受入
87-4-209
高工研図書室

EUROPEAN ORGANIZATION FOR NUCLEAR RESEARCH

CERN-EP/87-51
10.3.1987

NUCLEAR RADII AND MOMENTS OF UNSTABLE ISOTOPES

Erst W. Otten,

Institute of Physics, University Mainz, D-6500 Mainz

and

the ISOLDE Collaboration,

CERN, Geneva, Switzerland

January 1987

To be published in:
TREATISE ON HEAVY-ION PHYSICS
Edited by: D. Allan Bromley
Volume 8: Nuclei Far From Stability
Plenum Press, New York

TABLE OF CONTENTS

page:

ABSTRACT

The article deals with the isotopic change of mean-squared charge radii and with spins and moments of unstable nuclei, measured in extended chains of isotopes by off-line and on-line optical methods. The methodological development from traditional optical spectroscopy to the various techniques of laser spectroscopy is followed up. The state of the art of evaluating the isotope shift and the hyperfine structure with respect to ms charge radii and moments is outlined. The data cover about 400 nuclides of 20 elements. They are discussed in the frame of current nuclear models.

1. INTRODUCTION

The development of on-line mass-separators which provide long chains of isotopes extending far off stability immediately started the question, how to get access to the basic nuclear ground-state properties of these exotic nuclei, their spins, moments, radii and masses. In general the amount of radioactive material produced at these facilities is too low to form beams or targets for any kind of scattering or nuclear reaction experiment. The traditional spectroscopic methods, on the other hand, namely atomic, nuclear and mass spectroscopy turned out to be very efficient in this field since they could be well adapted to the special on line conditions met.

This article is dealing with radii, spins and moments which are the domain of atomic spectroscopy, as far at least, as nuclear ground states and long-lived isomers are concerned. The sources of information are the isotope shift (IS) and the hyperfine structure (hfs) of spectral lines. Whereas the evaluation of spins and magnetic moments from hfs poses no problem, the precision in evaluating spectroscopic quadrupole moments (Q_s) and isotopic variations of mean-squared (ms) charge radii from hfs and IS, respectively, is a matter of concern. It is adequate, therefore, to sum up briefly the basic concepts of analyzing IS and hfs in the following section 2. A central part of this review will be devoted to the description of the various spectroscopic methods which have been developed in this field (section 3). Most of them are still competitive,

and only few have exhausted their potential already. In the past decade, the development has focussed on laser spectroscopic methods. They can achieve optimum spectral resolution, i.e. free of Doppler-broadening, together with very high sensitivity. The principal goal of present methodological developments is the further increase in sensitivity. For that purpose the basic laser spectroscopic devices are embedded in complex, hybrid systems.

The discussion and interpretation of the results form another main topic of this review (section 4). For quite a number of elements typically 20 isotopes and more have been investigated by means of atomic spectroscopy. In some regions of the nuclear chart the results already cover a dense network, for instance from Cd to Sn, in the rare earth region, from Au to Pb and for the Rn-Fr-Ra sequence. Fig. 1.1 gives an overview on the systematic work on long chains of isotopes performed so far. In this plot is also included some off-line work on longer chains of stable or long-lived isotopes like, for instance, the important series of Ca isotopes. These complete sets of nuclear ground state data form a unique basis for a systematic overview and interpretation of the development of nuclear structure throughout the nuclear chart, linking far apart regions of very different structure, like spherical and deformed ones.

In this context the change of ms nuclear charge radii plays a guiding role, very similar to the one of the mass. Both quantities are governed globally by the liquid drop properties of the nucleus, which lead to the expansion

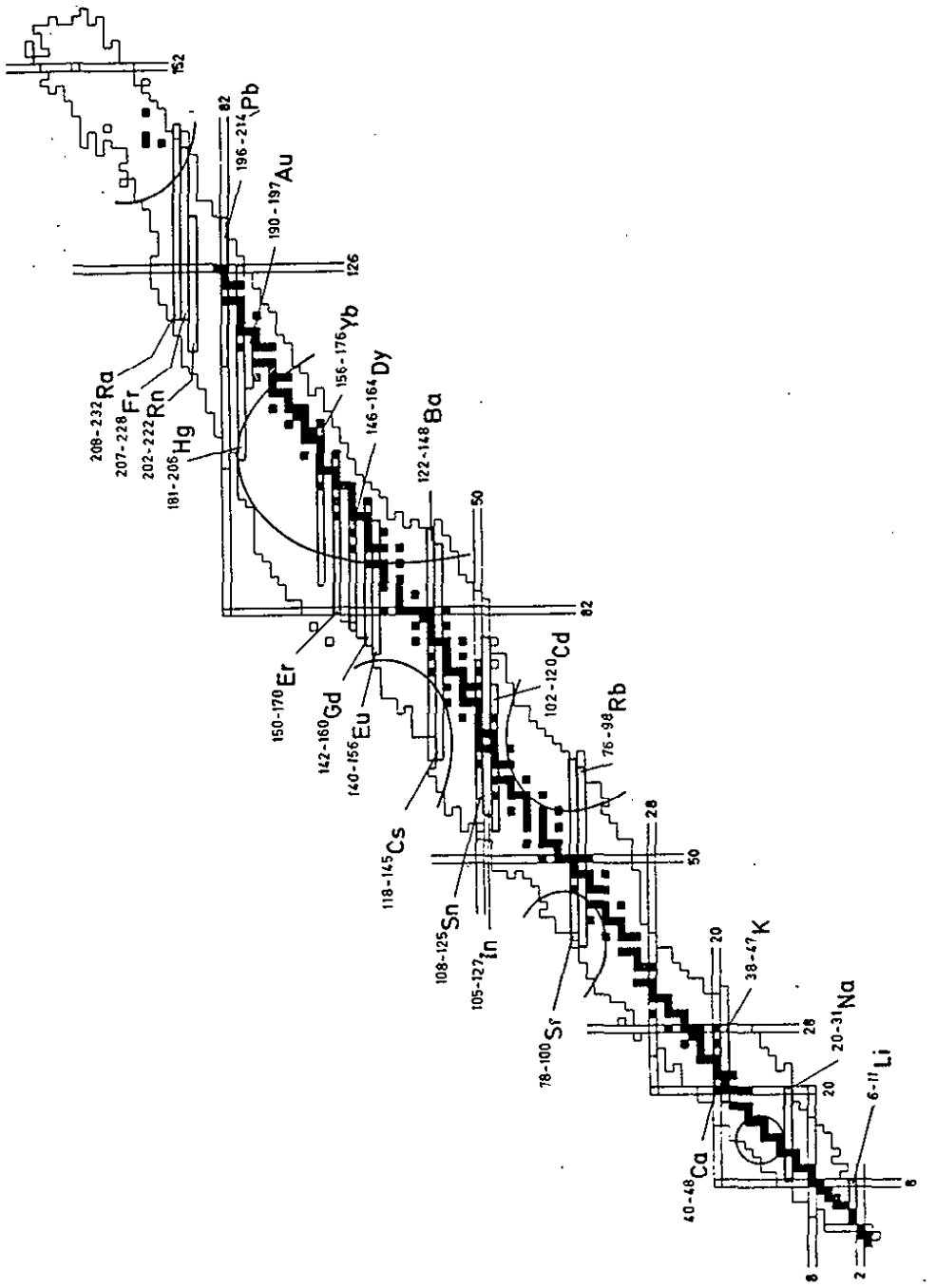

Fig. 1.1: Chart of nuclides showing extended chains of isotopes which have been investigated by optical spectroscopy off stability.

of the nuclear radius like $A^{1/3}$ and to the Bethe-Weizsäcker formula. If we define the deviations from the liquid drop model as the more interesting features of nuclear structure searched for, then we will find them in the deviations of the measured radii and masses from these two global laws. In isotope shift such deviations are caused predominantly by nuclear deformation which obviously increases the observable $\langle r^2 \rangle$. At shell closures we find characteristic changes in the average slope of the expansion of $\langle r^2 \rangle$, and at shape transitions we meet abrupt discontinuities.

Since isotope shift data are beginning to fill complete blocks in the N-Z plane, one can combine results from different elements in order to extract isotonic and isobaric shifts of the ms charge radius.

Whereas isotope shifts are sensitive to the mean-squared deformation $\langle \beta_2^2 \rangle$ of a nucleus, spectroscopic quadrupole moments are proportional to the first order term $\langle \beta_2 \rangle$ itself. Hence they show not only the size but also the sign of the deformation, provided that the coupling of the spin of the unpaired nucleons to the core is known. This interplay between collective and single particle structure is another interesting and valuable aspect in these systematic investigations. In regions of transitional nuclei we will also experience strong differences between the two observables $\langle \beta_2^2 \rangle_{IS}$ (from $\delta\langle r^2 \rangle$) and $\langle \beta_2 \rangle^2_{Q_s}$ (from Q_s), since the former includes zero point vibrations, the latter not. In the same sense spins and magnetic moments

may be used as fingerprints of collective nuclear structure by characterizing a particular Nilsson state, for instance.

The relations of spins, moments and ms radii to collective properties of nuclei may justify their joint discussion in this article. Still we do not aim at a complete discussion of all the spins and moments being measured off stability in recent years, but focus the interest on the systematics of ms radii. Their interpretation will mostly be structured according to different regions of nuclei accompanied by introductions into the different phenomena observed, like dynamic deformation near shell closures, shape transitions to static deformation, shape coexistence, isotone and isobar shift, odd-even staggering and octupole effects.

The different sections may be read rather independent from each other. The appendix contains a table with spins, moments and $\delta\langle r^2\rangle$ values measured in extended chains of isotopes by the techniques described in this article.

The field treated here has already been reviewed at an early stage by Jaquinot and Klapisch (Ja 79). Part of the techniques and results have also been summarized by Kluge (Kl 79, Kl 85), Neugart (Ne 85) and in ref. (Ot 81). A collection of papers in the field of laser spectroscopy of unstable isotopes is found in ref. (Be 82). Nuclear moments have been analyzed systematically by Ekström in the frame of the particle plus rotor model (Ek 81).

2. INTRODUCTION TO ISOTOPE SHIFT AND HYPERFINE STRUCTURE IN ATOMIC SPECTRA

2.1. The Isotope Shift

The IS of a spectral line between two isotopes with mass number A and A' is defined as

$$IS^{AA'} = \nu^{A} - \nu^{A'}. \qquad (2.1)$$

In case of hfs splitting the transition frequency ν is taken as the centre of gravity (c.g.) over all hfs components of the line. Note that the hfs interaction does not shift the c.g. in first-order perturbation theory which is usually an excellent approximation. The origin of the IS is twofold, namely the change of the nuclear mass M^{A} and of the nuclear charge distribution.

2.1.1. The Mass Shift

In hydrogen-like spectra the mass effect $\delta\nu_{M}$ is trivially accounted for by introducing the reduced electron mass. To good approximation it is given by

$$\delta\nu_{MN}^{AA'} = \frac{(M^{A}-M^{A'})m_e}{M^{A}\,M^{A'}}\,\nu^{A} \approx \frac{A-A'}{A\,A'}\,\frac{m_e}{amu}\,\nu^{A} = N\,\frac{A-A'}{A\,A'} \qquad (2.2)$$

(m_e = electron mass, amu = atomic mass unit). N indicates the so-called normal mass effect. In many electron spectra different

electron momenta may be correlated, leading to a collective retroaction onto the nuclear motion. It causes the so-called specific mass effect

$$\delta\nu_{MS}^{AA'} \approx S \frac{A-A'}{A\,A'} \qquad (2.3)$$

which still has the same A-dependence as the normal one. When shielded d- and f-electrons are involved in the transition, like in transition elements and rare earths, S can be of order of 10 N and more. But for simple s-p transitions, which are the most important ones in view of probing the nuclear charge distribution, experimental evidence has proved $|S| \lesssim N$ (He 74). Hartree-Fock calculations of S are very difficult; for some cases they are available and partially meet the experimental values. Since the mass shift is entirely a problem of atomic and not of nuclear structure, we will not persue it further and refer to the books of Kopfermann (Ko 58), Kuhn (Ku 69) and King (Ki 84) for more details. Methods to separate the mass effect from the field effect will be discussed below.

2.1.2. The Field Shift

The influence of the finite extension of the nuclear charge distribution on the electronic binding energy, usually called field shift $\delta\nu_F$, is easily derived in non-relativistic, first-order perturbation theory. For this purpose we write the electrostatic energy as an integral over the nuclear charge distribution $\rho(\vec{r})$ times the potential of the electron $V(\vec{r})$:

$$E_c = \int_0^{R_1} \rho(\vec{r})\, V(\vec{r})\, d\tau \qquad (2.4)$$

where R_1 is the radius at which $\rho(\vec{r})$ drops to zero (see Fig. 2.1). We restrict ourselves to s-electrons which produce a spherically symmetric V(r). We can separate V(r) inside $r \leq R_1$ into a constant part $V(R_1)$ which stems from the electronic charge outside R_1 and a variable one v(r) due to the inner charge. To good approximation we may take the non-relativistic s wave function $\Psi_s(r)$ of an electron as being constant over the nuclear volume and hence get for v(r) the parabola

$$v(r) = -2\pi e\, |\Psi_s(0)|^2\, (R_1^2 - r^2/3). \qquad (2.5)$$

Remembering further the relation

$$V(R_1) + v(0) = V(0) = -e \left\langle \frac{1}{r} \right\rangle_{\text{electron}} \qquad (2.6)$$

we get the total potential inside R_1

$$V(r) = -e \left\langle \frac{1}{r} \right\rangle_{\text{electron}} + \frac{2\pi}{3} e\, |\Psi_s(0)|^2\, r^2. \qquad (2.7)$$

After inserting eq. (2.7) into eq. (2.4) it follows:

$$E_c = -Z e^2 \left\langle \frac{1}{r} \right\rangle_{\text{electron}} + \frac{2\pi}{3} Z e^2\, |\Psi_s(0)|^2 \langle r^2 \rangle_{\text{nucleus}}. \qquad (2.8)$$

The first term in eq. (2.8) represents the monopole interaction with a point-like nucleus, the second one the finite size correction. The latter is the product of the electronic

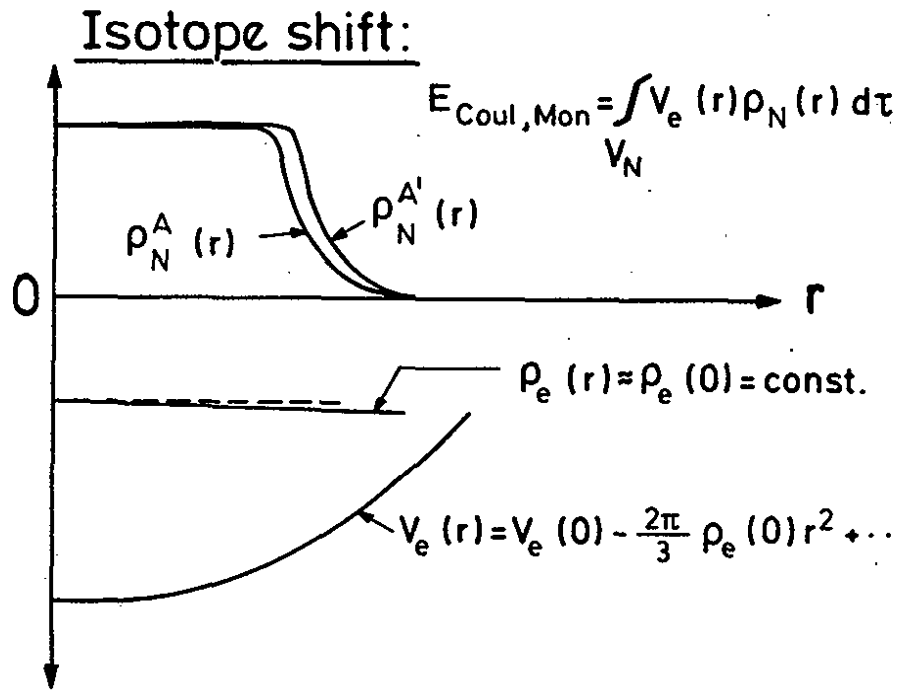

Fig. 2.1: Schematic drawing of a nuclear (ρ_n) and an electronic (ρ_e) charge distribution, the latter one for a s-wave function. In addition the potential (V_e) made up by the electron is shown.

charge density at the origin times the second radial moment of the nuclear charge distribution.

Let us note: (i) Eq. (2.8) was derived model-independently with respect to $\rho(\vec{r})$ thus holding for any nuclear shape, therefore. (ii) The restriction to s-electrons is justified, since others do not overlap considerably with the nucleus. (iii) The theory also holds for the lightest muonic atoms; for heavier ones the muon wave function varies strongly over the range of $\rho(\vec{r})$. Therefore, the finite size correction is characterized by more complicated radial moments in case of muons. These are the so-called Barett moments, which depend on the particular muonic transition in question. Muonic results have been tabulated by Engfer et al. (En 74).

The finite size effect in electronic spectra is too small in order to allow a direct determination of the total $\langle r^2 \rangle$ of a nucleus from a given electronic term value, even, if this has been measured to highest accuracy. This is due to the fact that the leading terms in the binding of many electron atoms cannot be calculated to the necessary precision of order 10^{-6}, the level at which the finite size effect appears. Thus, only a change of $\langle r^2 \rangle$ within an isotopic series or between isomers can be measured, since the first term in eq. (2.8) as well as other contributions to the binding cancel by taking the isotopic difference (except for the mass shift). The non-relativistic field shift between isotopes or isomers in an optical transition is thus given by

$$\delta\nu_{Fn.r.}^{AA'} = -\frac{2\pi}{3} Z e^2 \Delta|\Psi(0)|^2 \delta\langle r^2\rangle^{AA'} \qquad (2.9)$$

where $\Delta|\Psi(0)|^2$ is the change of electron charge density at the nucleus between lower and upper state of the optical transition.

In the case of heavier elements it is necessary to proceed to a relativistic level of the theory. In this case it is no more adequate to use the Dirac s wave functions for a point-like nucleus as starting point of a perturbation theory like in eq. (2.4); because they show a logarithmic divergence at the origin which leads to an unrealistic exponent of the radial moment of the charge distribution measured by the field shift. Instead, the Dirac equation is solved first near the origin in an extended, approximate nuclear charge distribution of liquid drop dimension

$$R_o = r_o A^{1/3}. \qquad (2.10)$$

Fig. 2.2, taken from Kopfermann's book (Ko 58), shows the difference between both solutions for Z = 90. The solution for an extended charge is still rather constant within the nuclear radius R_o. If we calculate the field shift with this wave function in perturbation theory we can expect, therefore, that $\delta\nu_F$ will still be proportional to the isotopic change of the second radial moment with reasonable accuracy. Bodmer (Bo 59) has shown that the Dirac solution in an extended nuclear charge and hence the field shift are quite insensitive to details of the charge distribution, in fact. He has derived the relativistic formula

$$\delta\nu_F = -\frac{\pi a_o^3}{Z}\,\Delta|\psi(0)|^2\,\mathcal{F}(Z)\,N(Z)\,\langle r^2\rangle^{\sigma-1}\,\delta\langle r^2\rangle. \qquad (2.11)$$

$\mathcal{F}$ and N are known functions of Z (see (Ki 84)), $\sigma = \sqrt{1-\alpha^2Z^2}$, α is the fine structure constant, a_o is the Bohr radius. Since σ is close to 1, $\delta\nu_F$ is still dominated by $\delta\langle r^2\rangle$ and depends in addition weakly on the total $\langle r^2\rangle$ of the nucleus. One can account for the latter effect with sufficient accuracy by inserting into eq. (2.11) the liquid drop estimate

$$\langle r^2\rangle = 3/5\; r_o^2\; A^{2/3}. \qquad (2.12)$$

This allows to contract eq. (2.11) further to

$$\delta\nu_F^{AA'} = -\frac{\pi a_o^3}{Z}\,\Delta|\psi(0)|^2\,f(Z)\,\delta\langle r^2\rangle^{AA'} = F(Z)\,\delta\langle r^2\rangle^{AA'} \qquad (2.13)$$

where the field shift is now factorized into an electronic factor F(Z) and a nuclear one $\delta\langle r^2\rangle$. A revised table of f(Z) has recently been published by Blundell et al. (Bl 85).

In eq. (2.13) $\Delta|\psi(0)|^2$ still describes the non-relativistic change of the electronic charge density which may be calculated from non-relativistic, semi-empirical formulae (see below). It serves to calibrate the amplitude of the Dirac solution of the electronic states in question by fitting the relativistic to the non-relativistic wave functions at $r > R_1$ outside the nucleus.

For the very heaviest elements the constancy of the electronic wave function over the nuclear volume cannot be claimed anymore, requiring an expansion of the nuclear factor into a power series of radial moments (Se 69) which replaces $\delta\langle r^2\rangle$ by

$$\lambda^{AA'} = \delta\langle r^2\rangle^{AA'} + \frac{G(Z)}{F(Z)}\,\delta\langle r^4\rangle^{AA'} + \frac{H(Z)}{F(Z)}\,\delta\langle r^6\rangle^{AA'} + \ldots \qquad (2.14)$$

For a spherical nucleus λ is about 6 % smaller than $\delta\langle r^2\rangle$ at $Z = 80$. The shape dependence of the Seltzer correction (2.14) has been discussed e.g. by Ahmad et al. (Ah 85,87).

According to equations (2.9), (2.12) and (2.16) (see below) the field effect varies approximately like $Z^2A^{-1/3}$. For $\delta A = 2$ it is of order 10 MHz in Li and 10 GHz in Fr.

2.1.3. Separation of Mass and Field Shift

The IS has usually been measured in several electronic transitions; but data for the full isotopic series have rarely been taken in that particular transition for which the electronic mass and field shift factors can be calculated most reliably. However, different data sets can be related to each other by the so-called King plot (see ref. (Ki 84)) which, fortunately, separates field and mass shift and also controls the consistency of the data sets. For this purpose the measured IS in two different transitions 1(2) given as

$$IS^{AA'}_{1(2)} = \frac{A-A'}{A\,A'}\,(N_{1(2)} + S_{1(2)}) + F_{1(2)}\,\lambda^{AA'} \qquad (2.15)$$

are multiplied by AA'/(A-A') thereby transforming them into linear equations of the same argument $\lambda^{AA'}$ (A-A')/AA'. These renormalized isotope shifts are plotted for all pairs AA' in a (x_1,x_2)-plane, where the data points form a straight line with slope F_2/F_1 and intersection $(N_2+S_2) - (N_1+S_1)\ F_2/F_1$ on the x_2 axis. Thus the ratio of field shifts and the difference of mass shift factors (modified by F_2/F_1 in one term) can be extracted separately from the King plot. Fig. 2.3 shows some King lines for the example of Ba. The alkali-like, ionic resonance transition ($6s\ ^2S_{1/2}$ - $6p\ ^2P_{3/2}$, λ = 455 nm) in Ba II (We 84) whose F-factor is favourably calculated serves as reference on the horizontal axis. Within the limits of error the data points fall on straight lines as they should. The King line versus the atomic resonance transition ($6s^2\ ^1S_0$ - $6s6p\ ^1P_1$, λ = 554 nm) (Be 79, Mu 83) almost crosses the origin and hence shows no evidence for any specific mass shift in either of the two transitions. The transition $5d\ ^2D_{3/2}$ - $6p\ ^2P_{3/2}$, λ = 585 nm (Si 80), on the other hand, has a pronounced specific mass shift $S \approx 4\ N$ and a negative F-factor with respect to the reference transition. Both effects are due to the inner 5d electron which orbits inside the core and thus gives rise to correlations with and screening of core electrons.

For preparing a King plot one needs at least three isotopes measured. But if the field shift in an isotopic series happens to be as regular as the mass shift, i.e. proportional to A-A' almost, then the data points converge towards a single

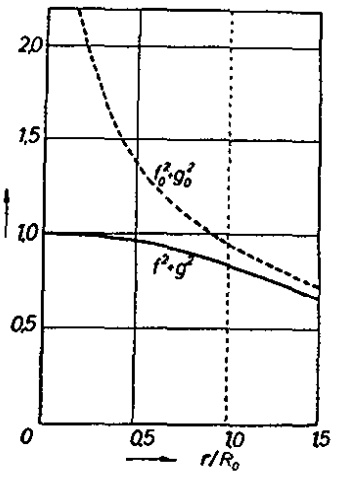

Fig. 2.2: Density of an electronic Dirac-s-wave function in the potential of a point-like (broken line) and of an extended nucleus of radius R_o (full line) for Z = 90 (Ko 58).

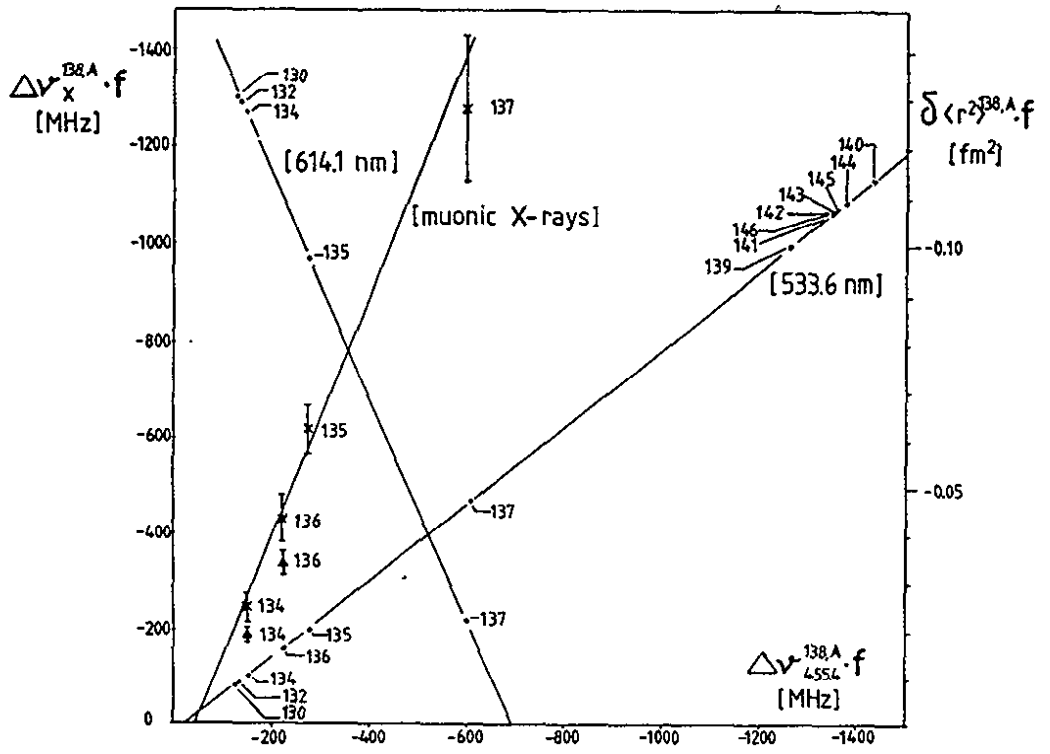

Fig. 2.3: King plots $IS^{A,138}$ of transitions in Ba I and Ba II with respect to the reference transition λ = 455 nm. The IS is renormalized by the factor f = 2A/136(A-138). Also shown is the King line versus the muonic isotope shift fitted to the results of ref. (Sh 82) (crosses). Muonic results from ref. (Ku 83) are given for comparison (triangles). The vertical scale on the right applies to the muonic IS. For all transitions the normal mass shift has been substracted already from the IS.

point on the King line and the fit of its two parameters, slope and intersection, becomes rather poor. Unfortunately, a regular expansion of $\langle r^2 \rangle$ is the rule for sequences of stable, even isotopes; and these are, more or less, the only ones for which precise absolute $\delta\langle r^2 \rangle$ determinations are available from either X-ray or muonic IS or from electron scattering experiments. Therefore, these non-optical measurements served so far only in a few cases to calibrate the optical field and mass shift on an absolute scale via King plots (compare Fig. 2.3 and the following section). The situation is rescued to some extent by the fact that poorly fitted King parameters are still well correlated, and this correlation partly compensates their individual errors in the final evaluation of $\delta\langle r^2 \rangle$.

2.1.4. Evaluation and Calibration of Field Shift Constants

An important problem in the evaluation of $\delta\langle r^2 \rangle$ via eq. (2.13) is the determination of $\Delta|\Psi(0)|^2$. Traditionally it is calculated by the semi-empirical Goudsmit-Fermi-Segrè (GFS) formula (Ko 58, Ar 71) which relates $|\Psi(0)|^2$ of s-electrons to the effective quantum number $n^* = n-\sigma = (Z_a^2\ \mathrm{Ry}/T_n)^{1/2}$ and its derivative $dn^*/dn = 1-d\sigma/dn$, σ = quantum defect, Z_a = outer charge (being 1 for neutral atoms), Ry = Rydberg constant, T_n = term value. The GFS formula reads:

$$|\Psi(0)|^2 = \pi a_o^{-3}\ Z\ Z_a^2\ (1-d\sigma/dn)/n^{*3} \qquad (2.16)$$

In alkali-like spectra e.g., the favourable transitions being

sensitive to $\delta\langle r^2\rangle$ are those of the principal series ns to n'p. The p doublet has no density at the nucleus in the non-relativistic limit; but the $p_{1/2}$ state gains some density by relativity (see ref. (Ko 58)). A semi-empirical formula for the latter one has recently been given and proved experimentally by Wendt et al. (We 84). Besides its direct contribution to $|\Psi(0)|^2$ any valence electron may also cause an indirect one by screening inner s-shells. Both effects are taken into account by a correction ß in the form

$$\Delta|\Psi(0)|^2_{ns\to n'p} = ß\,|\Psi(0)|^2_{ns}. \qquad (2.17)$$

ß is of order 1.1 for an alkali-like ns→np transition (He 74).

The quantity $|\Psi(0)|^2$ also determines the magnetic hfs splitting corstant a_s (compare below) of an s-electron through the so-called Fermi contact interaction:

$$a_s = (8\pi/3)(\mu_o/4\pi)(2\mu_B)(\mu_I/I)|\Psi(0)|^2_{ns}\,F_{1/2}(Z)(1-\delta)(1-\varepsilon) \qquad (2.18)$$

μ_o = permeability of vacuum; μ_B = Bohr's magneton; F_r = relativistic correction; $(1-\delta)$ = Breit-Crawford-Schawlow correction, taking into account the influence of the extended nuclear charge on the Dirac wave function already discussed above; $(1-\varepsilon)$ = Bohr-Weisskopf effect, stemming from the finite extension of nuclear magnetization. The corrections are discussed and tabulated in (Ko 58, Sc 55, Sc 57, Ar 71, Li 74).

Since the nuclear g_I-factor is usually known from an independent source (e.g. NMR) for at least one isotope of a given element, $|\Psi(0)|^2$ may also be determined from a_s and g_I through (2.18), therefore. This procedure is certainly correct for the direct contribution of the valence s-electron to the IS and hfs. But for the indirect contributions, induced by screening, core polarization etc., this is not necessarily true, since the IS is sensitive to the charge density but a_s to the spin density. With respect to many body effects these two may differ from each other because of exchange interaction. It is astonishing that in spite of these complications by many body effects eq. (2.18) correctly reproduces a_s to about 5 % in almost any known case (Ko 58). This success of the GFS formula is the main reason for its continued application in hfs as well as IS analysis. Its extension to configurations with more than one valence electron is possible and successful in many cases (Ko 58). Even in complex spectra like those of rare earths and transition elements the IS could be analyzed systematically this way (see e.g. references (He 74, Ki 84)). These analyses are subtle, cover many different lines in each spectrum and make in addition use of Hartree-Fock calculations (see below) in order to fix screening corrections etc.

An alternative way to analyze field shifts is offered by straight, relativistic Hartree-Fock calculations of F(Z) which include also most of the many body effects like screening etc. It has been chequed by many examples that they reproduce ratios of F-factors quite well even in rather complex spectra (Au 85,

Au 86, He 74, Ki 84). For instance the ratio F_{554}/F_{455} for Ba is determined from the King plot in Fig. 2.3 to be 0.808(2) whereas Torbohm et al. (To 85) have calculated 0.783. However, the absolute precision of F(Z) values from Hartree-Fock calculations is still a matter of discussion. They are lying systematically 15 - 25 % below those, calculated semi-empirically. King and Palmer have recently discussed the situation again and conjecture that the truth may lie somewhere in the middle between both procedures (Ki 86). On the other hand, the systematic character of the discrepancy makes clear that it is not due to deficiencies in the calculation of individual valence states. It might be caused rather by perturbations located deeply inside the core thus connecting to states of high momenta far out in the continuum which would lead to a kind of renormalization of the field shift. The dilemma is that the experimental calibration of F(Z) discussed in the following is difficult and cumbersome and only few useful data have been published.

For calibrating F(Z) one needs independent information on $\delta\langle r^2\rangle$ or more correctly on λ. From a pure physics standpoint of view, K - X-ray isotope shifts are most suited, since they also measure λ directly. Moreover, the calculation of mass and field shift factors poses no serious problem there, because the inner shell electrons are essentially unscreened. However, the experimental precision is marginal since $\delta\nu_F$ is about a hundred times smaller than the linewidth. Only for the heaviest elements satisfactory accuracy is achieved. For the case of lead e.g. an accuracy of 5 % was obtained in very careful mea-

surements by Borchert et al. (Bo 83) who also compared their results systematically to those from optical and muonic IS and from electron scattering. X-ray IS's have been compiled by Boehm and Lee (Bo 74).

Electron scattering experiments offer another access to nuclear charge radii through the formfactor F(q). For small momentum transfer q, it may be expanded as

$$F(q) = 1 - q^2 \langle r^2 \rangle / 6 + O(q^4) \langle r^4 \rangle). \qquad (2.19)$$

This method provides an excellent model-independent determination of the total $\langle r^2 \rangle$ by taking the slope $dF/d(q^2)$ at $q^2 = 0$. However, the precise measurement of the small $\delta\langle r^2 \rangle$ effect in an isotopic series is difficult and therefore, has been only performed for a limited number of cases (compare the compilation of de Jager and de Vries (Ja 74). The more recent experiments are aiming not just for the $\langle r^2 \rangle$ term in eq. (2.19), but for a complete measurement of F(q) over a q-range as wide as possible. A Fourier-Bessel transformation of F(q) leads to a determination of the *monopole charge distribution* $\rho(r)$. By extending these measurements over series of isotopes and isctones one obtains a complete information about the local change $\delta\rho(r)$ at any r and not just $\delta\langle r^2 \rangle$. Needless to say that *such measurements* provide much more detailed information on nuclear structure than the optical IS. Fig. 2.4 gives an example for the isotope pair ^{48,40}Ca (Em 83) which is discussed in section 4.8. in more detail. Obviously $\delta\langle r^2 \rangle$ can be determined straight away from this

measurement by taking the integral

$$\delta\langle r^2\rangle = (1/Z) \int_0^\infty r^2 \delta\rho(r)\, d\tau. \qquad (2.20)$$

Again such examples are rare since it would require extraordinary efforts to perform them systematically throughout the nuclear chart.

An easier access to nuclear charge distribution and its isotopic dependence is provided by muonic spectra. As already mentioned they measure a radial moment which explicitly depends on the particular muonic transition measured and which differs strongly from $\langle r^2\rangle$ except for the lightest elements. In order to convert both observables into each other one needs knowledge on $\delta\rho(r)$ again. Fricke et al. concluded, therefore, that a combined analysis of electron scattering and muonic data probably offers the most effective method of calibrating the $\delta\langle r^2\rangle$ scale (Fr 81, Fr 83, Bo 83). However, this statement presupposes not only precise measurements but also sufficiently correct calculations of nuclear core polarization by the muon which constitutes a large fraction of the muonic IS (reviewed, e.g. in ref. (Sc 78)). At present it seems as if this latter problem is not jet fully under control. For instance the calculation of $\delta\langle r^2\rangle$ from muonic Ba spectra by Kunold et al. (Ku 83) differs from that by Shera et al. (Sh 82) by more than 20 % (compare Fig. 2.3, see also ref. (Bo 83) for the lead case).

Let us summarize the situation, as it appears at present:

As to the mass shift: since it decreases about as fast with mass number as the field shift increases, it can cause serious difficulties in the analysis of lighter isotopes up to $A \lesssim 150$ and it is of little importance for $A \gtrsim 150$.

The calculations of absolute field shift factors by Hartree-Fock methods or semi-empirical formulae differ from each other and may be in error by 10 % to 30 %, depending on the complexity of the spectrum. Similar accuracy has been reached by the various calibration methods. The error in F is a pure scaling error and does not affect ratios of $\delta\langle r^2\rangle$ in an isotopic series. If there is left a systematic error in F, it seems not to scatter very much, but has to be about the same for all the elements measured. Otherwise the slope $(\delta\langle r^2\rangle^{NN'}/N-N')$ would scatter substantially for different isotones. That would necessarily lead to a crossing of their ms charge radii somewhere off stability, such that $\langle r^2\rangle$ of a nucleus (Z,N) becomes smaller (at constant shape!) than that of a lighter isotone (Z-x,N). Such an unphysical behaviour has never been observed.

2.2. Atomic Hyperfine Structure

2.2.1. Introduction to hfs

The hfs in atomic spectra is the classical example of static multipole interaction. Due to the small ratio of nuclear to atomic radius it converges very rapidly with powers of this ratio. Besides the leading electric monopole, only the magnetic dipole and electric quadrupole interaction are of practical

importance, therefore. For the same reason the hfs interaction is separable into a product of a nuclear matrix element, the moment, and an electronic one, the hfs field. Note further that the nuclear matrix element is always a diagonal one for a state of definite spin parity assignment I^p. Therefore, only moments of even parity contribute to hfs. The odd ones vanish identically. This fact answers the question, for instance, why octupole deformation of nuclear charge distribution cannot be observed through hfs, although it may be different from zero if measured in the intrinsic frame of the nucleus. The latter statement is not in contradiction to the first one since a measurement in the intrinsic frame never corresponds to a pure quantum state I^p.

The hfs coupling of nuclear and electronic angular momenta I, J to the total one of the atom F is given by the well-known formula (Ko 58)

$$W(F) = A\ K/2 + B\ \frac{3}{4}\ \frac{K(K+1) - I(I+1)J(J+1)}{2(2I-1)(2J-1)\ I\cdot J} \qquad (2.21)$$

with $K = F(F+1) - I(I+1) - J(J+1)$. $A = \mu_I\ H_e(0)/I\cdot J$ is the magnetic dipole and $B = e\ Q_s\ \varphi_{jj}(0)$ is the electric quadrupole coupling constant. $H_e(0)$ is the magnetic field, $\varphi_{jj}(0)$ the electric field gradient produced by the electrons at the site of the nucleus. In the traditional notation of eq. (2.21) the moments and fields are defined as the expectation values of the respective operators in the states of maximum projection $m_I = I$, $m_J = J$.

Fig. 2.5 shows a schematic plot of a hfs multiplet. The magnetic hfs follows Lande's interval rule stating that two neighbouring levels are split by $F_> \cdot A$, where $F_>$ is the larger of the two F-values. For $Q_s > 0$ the quadrupole interaction lifts levels with I and J parallel or antiparallel, and it loweres those with perpendicular spins.

For unpaired s-electrons the magnetic hfs usually exceeds the Doppler width of a spectral line of roughly 1 GHz; for p-electrons it is at least larger than the natural line width which is typically 1 to 20 MHz. For a deformed nucleus of medium mass ($A \approx 100$) a p-electron produces an electric quadrupole splitting of about equal size as the magnetic dipole splitting.

2.2.2. On the Evaluation and Calibration of hfs Fields

For a single valence electron in a state $|n\ell j\rangle$ the hfs coupling constants, denoted now by small letters $a_{n\ell j}$, $b_{n\ell j}$ are given for $\ell > 0$ in first approximation by (Ko 58, Ar 71)

$$a_{n\ell j} = \frac{\mu_o}{4\pi} \frac{2\mu_B \mu_I}{I} \frac{\ell(\ell+1)}{j(j+1)} \langle r^{-3} \rangle_{n\ell} \, F_j(Z_i) \, (1-\delta) \, (1-\varepsilon) \qquad (2.22)$$

$$b_{n\ell j} = \frac{e^2}{4\pi\varepsilon_o} Q_s \frac{2j-1}{2j+2} \langle r^{-3} \rangle_{n\ell} \, R_{\ell j}(Z_i) \qquad (2.23)$$

$F_j(Z_i)$ and $R_j(Z_i)$ are relativistic corrections factors (Ko 58, Sc 55,57, Li 75). Z_i is the nuclear charge, seen by the inner part of the electronic wave function close to Z; e.g. $Z_i = Z-4$ for p-electrons. The a-factor for an s-electron was already

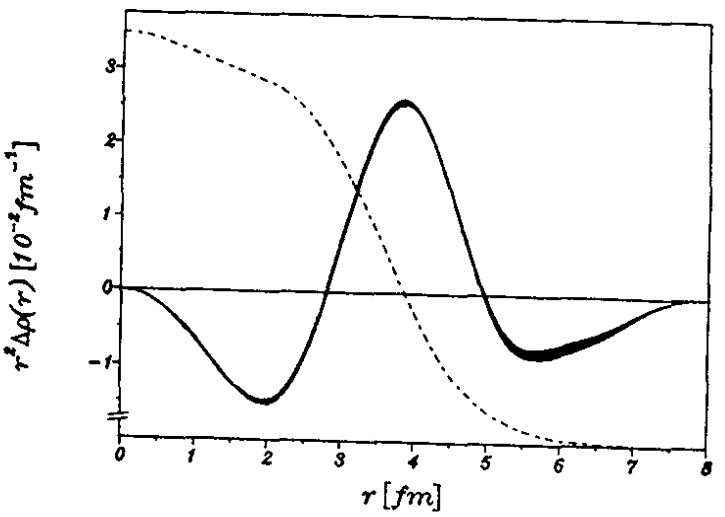

Fig. 2.4: Plot of the quantity $r^2\,\delta\rho(r)$ for the isotope pair $^{48,40}Ca$. Charge is shifted from the centre and the outer skin towards the surface region around the half density radius c. The width of the band corresponds to the error. For comparison also $\rho(r)^{40}$ is shown on an arbitrary scale (Em 83).

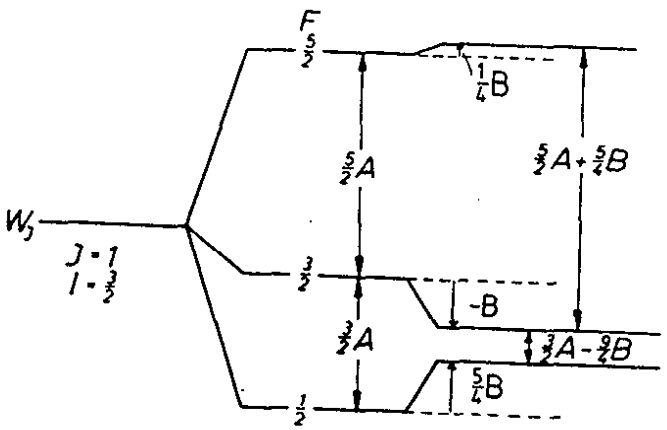

Fig. 2.5: Hyperfine multiplet for J = 1, I = 3/2 with magnetic dipole (A) and electric quadrupole (B) splitting.

given in section 2.1.4. by eq. (2.18).

The main problem is the evaluation of the radial matrix element $\langle r^{-3} \rangle$. Semi-empirically it can be determined either from the effective quantum nuclear n* through Lande's formula

$$\langle r^{-3} \rangle = \frac{Z_i \, Z_a^2}{(n^*)^3} \qquad (2.24)$$

or from the fine structure splitting ΔW_{FS} which is also proportional to $\langle r^{-3} \rangle$

$$\Delta W_{FS} = \frac{\mu_o}{4\pi} \; 2\mu_B^2 (\ell + \tfrac{1}{2}) \langle r^{-3} \rangle H(Z_i) \qquad (2.25)$$

where $H(Z_i)$ is another relativistic correction. In the p-series of alkalis, e.g., both methods agree extremely well. Also ab-initio calculations reproduce these particular $\langle r^{-3} \rangle$ values quite well. However, this success does not solve the whole problem, since core polarization effects are not jet included in eq. (2.22) and eq. (2.23). In the magnetic case they can exceed even the direct contribution, in the electric case they are of the order of 20 % and known as Sternheimer correction (St 50). In case of simple spectra these two corrections are also under reasonable control.

The analysis of the hfs of complex spectra is usually performed by the help of the relativistically correct parametrization of the hfs interaction given by Sandars and Beck (Sa 65). A certain number of radial matrix elements attached to angular momentum

operators are treated as free parameters and fitted to experimental results. They can also be computed ab-initio with limited success (Li 74, Bü 82).

Since n* is roughly constant ($\approx$ 1.5) for atomic ground states throughout the periodic system the hyperfine fields increase approximately with Z according eq. (2.24). The experimental calibration of magnetic hfs fields is no problem, since for virtually any element μ_I of at least one isotope has directly been measured in an external field by NMR or an equivalent method. The last major gap in this respect concerned the radioactive elements Rn, Fr, Ra; it could be recently filled by experiments at ISOLDE (Ca 85, Ro 84, Ar 87). Electric hfs fields have only been calibrated for a limited number of elements through a measurement of the muonic quadrupole splitting. For higher excited states $n \gtrsim 3$ it can be safely analyzed with respect to Q_s (Sc 78, St 85). These measurements have also shown that for well-deformed nuclei the projection formula of the intrinsic quadrupole moment Q_o on to the spectroscopic one Q_s holds with remarkable precision of a few percent in its strong coupling limit

$$Q_s = \frac{I(2I-1)}{(I+1)(2I+3)} Q_o . \qquad (2.26)$$

Hence this formula offers another possibility to calibrate the quadrupole splitting for spectra of elements with well-deformed isctopes and well-measured Q_o.

3. METHODS OF ATOMIC SPECTROSCOPY FAR OFF STABILITY

3.1. Early and Non-Optical Experiments off Stability

Optical spectroscopy of unstable isotopes faces two basic problems: i) How to gain sufficient sensitivity in tracing optical signals from the minute samples of material available? (ii) How to achieve, or at least preserve, under the constraint of highest sensitivity sufficiently high spectral resolution in order to resolve IS and hfs? In the course of this section we will learn how laser spectroscopic methods on-line with mass-separators for radioactive beams (ISOL-systems) solved these problems in several elegant and favourable ways. But on the way to these more recent developments we will touch upon a few early experiments in the field of unstable isotopes, including non-optical methods which provided knowledge on spins and moments but not on the isotope shift.

In traditional optical spectroscopy emission spectra from hollow cathodes or other kinds of spectral lamps are analyzed with high resolution gratings or Perot Fabry interferometers. This method is Doppler-limited, of course, but resolves hfs and IS of heavier nuclei ($A \gtrsim 100$), in particular, if cooled sources are used. Applications to unstable isotopes were limited to off-line experiments, managing half lives $T_{1/2} \gtrsim 1$ day. The classical example of this type of work is the measurement of a sericus of Hg isotopes $192 \leq A \leq 204$ by Tomlinson and Stroke (To 64). The lighter members of this chain were produced by

(p,x_n) reactions in a Au foil. Thereafter, Hg was heated out of the foil in vacuo and destilled into a small quartz bulb which was sealed off finally. The spectrum was excited by a rf-discharge and photographed with a diffraction grating spectrograph. Fig. 3.1 shows the IS in the Hg series together with results from neighbouring Tl.

Since Hg is a rather volatile and inert element this experiment worked down to quantities of the order of 10 ng. The demand for volatility and (or) chemical stability seriously restricted the application of the traditional optical methods to unstable isotopes and is still a crucial handicap in many of the more recent experimental methods applied off stability.

Among the non-optical methods we mention Rabi's famous atomic beam magnetic resonance method (ABMR). It could be adapted generally to the investigation of unstable isotopes by tracing the radioactivity of the collected beam, thereby taking advantage of the high sensitivity and selectivity of this detection technique. In this way a huge number of long-lived unstable nuclei have been investigated off line in the past (Ni 57). The method is also competitive far off stability when running at a powerful isotope separator on line (ISOL-system) such as the ISOLDE at CERN (Ra 79). The first systematic measurements of spins and magnetic moments of long series of alkalis Rb (Ek 78), Cs (Ek 77), Fr (Ro 84) were performed by ABMR at ISOLDE; measurements on Au (Ek 80), In and Tl (Ek 84) followed. Later laser spectroscopic experiments enabled in addition the determination of Q_s and $\delta\langle r^2\rangle$ values (see below). Under on-line conditions

ABMR reaches a sensitivity down to beam intensities of about 10^5 atoms/s.

Other rf methods such as NMR and optical pumping played a sophisticated trick to monitor the rf resonance by radioactivity: Since the nuclear rf resonance results basically in a destruction of nuclear polarization, it can be monitored by a change of the parity violating asymmetry of the angular distribution of ß-decay. If excited nuclear levels are concerned, the anisotropy of γ-radiation is used instead. These methods belong to the vast field of angular correlation techniques from which most of our knowledge on moments of excited states stems. The nuclear orientation technique at low temperature (NOR) enabled to extend such measurements also to ground states of nuclei far from stability. On-line applications of this method have been successful recently, for instance in neutron-deficient Au and In isotopes (Wa 85, Va 85) and are developing fast (reviewed e.g. in ref. (St 85)). Since these methods cannot be covered within the frame of this article we refer to the topical literature (Ka 81, Ni 83, Ra 85). However, there exists one optical method linked to this field which played an important role in the early years of research far off stability, it is the RADOP method which will be discussed in the following section.

3.2. Radioactive Detection of Optical Pumping (RADOP)

Optical Pumping (OP) is an efficient method to polarize an atomic vapor by absorption of polarized resonance light. The angular momentum of the photons is first transferred to the

valence electron and then by hfs coupling to the nuclear spin as well.

The detailed mechanism of OP is shown in Fig. 3.2, where a mercury isotope with I = 1/2 is taken as an example. The diamagnetic ground state $^1S_0$ has total angular momentum F = I = 1/2 because of J = 0. It splits into two nuclear Zeeman levels m_I = +1/2 and -1/2. The excited $^3P_1$ state has two hyperfine components with F = 1/2, 3/2 which split into two and four Zeeman levels, respectively as shown in Fig. 3.2. Let us assume that the optical excitation via the resonance line excites only one of the upper F levels, either the F = 1/2 or the F = 3/2 level. In Hg this is possible in general, since the hfs splitting is large as compared to the Doppler width of the spectral line. Right handed σ^+-light leads to Δm_F = + 1 absorption. The relative tranistion probabilities given in Fig. 3.2, the pumping rate and the relaxation rates in the excited and the ground state govern the nuclear polarization $P_I = \langle I_z \rangle / I$ finally achieved. Collisions with buffer gas atoms (usually a noble gas) depolarize the excited p state during its lifetime of ≈ 100 ns due to the atomic quadrupole moment of a state with $\ell > 0$. Thus reemission is isotropic. In the spherically symmetric atomic ground state, however, relaxation rates are negligible as compared to the pumping rate. Under these conditions the steady state is reached when the product of population numbers times absorption probability is the same for all of the ground state sublevels. This leads to P_I = + 100 % for pumping through the F = 1/2 channel and to - 50 % through the other one.

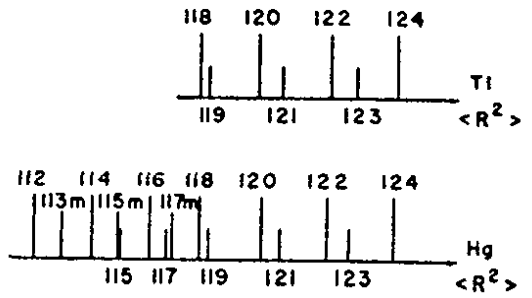

Fig. 3.1: ms charge radii of stable and long-lived Hg and Tl isotopes determined by classical spectroscopy off line. The scale is arbitrary (To 64 and references therein).

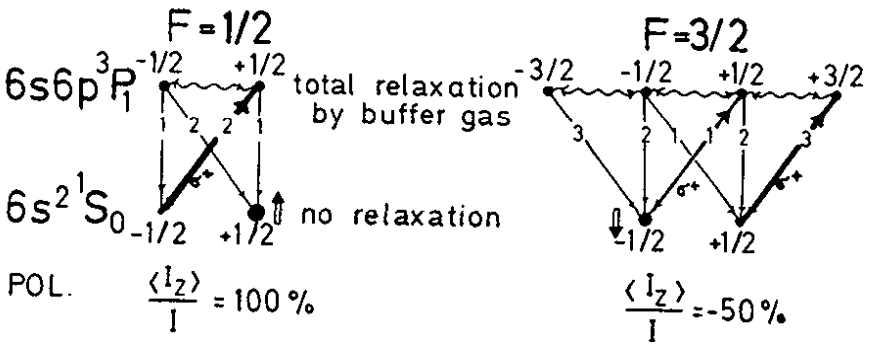

Fig. 3.2: OP cycle for a mercury isotope with I = 1/2 between states J = 0 and J = 1.

The angular distribution of radiation emitted by an oriented ensemble of nuclei is given by

$$W(\vartheta) = \sum_k A_k f_k P_k(\cos \vartheta) \qquad (3.1)$$

where A_k is a correlation coefficient in the decay, P_k is the Legendre Polynomial and f_k is the k'th moment of orientation defined by

$$f_k(I) = \binom{2k}{k}^{-1} I^{-k} \sum_m \sum_{\nu=0}^{k} (-1)^{\nu} \frac{(I-m)!\ (I+m)!}{(I-m-\nu)!\ (I+m-k+\nu)!} \binom{k}{\nu}^2 n_m \qquad (3.2)$$

n_m is the normalized population number of the substate $m_I = m$. Whereas f_o measures the degree of isotropic population, f_1 is the ordinary polarization P_I, relevant for ß-decay asymmetry through the asymmetry coefficient

$$A_1 = \left\langle \frac{v}{c} A \right\rangle_{\text{spectrum}} \qquad (3.3)$$

v is the velocity of the ß-particle and A the asymmetry parameter, both averaged over the ß-decay spectrum in question. For exotic nuclei this spectrum is usually very complex and not known in such detail that A_1 could be estimated. Competing channels with opposite sign of A tend to diminuish A_1 to uncomfortably small values in ß-RADOP applications.

The second moment

$$f_2 = (1/I^2) \sum_m (m^2 \cdot n_m) - (1/3)\ I(I+1) \qquad (3.4)$$

is the so-called alignment and the most important one in γ-RADOP since A_2 dominates the anisotropy of γ-decay of oriented nuclei for all multipolarities.

Since $f_K \equiv 0$ for $I \leq k/2$, ß-RADOP requires $I \geq 1/2$ and γ-RADOP $I \geq 1$. These rules exclude, for instance, IS measurements of even nuclei which obviously restricts the systematic application of RADOP. γ-RADOP is not limited to excited nuclear levels, since ß-decay from the ground state transfers the alignment to excited levels of the daughter whose γ-decay may then be measured. Since ß-decay is sensitive to odd and γ-decay to even moments of orientation, the pair of detectors observing the angular correlation are mounted under 0° and 180° in the former and under 0° and 90° in the latter case (compare Fig. 3.3).

A special advantage of OP is its capability of inverting the polarization in a fast and very gentle manner, just by switching the polarization of light from σ^+ to σ^-. This enables the suppression of any kind of instrumental asymmetry by taking the relative difference signal of ß countrates

$$S_ß = (N_1^+N_2^- - N_1^-N_2^+) / (N_1^+N_2^- + N_1^-N_2^+) = 2\,A_1 / (1+A_1^2) \qquad (3.5)$$

where N_1^+ is the countrate on detector (1) at (+) polarization etc. The detection limit of $S_ß$ is determined only by statistical accuracy. Signals ≈ 0.1 % have been observed unambiguously. In case of γ-RADOP one prefers to irradiate the pumping light perpendicular to the external field H_o and with linear polarization.

Turning this polarization axis by 90° changes the sign of f_2, i.e. from polar to equatorial alignment. Hence we can define a signal S_γ in analogy to S_β (eq. (3.5)).

The most serious danger in RADOP experiments stems from unpolarized radioactive material which is sticking to the walls of the resonance vessel and hence does not participate in the OP cycle. This probelm is avoided, or at least minimized, in on-line experiments on short-lived isotopes, where the radioactive species is produced or deposited in the center of the vessel and decays already on its diffusion path through the buffer gas to the walls. The first ß-RADOP experiment on short-lived alkalis strictly followed this scheme (Kö 69). A deuteron beam passed a resonance vessel filled e.g. with ^{36}Ar giving rise to the reaction $^{36}Ar\ (d,n)\ ^{37}K \xrightarrow[\beta^+,\ 1s]{} {}^{37}Ar$. The magnetic moment of ^{37}K and some other mirror nuclei were measured this way (reviewed e.g. in references (Ot 85, 85b)).

Off-line experiments are possible only for a few noble and volatile elements which do not stick to the walls. The first γ-RADOP experiment which was conducted on ^{203}Hg ($T_{1/2}$ = 47 d) is an example of this type (Ca 73).

Fig. 3.4 shows the set-up for RADOP experiments on short-lived Hg isotopes at ISOLDE which opened the era of optical investigations at on-line mass-separators (Bo 71, Hu 76). Collector foils are mounted two both sides of a flange, receiving the mass-separated beam on one side and releasing it on the

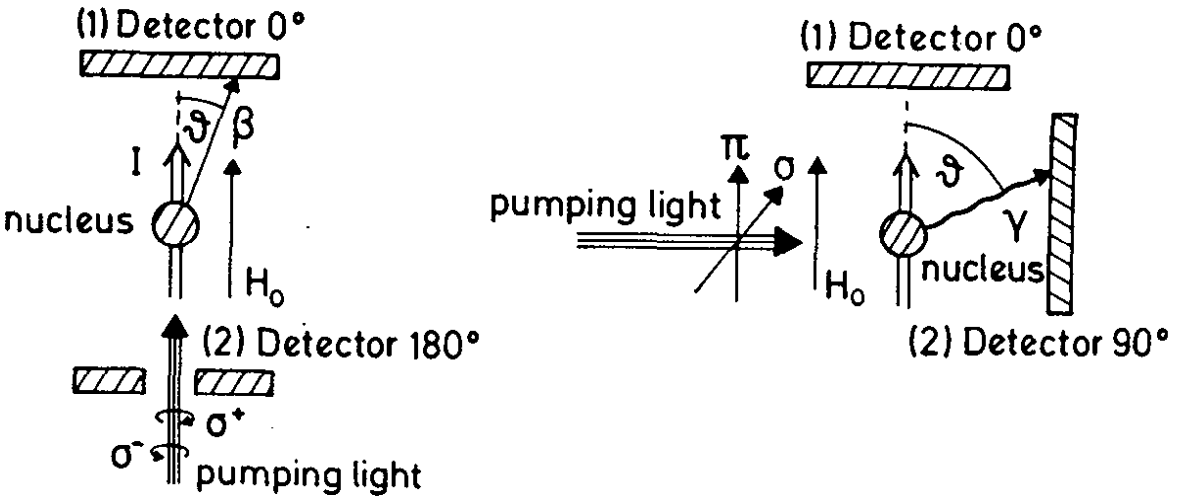

Fig. 3.3: Geometries in ß- and γ-RADOP with respect to an external field H_o.

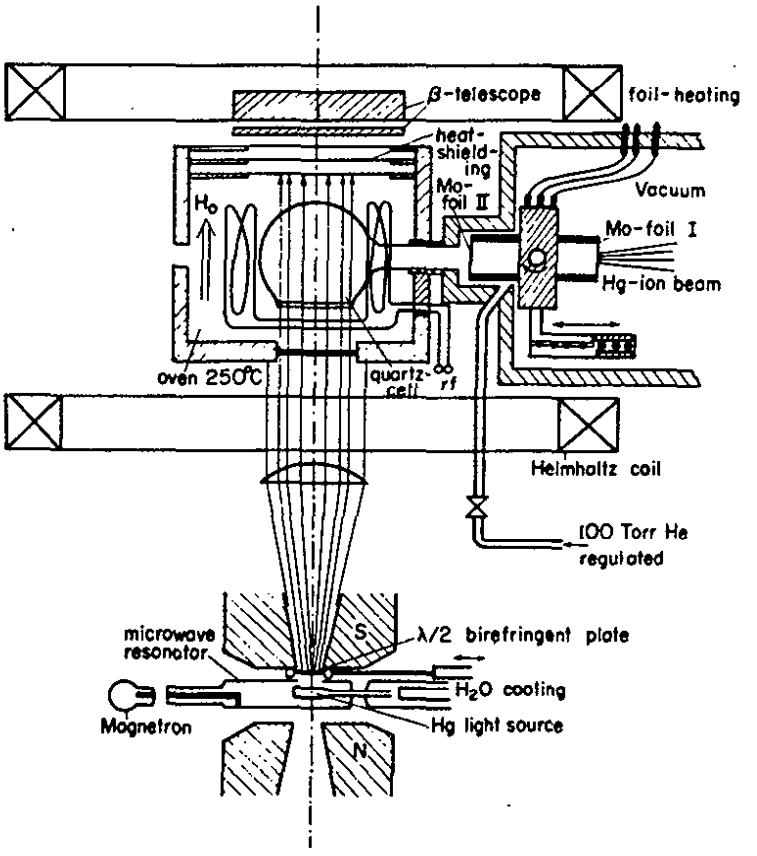

Fig. 3.4: Apparatus used for RADOP experiments with on-line mass-separated, short-lived Hg isotopes (Hu 76).

other after interchange of position and heating. OP is performed in the presence of He buffer gas by circularly polarized resonance light ($6s^2\ ^1S_0 \rightarrow 6s6p\ ^3P_1$, λ = 254 nm) from a spectral lamp containing an even stable isotope, e.g. ^{198}Hg. Since hfs and IS in this line are large as compared to the Doppler width, a Zeeman component of the lamp isotope is tuned to the position of the hfs components of the unstable isotopes. This gives rise to scanning signals of the asymmetry S_β as shown in Fig. 3.5 for the case of ^{189}Hg. The position of the signals directly display hfs splitting and IS.

In addition to this information, g_I can directly be determined by applying NMR to the oriented ensemble of nuclei in the resonance vessel. At the resonance point

$$\nu_o = \gamma H_o = g_I \mu_n H_o/h \qquad (3.6)$$

(μ_n = nuclear magneton, H_o = external field) the orientation and hence the asymmetry signal S_β is destroyed as shown in the insert of Fig. 3.5. In that experiment ß-RADOP signals were obtained in the Hg series $181 \leq A \leq 205$. A particular surprise was the discovery of a shape transition from small oblate to strong prolate deformation at ^{185}Hg observed by a strong discontinuity of the IS (Bo 72, Bo 76) (compare section 4.7.).

At the very ends of this chain the yield curve drops down to about 10^3 atoms/s. Since the lifetime is a few seconds only, the number of atoms in the vessel is of same order. Still a satisfactory signal-to-noise ratio is obtained at an asymmetry

level of $S_\beta \approx 4$ %. For comparison, a usual fluorescence signal would optimize at a density of 10^{10} to 10^{12} atoms/cm^3. As seen from todays experience, these early ß-RADOP experiments surpassed the sensitivity of many of the later laser spectroscopic experiments by orders of magnitude. But their scope remained quite restricted. In the course of discussing the various methods it will become clear that the question of sensitivity and applicability of a particular method is always complex and subjected to many experimental circumstances. General statements are of little use and poor prognostive power, therefore.

An example of γ-RADOP is given in Fig. 3.6. The vessel contained ^{193}Hg together with its isomer I = 13/2. Both decay to ^{193}Au the γ-spectrum of which is being measured by a GeLi-detector. The upper part shows the spectrum of the anisotropy signal (from one detector only) defined here as

$$S_\gamma = (N_1^+ - N_1^-) / (N_1^+ + N_1^-)^{1/2}. \qquad (3.7)$$

The squareroot in the denominator of eq. (3.7) normalizes S_γ such that it is measured in units of one statistical standard deviation. Strong signals of different sign are seen in many transitions. In these data abundant information on the multipolarities of the decay scheme is contained which hasn't been analyzed yet. The revived interest in detailed nuclear spectroscopy might stimulate more work in this direction in the future, especially on the side of nuclear orientation (St 85b).

Fig. 3.7 shows NMR curves from γ-RADOP on the (M1/E2)-transition in ^{203}Hg (Ca 73). The width increases with the rf

Fig. 3.5: ß-RADOP on ^{189}Hg. The upper part shows the splittings of the resonance line for the lamp isotope ^{198}Hg and for the unstable ^{189}Hg in their relative positions. Below, the scanning signal of $S_ß$ is given. The insert shows the NMR signal of ^{189}Hg (Hu 76).

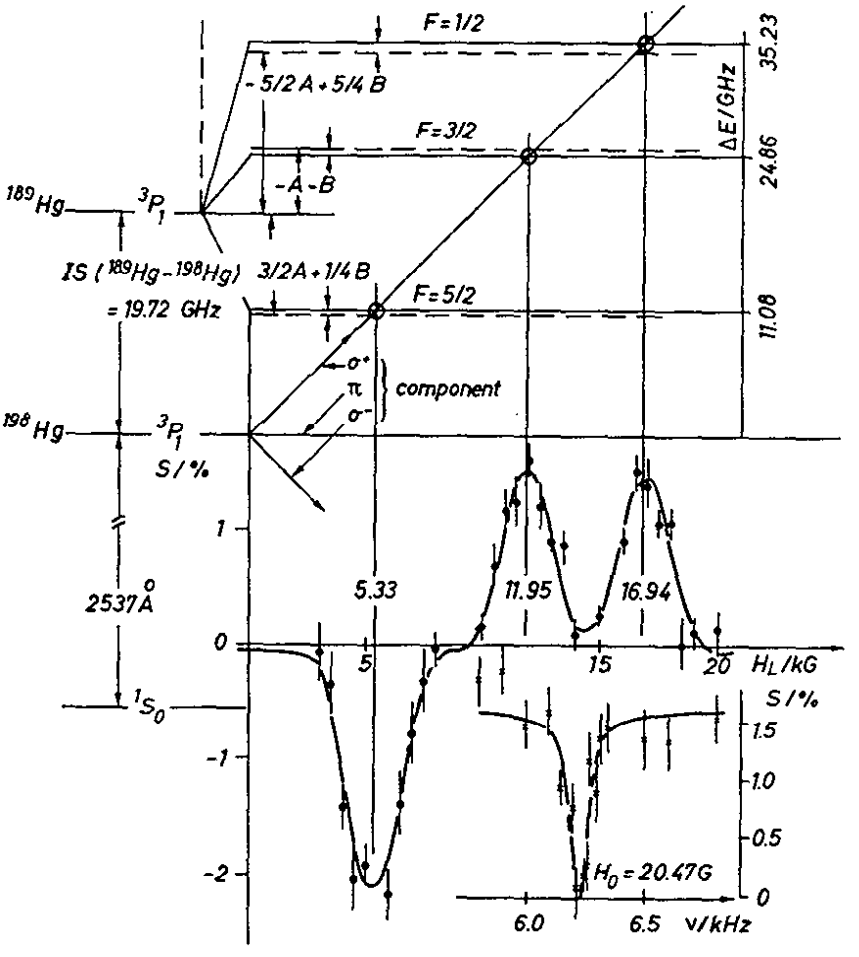

Fig. 3.6: Upper part: Normalized γ-RADOP signal in the decay spectrum of $^{193}Hg^{m}$. The anisotropy is calculated in each channel. Lower part: The decay spectrum itself (Hu 76).

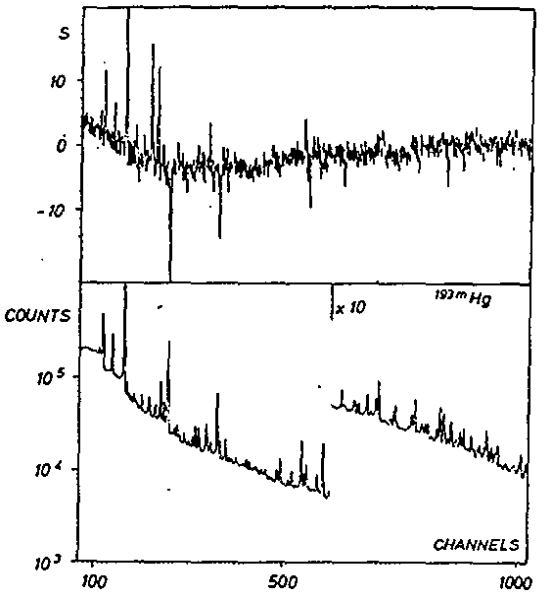

power, whereas the shape is characteristic for the orientation parameter f_K and multipolarity involved (Ma 71).

A very interesting but also difficult problem was tackled by a RADOP experiment on the fission isomer ^{240m}Am ($T_{1/2}$ = 1 ms), dedicated to the determination of the isomer shift (Be 79b). A huge shift of the order of 2 Å is expected due to the extraordinary large deformation of the isomeric state in the second minimum of the potential energy surface. Level structure and BE2 values of fission isomers indicate an ellipsoidal shape with a ratio of axis of 2 : 1. Fig. 3.8a shows the experimental set-up. ^{240m}Am is produced by a Li beam from a thin ^{238}U-target, recoiling the reaction product into the He buffer gas of the resonance vessel were it comes to rest. In contrast to earlier RADOP experiments one took advantage of using a broad band, tunable dye laser instead of a spectral lamp for polarizing up the Am atoms. Am is the only actinide with a spherically symmetric atomic ground state (the configuration is $5f^7 7s^2\ ^8S_{7/2}$) and hence suited for RADOP, since the relaxation rate of the polarization in the buffer gas atmosphere is moderate. Broad band running ($\Delta\nu$ = 0.5 Å) facilitates the search for the resonance line by taking large tuning steps. This was essential in view of the low event rate (≈ 200/h). On the other hand, the light intensity which is necessary to achieve a certain pump rate rises in proportion with the band width. Only powerful lasers can meet these requirements. The RADOP signal could be obtained in this particular case from the anisotropy of spontaneous fission with respect to the axis of orientation. This signal is absolutely

free from background. Fig. 3.8b shows a scan of the coincidence rate of the two fission fragments detected by two opposite proportional counters. A 30 % dip is observed at the expected resonance position, at which the nuclear spins should line up along the laser beam axis. With a somewhat different arrangement where production and pumping section are separated this experiment is going to be repeated by another group in order to strengthen the statistical confidence level of the resonance and to resolve the hfs eventually (Ba 86).

Another variant of RADOP was recently realized off line by Calaprice et al. (Ca 85, 85b) for the example of radioactive Xe isotopes 131^m, 133, 133^m. The noble gas was spin-polarized by gas kinetic collisions with an optically pumped Rb vapor in a resonance vessel. During the collision the two atoms form a transient molecular state in which they share the spin polarization of the Rb valence electron which couples to the Xe spins and polarizes them. The polarization is monitored by γ-decay anisotropy. The extremely slow relaxation rate allows ultimate NMR resolution. So far a linewidth of 0.5 Hz was reached, still dominated by power broadening. This experiment shall finally serve to set a better lower limit for the electric dipole moment of a nucleus by measuring the resonance shift in an external electric field. Quite recently the group applied this method to ^{209}Rn and performed the first direct determination of a g_I-factor of this element (Ca 86). This measurement enabled the calibration of hfs splittings in spectral lines of Rn which has been investigated recently for a long series of isotopes (Bo 87).

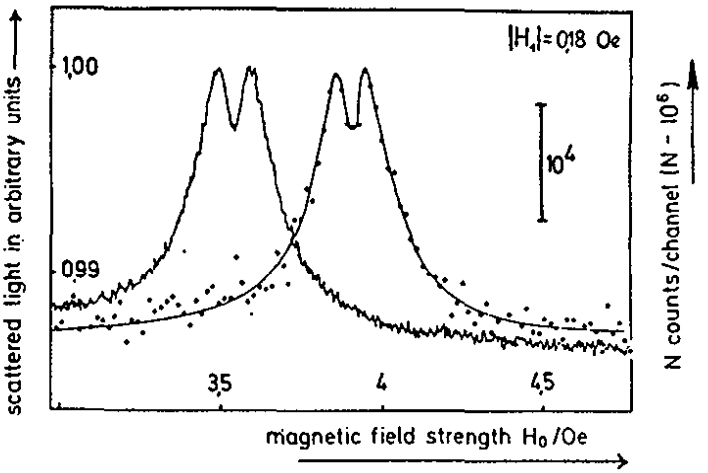

Fig. 3.7: NMR resonance in γ-RADOP signal of ^{203}Hg (right) in comparison with the ordinary optical pumping NMR signal of ^{201}Hg (Ca 73).

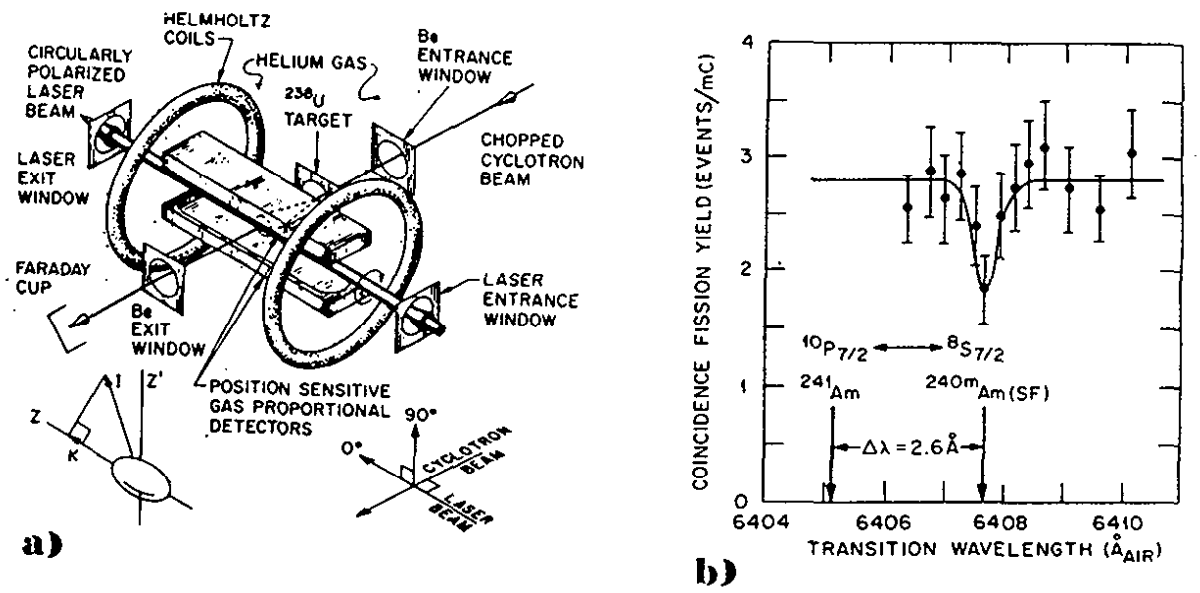

Fig. 3.8: Fission-RADOP experiment on ^{240m}Am (Be 79b), a) experimental set-up; b) scan of the coincidence rate of the fission fragments as function of laser frequency. The arrows indicate the IS with respect to ^{241}Am.

In section 3.7.2c. we will come back to RADOP again in connection with collinear laser spectroscopy. In summary the RADOP method still proves to be fruitful for specific, dedicated experiments; but in the field of systematic survey experiments off stability it has been displaced by the more general and less cumbersome laser spectroscopic methods, discussed below.

3.3. Principles of Laser Spectroscopy

When tunable lasers started to revolutionize optical spectroscopy in the early seventies several laboratories were engaged in developing and testing methods with particular emphasis on reaching simultaneously high sensitivity and high resolution. Quite a number of these attempts turned out to be useful for investigating unstable isotopes and could be adapted to on-line conditions. Before going into experimental details the principal physical situation in laser spectroscopy will be briefly described.

Let the laser radiation drive transitions between atomic levels (1) and (2) which may (or may not) couple to a third level (or a group of levels) by spontaneous emission or relaxation rates Γ_{23}, Γ_{31} (compare Fig. 3.9). An atom with resonance frequency ν' in the lab frame will offer to a photon of frequency ν an absorption (or induced emission) cross section

$$\sigma(\nu-\nu') = \frac{\lambda^2}{2\pi} \frac{\Gamma_{21}/\Gamma_{2\text{total}}}{1+(4\pi(\nu-\nu')/\Gamma_2)^2} \qquad (3.8)$$

where λ is the wave length of the photon and $\Gamma_2 = 2\pi\Delta\nu_h$ the total decay rate of level (2) which determines the so-called homogenous (or natural) linewidth $\Delta\nu_h$ of the Lorentz profile (3.8). At the resonance point $\nu = \nu'$ and under the assumption that Γ_2 is comparable to Γ_{21} the cross section for an optical photon is of the order

$$\sigma(\nu=\nu') = \mathcal{O}(10^{-9}\ \mathrm{cm}^2). \qquad (3.9)$$

This is an enormous dimension for an elementary system and explains the effectivness of laser spectroscopy. Let us assume for instance a laser power of 10 mW/cm² which is reached by any continuous wave (cw) laser; this power corresponds to a photon beam intensity $j_{Ph}(\nu)$ of the order of 10^{17}/cm² s; then the induced transition rate $\Gamma^{(i)}$ already reaches the level of 10^8/s which is comparable to the spontaneous decay rate Γ_{21} of allowed optical transitions. $\Gamma^{(i)} > \Gamma_{21}$ marks the regime of saturation where the populations in the excited (2) and the ground level (1) are equalized in the absence of branching ($\Gamma_{23} = 0$)*). A single atom excited to saturation hence will emit already about 10^8 fluorescence quanta per second which form a strong signal. In an experiment on a single, trapped Ba ion this fluorescence signal has been observed by the naked eye, indeed (Ne 78).

In most cases, however, branching leads to OP into a third state (3) which is metastable for the time of observation T, that is $T \cdot \Gamma_{31} << 1$. This "mute" level can be one of the hfs levels of the ground state, for instance. In this case the excitation emission cycle stops after a total number of fluore-

Footnote: (page 44)

*) Whereas eq. (3.8) is a result of perturbation theory for a white photon spectrum, the interaction of a strong (i.e. classical) monochromatic field with a two level system is described exactly by an analogue to Bloch's equations for the motion of a spin 1/2 in an external magnetic field. At resonance the transient solutions show oscillations of the population numbers with the so-called Rabi frequency $\omega_1 = E\,\mu_e/\hbar$ (E = electric field strength of the laser, μ_e = transition electric dipole moment). The oscillation decays with Γ_2 towards the steady state population. The line width of the resonance curve of the steady state solution increases with ω_1 as $\Delta\omega_h \approx \sqrt{\Gamma_2^2+\omega_1^2}$ (power broadening). Rabi frequency and power broadening are hence proportional to the squareroot of the laser power. The physical reality in laser spectroscopy usually corresponds neither to the white nor to the monochromatic solution but is complicated in addition by the "inhomogeneous" Doppler width $\Delta\nu_D$ (Ab 61, Sh 76).

scence quanta of $(1 + \Gamma_{21}/\Gamma_{23})$ has been emitted per atom in the average. Usually this number does not exceed 1 very much. Therefore, many attempts have been made in searching for another signature of optical resonance excitation which is more efficient and less sensitive to background than the detection of fluorescence quanta. RADOP was one example, a number of others will be described below. Experience has taught us, however, that in the absence of OP and for long observation times the fluorescence detection is not easily beaten in sensitivity. Moreover, it is the easiest and most general detection method.

In case of Doppler broadening the cross section is a convolution of a Lorentzian and a Gaussian (so-called Voigt profile):

$$\sigma_D(\nu) = \frac{(\lambda^2/2\pi)\ (\Gamma_{21}/\Gamma_2)}{\sqrt{\pi}\ \Delta\nu_D} \int_{-\infty}^{+\infty} \frac{\exp[-(\nu'-\nu_o)^2/(\Delta\nu_D)^2]}{1 + (4\pi(\nu-\nu')/\Gamma_2)^2}\, d\nu' \qquad (3.10)$$

ν_o is the resonance frequency for the atom at rest. For a thermal gas the (single) 1/e width

$$\Delta\nu_D = (\nu_o/c)\ \sqrt{2kT/m} \qquad (3.11)$$

is of the order of 1 GHz and exceeds the natural one by a factor of 100 to 1000. By the same factor the cross section (3.10) is flattened as compared to the Doppler-free case ($\nu' \equiv \nu_o$). That means that only a small fraction of the order $\Delta\nu_h/\Delta\nu_D$ of the atoms can participate at a given excitation frequency ν in the transition.

3.4 Laser Excited Fluorescence in Resonance Cells

The following dicussion of the individual experiments will not follow the chronological order but will start with the conceptually simplest one.

A straight forward way to laser excited fluorescence spectroscopy on-line starts from the RADOP set-up in Fig. 3.4. One replaces the spectral lamp by a tunable dye laser and the ß-counters by a photomultiplier. Fig. 3.10 shows the modified apparatus used for measuring a number of even Hg isotopes (Kü 77) as well as $i_{13/2}$-isomeric states (Da 78, Da 79) down to ^{184}Hg and $^{185}Hg^{m}$, respectively. Both had evaded the earlier RADOP experiments, the even isotopes for principal reasons (I = 0), the isomers because of ß-asymmetry parameters being apparently too small.

The resonance wavelength of 254 nm for Hg cannot be directly generated in a dye but by frequency doubling a laser beam of wavelength 508 nm in a birefringent crystal. Since this non-linear effect is proportional to the square of the incoming intensity, it is advisable to choose a pulsed laser with high peak power instead of a cw laser. The primary nitrogen pump laser yields ≈ 3 ns wide pulses of ≈ 100 kW power at a repetition rate ≈ 100 Hz; the frequency-doubled pulse has a power of the order of 1 kW and a spectral width of about 2 GHz which covers the Doppler-width. This latter circumstance together with the high power enables to almost saturate the transition at resonance for the whole ensemble and to maximize the fluorescence peak.

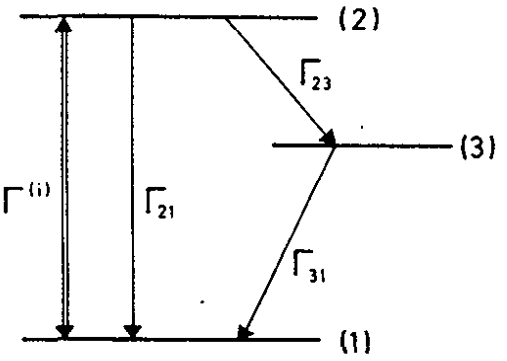

Fig. 3.9: Schematic level diagram for laser spectroscopy. The laser drives transitions between levels (1) and (2) with the induced rate $\Gamma^{(i)}$. Γ_{kl} are decay rates. Level (1) is supposed to be the atomic ground state.

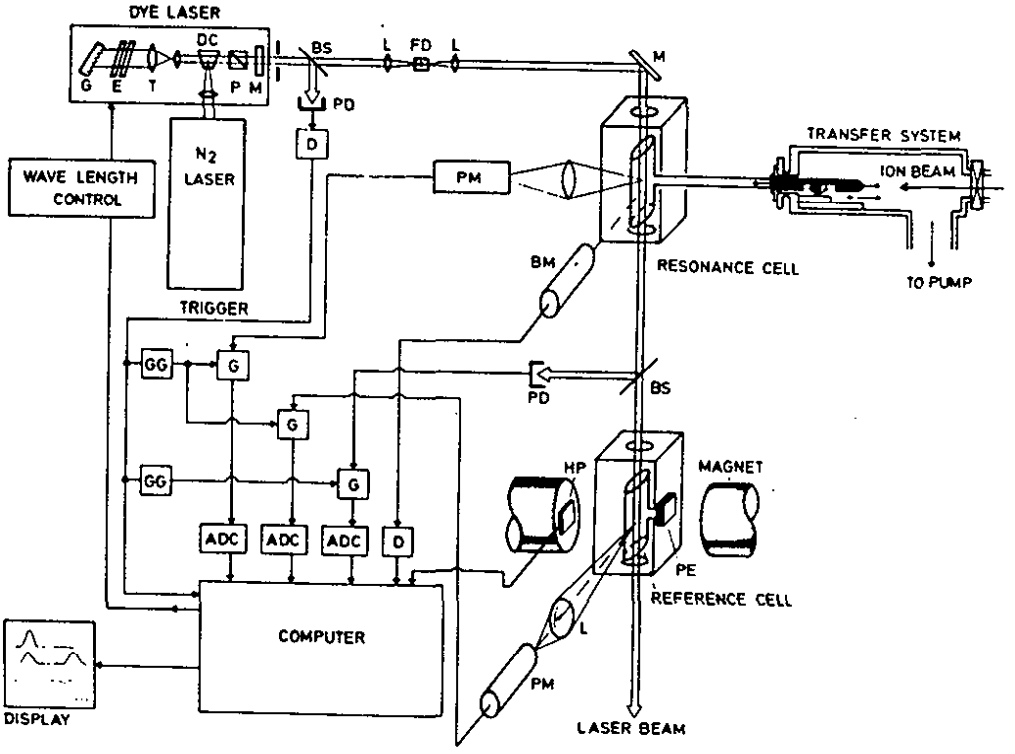

Fig. 3.10: Experimental set-up for laser spectroscopy on short-lived even Hg isotopes. G: grating, E: etalon, T: beam expanding telescope, DC: Dye cell, P: polarizer, M: mirror, FD: frequency doubling crystal, L: lens, PM: photomultiplier, MO: monitor for laser intensity, G: gate, ADC: analog to digital converter (Kü 77, Da 78).

Fig. 3.11, taken from ref. (Kr 79), shows the scan of the hfs spectrum of ^{187}Hg containing the components from the ground state as well as from the isomeric one. The laser frequency is calibrated by simultaneously scanning Zeeman components from stable isotopes at a fixed field.

A modification of the method led to a direct determination of nuclear spins of Hg isomers (Kr 79), utilizing the fact that the laser excitation is performed by very short pulses, followed by the slow decay of the atomic state with a lifetime of 10^{-7} s. If a small magnetic field is applied to the resonance vessel, the total spin $F = I + J$ performs a Larmor precession in the excited state, resulting in a rotation of the angular distribution of the emitted photons. Fig. 3.12 shows the number of photons observed as a function of time after the laser shot. For electric dipole radiation, the modulation on the decay curve occurs at twice the Larmor frequency, which is connected to the spin via the g_F-factor:

$$g_F = g_J\,[F(F+1) + J(J+1) - I(I+1)]/2F(F+1). \qquad (3.12)$$

$I = 13/2$ has been confirmed for all the isomers, including the questionable case of ^{185}Hg^m. The method of laser-excited fluorescence in cells has further been applied to a series of Cd isotopes $102 \leq A \leq 120$ (Bu 81,87) and to some neutron-deficient Au isotopes (St 85c). The latter experiment was the first to be conducted on radioactive isotopes of a refractory element. It required excogitated high temperature technology with saphire cells heated to 1000°C etc.

Fig. 3.11: Upper part: hfs spectrum of ground state (I = 3/2) and isomer (I = 13/2) of the $6s^2\ ^1S_0$ - $6s6p\ ^3P_1$ (λ = 2537 Å) line of ^{187}Hg. Lower part: reference spectrum of the σ^+-Zeeman components of the even, stable Hg isotopes (Kr 79).

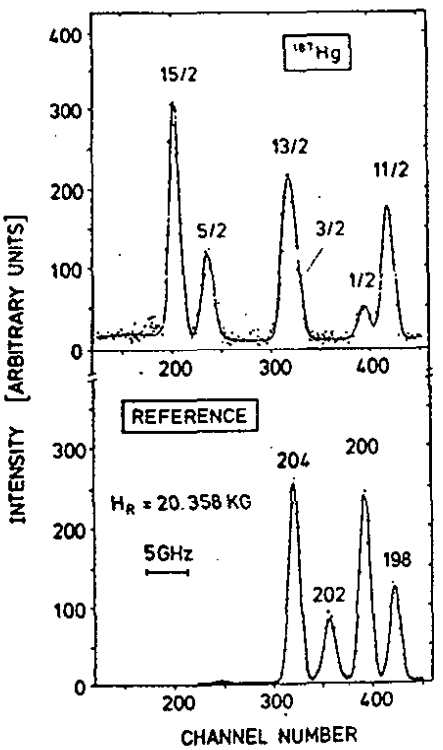

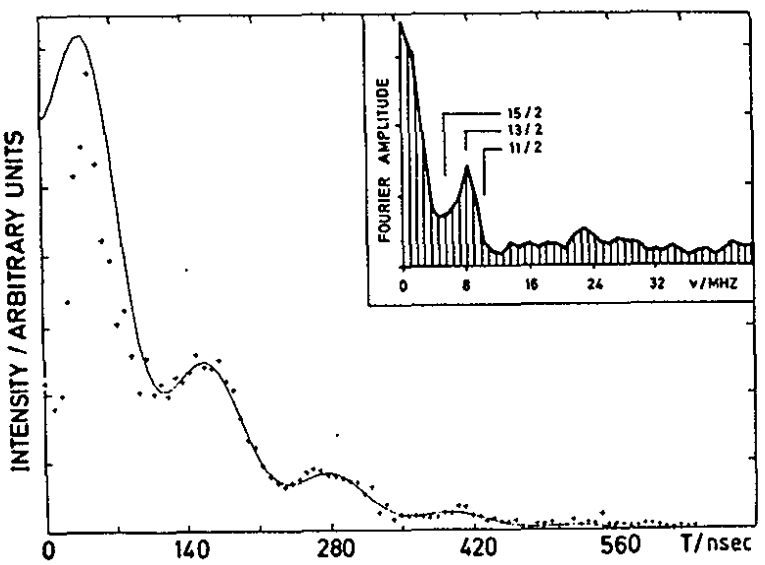

Fig. 3.12: Time-dependent perturbed angular correlation in the fluorescence from the F = I = 13/2 hfs level of $^{187}Hg^m$ in a magnetic field of 91.1 G. A damped oscillation is fitted to the data points. Owing to prompt stray light, the photomultiplier is overloaded in the first 80 ns. The inset shows the Fourier transform of the signal peaking at the Larmor frequency expected for I = 13/2 (Kr 79).

The sensitivity of fluorescence spectroscopy with pulsed lasers was seriously limited by their low duty cycle ($\approx 10^{-6}$). An amount of $\approx 10^{9}$ atoms in the cell was necessary to achieve a decent signal. Only a few percent of them were in the region of observation, the others filling the dead volume. With modern copper vapor or excimer lasers one could gain a factor of 100 in duty cycle but would still remain far below the optimum of using a cw laser. From this standpoint of view it would be advisable to choose, instead, elements with low-lying resonance lines, accesible to cw lasers. However, low excitation energies go together with high chemical affinity (like for the alkalis and alkaline earths), which causes the atoms to stick to the wall at the first encounter already.

3.5. Laser Spectroscopy on Collimated Atomic Beams

The experiments to be described in this section avoid the difficulties specific to resonance vessels by switching to atomic beam techniques. This offers, in addition, the chance to reduce the Doppler width by a large factor which is necessary for application to lighter elements in order to resolve hfs and IS. The chances to achieve high sensitivity together with high resolution in laser spectroscopy on atomic beams have been explored by Jaquinot and collaborators for various detection schemes and are discussed in ref. (Ja 76). The experiments described in sections 3.5.1. and 3.5.2. trace back to considerations along these lines.

3.5.1. Laser Excited Fluorescence from an Atomic Beam

Excitation of a collimated, thermal atomic beam obviously leads to a reduction of the Doppler width by a factor corresponding to the truncation of the atomic velocity in the direction of light. It is also clear that resolution can only be gained on cost of signal height since the collimation cuts down the solid angle of the atomic beam observed. For a simple geometry as sketched in Fig. 3.13 the necessary integrations can be carried out analytically. In the absence of OP and for moderate light intensities below the saturation point the rate of fluorescence photons emerging from the illuminated volume V is given by

$$R = j_{Ph}(\nu)\, n_V\, V\, \sigma_{Dc}(\nu) \qquad (3.13)$$

where

$$n_V \approx n_o \frac{A}{4\pi r^2} \qquad (3.14)$$

is the total density of atoms in V, whereas n_o is the one in the oven. $\sigma_{Dc}(\nu)$ is the frequency-dependent cross-section (3.10) but now taken for the "collimated" Doppler width

$$\Delta\nu_{Dc} = \Delta\nu_D \sin\delta_o = \frac{\nu_o}{c}\sqrt{2kT/m}\,\sin\delta_o. \qquad (3.15)$$

The other symbols are explained in Fig. 3.13. The gain in resolution is given by the sine of the collimation angle δ_o, and

the loss in density by the solid angle under which the orifice of the oven is seen in the observation volume.

Let us assume now more realistically that in practice OP limits the number of fluorescence photons to about 1 for each atom passing V; furthermore the laser intensity may be adjusted such, that this limit is just reached at the resonance peak ν_o. Then the peak count rate is given by

$$R(\nu_o) \approx I \frac{A'}{\pi r^2} \qquad (3.16)$$

where I is now the total current of atoms leaving the oven and A' is the cross-section of the observation volume. Assuming a typical collimation of the beam to 25 mrad in both directions eq. (3.16) implies a geometric reduction factor of ≈ 5000. Fluorescence photons may be detected with a solid angle of $\Delta\Omega/4\pi \approx 5$ % and a quantum efficiency of the PM of 10 %. From these numbers one calculates a total detection efficiency for an atom of only 10^{-6}.

Nevertheless this technique has proved to be very fruitful in off-line applications to the following isotopic chains: ^{40}Ca to ^{48}Ca (Be 80, An 82), $^{80\text{-}90}$Sr (Bu 85, An 86b), ^{110}Sn to ^{125}Sn (An 86b), ^{124}Ba - ^{138}Ba (No 78, Be 79), and ^{196}Pb to ^{214}Pb (Th 83, An 86c). The experiments have concentrated on the particularly interesting cases of magic proton elements Z = 20, 50, 82. Fig. 3.14 shows the set-up used by the Karlsruhe group for Ba and other elements (No 78). The atomic beam,

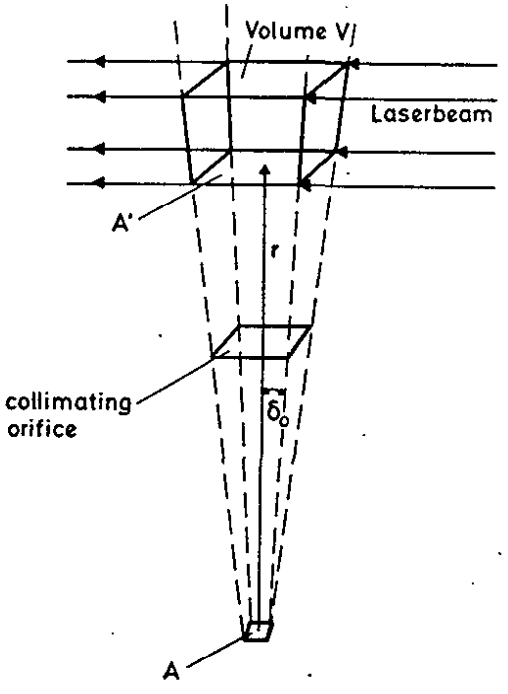

Fig. 3.13: Geometry for exciting a collimated atomic beam in the volume V. The beam emerges from an oven with orifice A.

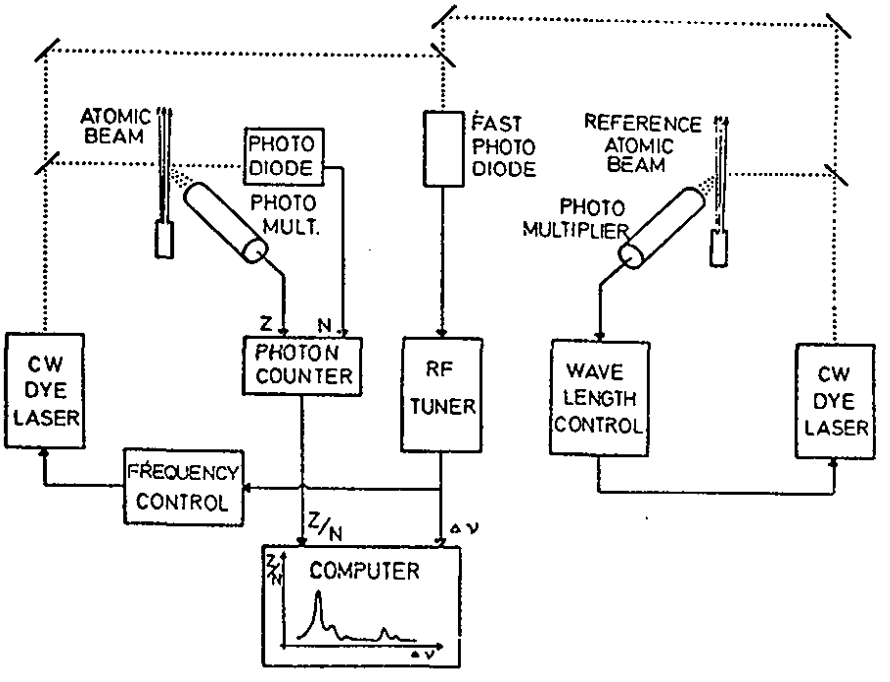

Fig. 3.14: Set-up for fluorescence spectroscopy from a collimated atomic beam of off-line mass-separated unstable Ba isotopes excited by a cw dye laser. On the left the unstable beam; on the right the stable reference beam (No 78).

evaporating from an off-line mass-separated sample of an unstable Ba isotope is excited by a cw dye laser tuned periodically through the resonance. The laser frequency is controlled by heterodyning it with a second laser which is stabilized to the atomic resonance line of a stable Ba isotope.

Fig. 3.15 shows a recording of ^{126}Ba ($T_{1/2}$ = 97 min) (Be 79). The line width has shrinked to about 50 MHz which is an enormous gain compared to the cell experiments. ^{126}Ba was produced in an amount of $3 \cdot 10^{11}$ atoms. A fraction of $6 \cdot 10^{10}$ has been used in a single recording over 6 min. From these numbers one calculates that the average number of atoms, present in the observation region, was only about 1. Seen this way, it is astonishing that the method can compete with the cell technique. But the 100 % duty cycle of the cw laser compensated for most of the handicaps; some other factors, such as higher oscillator strength and better stray light suppression, helped in addition.

3.5.2. Laser-Induced Optical Pumping (LIOP) of an Atomic Beam with Stern-Gerlach Analyzer

This experimental method was the first in the field of on-line laser spectroscopy. It has been developed by a collaboration of the Institutes René Bernas and Aimé Cotton, both at Orsay, and is particularly suited for investigating alkalis. The pilot experiment was run on-line with a 150-MeV proton beam at Orsay, producing Na isotopes in the range ^{21}Na to

^{25}Na (Hu 75). Later an improved apparatus was put on-line with the 24-GeV proton beam at CERN which yielded extremely neutron-rich Na isotopes by fragmentation of U. Laser spectroscopy could be performed up to ^{31}Na (Hu 78). Finally the experiment was connected to the ISOLDE facility measuring all other series of alkalis, namely ^{38}K to ^{47}K (To 82b), ^{76}Rb to ^{98}Rb (Th 81), ^{118}Cs to ^{146}Cs (Th 81b, Co 87), ^{207}Fr to ^{223}Fr (Li 80, Co 85,87).

The principal of the method shall be explained from Fig. 3.16 which shows the decisive elements of the apparatus used in the experiments at ISOLDE. The mass-separated ion beam is stopped in a hot Ta tube covered with Y in order to reduce the work function of the surface below the ionization potential of alkalis. Therefore, the stopped particles predominantly reevaporate as neutral atoms and form an atomic beam which undergoes OP by the transverse laser beam. From the example of a level diagram on the lower part of Fig. 3.16 one learns that pumping via transitions a) and b) depopulates the upper hfs level (F = 2) of the atomic ground state. For the spontaneous reemission from the excited state also channels c) and d) are open which connect to the lower hfs level (F = 1). Thus the lower level is enriched on cost of the upper. Pumping via channels c) and d) has the opposite effect.

After the pumping section, the beam enters a strong magnetic sextupole field where the Paschen-Back effect forms two groups of Zeeman levels with m_j = 1/2 and -1/2. Only the rising group is focussed by the Stern-Gerlach force of the field gra-

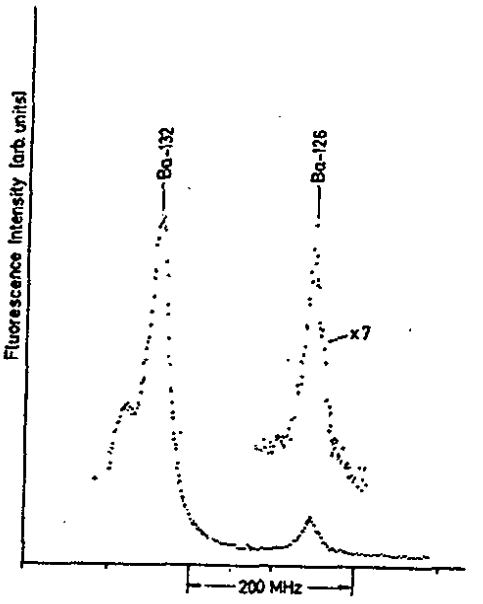

Fig. 3.15: Fluorescence spectrum of the $6s^2\ ^1S_0 - 6s6p\ ^3P_1$ ($\lambda = 5535\text{Å}$) line taken from a sample of ^{126}Ba. The resonance line is slightly powerbroadened by high laser intensity in order to profit from multiple excitation of each atom (Be 79).

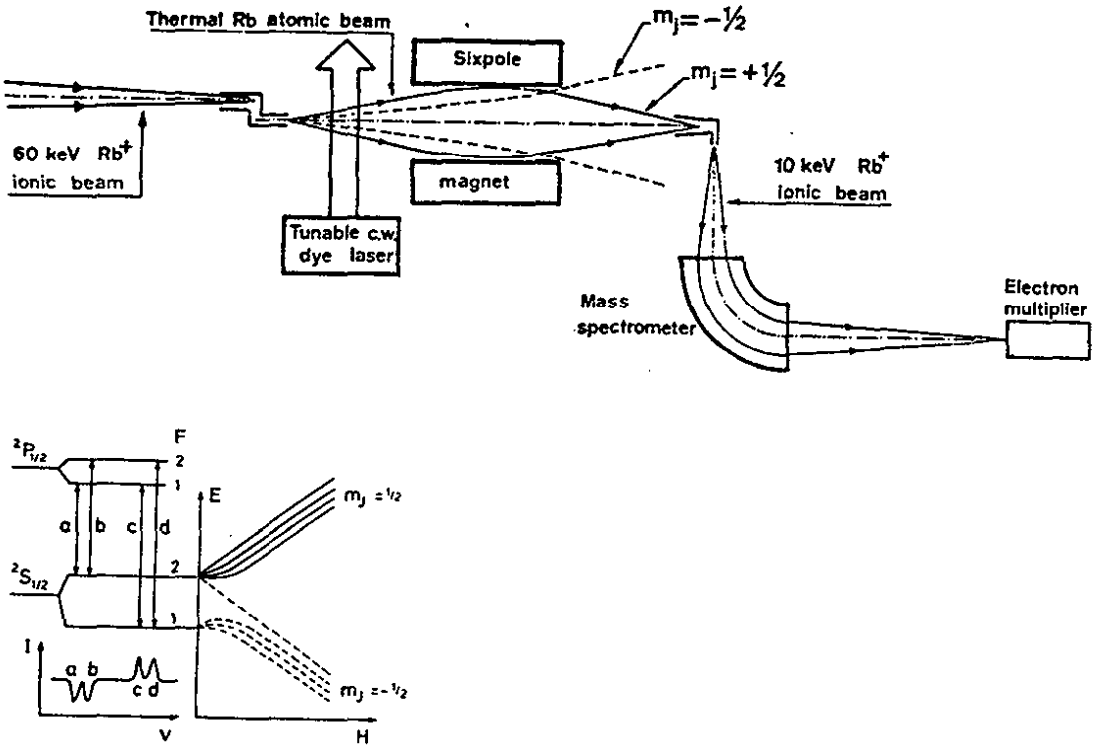

Fig. 3.16: Upper part: Experimental set-up of laser-induced optical pumping (LIOP) of an atomic beam of alkalis detected by magnetic state selection (Th 81).
Lower part: Hfs level diagram of the D_1 resonance line of an alkaline isotope with I = 3/2. The inset shows schematically the spectrum of the four pumping signals.

dient; the other one is defocussed. Thus pumping via a) and b) decreases, via c) and d) increases the current on the detector, giving rise to the pattern sketched in the figure. Selective and efficient detection of the atomic beam is achieved by an advanced version of the well-known Langmuir-Taylor detector. A hot tungsten tube is placed at the focus of the sextupole, converting by surface ionization alkali atoms into ions, which are then mass-separated and counted by a multiplier.

Fig. 3.17 displays the whole series of signals obtained in the chain of Na isotopes (Hu 78). The large splitting corresponds to the hfs of the 3s ground state, the small one to that of the excited 3p $^2P_{1/2}$ state. The centre of gravity displaces by the isotope shift which is dominated by the mass shift. If one compares the small hfs splitting of the excited state with the huge one in Hg (compare Fig. 3.5) one immediately recognizes the importance of reducing the Doppler width in the case of light elements.

The accuracy of determining the ground state splitting could be improved recently by a factor of 1000 over these optical measurements by employing rf-transitions between the hfs levels in the region between the pumping zone and the Stern-Gerlach analyzer thus completing the set-up to a type of Rabi apparatus (Du 86). Out of the many important results obtained by the LIOP method (see section 4.) we quote at this place a particular one which is of relevance for atomic physics. It

concerns the first discovery of spectral lines in Fr. By now the first two doublets in the principal series are completely measured including their fine structure, hfs and IS (Li 80, Be 84, Du 87). Fr attracted the interest of theoreticians because of the simplicity of the spectrum on one hand (only one electron outside closed shells) and because of its highly relativistic character on the other. The ground state hfs field was predicted, e.g. with an accuracy of about 5 % (Dz 83, Ro 84). The experimental check of this prediction required the measurement of the hfs splitting by LIOP (Li 80) as well as of the g_I-factor by ABMR (Ro 84).

Under the typical running conditions at ISOLDE the LIOP experiments produced results down to beams of the order of 10^5 particles/s. Another characteristic number is the total transmission of the apparatus from the atomic beam oven tc the final ion multiplier which detects the signal; it has been determined to be 10^{-5}. The critical signal rate is thus of the order 1/s. For comparison we remark here, that on-line fluorescence detection, as performed in collinear laser spectroscopy experiments, for instance, requires minimal signal rates of 100/s to overcome backgrcund (see section 3.7.). But a better efficiency, i.e. a higher signal rate per incoming atom, compensates for the higher background. Anyhow, the success of LIOP tells us that particle detection in optical experiments is a powerful alternative to photon detection since it solves the background problem.

3.6. Resonance Ionization Spectroscopy (RIS)

Ionization of atoms and molecules by stepwise resonant excitation with two or more laser quanta is a well-established, quite generally applied method in trace analysis (Le 84, Hu 79). The method has earned its first merits in the field of unstable nuclei by an experiment at the Leningrad on-line mass-separator on a series of Eu isotopes $141 \leq A \leq 150$ (Al 83, Fe 84). Fig. 3.18 shows the relevant part of the level scheme. Three photons from three different dye lasers lead from the atomic ground state via two relay states into the continuum. Ionization efficiency is optimized if all three transitions are saturated. This requirement is easily met for the two first steps but poses a problem for the third one, since the cross-section for photoionization into the plane continuum is of the order of 10^{-17} cm^2 only. Therefore, it is advisable to tune this last step to an autoionizing state; in complex spectra plenty of them are met shortly above the ionization limit. From eq. (3.10) one learns that the excitation cross-section for such a state is the higher, the smaller its autoionizing width ($\approx \Gamma_2$) is. The same purpose can be fulfilled by exciting a Rydberg state just below the ionization limit which can easily be field-ionized.

Hfs and IS are measured in the first step. The spectral width of the laser which serves this transition is adjusted to its Doppler width, therefore. Since the latter depends on the collimation of the atomic beam one compromizes between resolution and efficiency again. The two other lasers are run

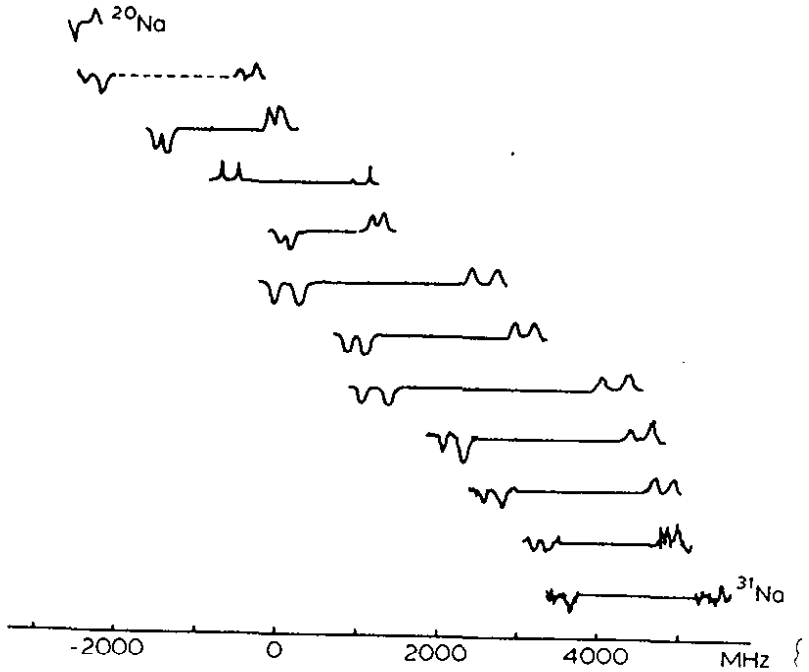

Fig. 3.17: Whole series of Na signals in the D_1-resonance line by LIOP (Hu 78).

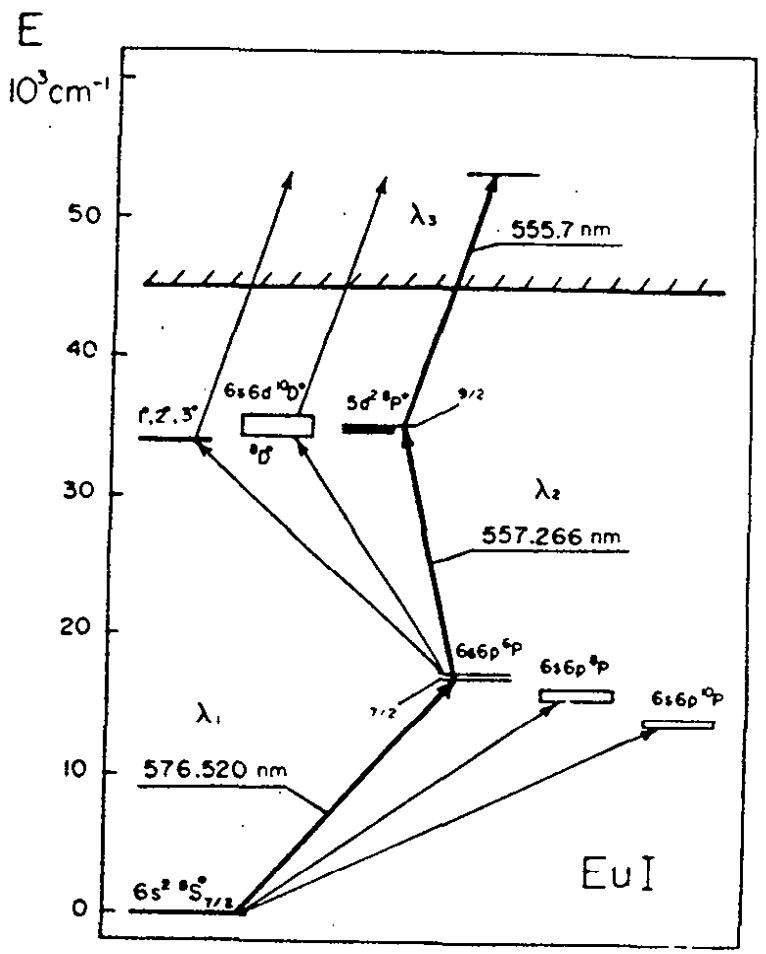

Fig. 3.18: Partial scheme of Eu levels and the transitions used for three-step laser photoionization (Fe 84).

broadband (a few GHz wide) as to match steps 2 and 3 for any of the isotopes without tuning in between.

Fig. 3.19 shows some details of the apparatus used. The ion beam from the mass-separator is stopped in an oven from which it evaporates as atomic beam into the ionization region. The light intensity is amplified by a pair of mirrors providing multipassing of the laser through the atomic beam. The ions are then extracted, focussed onto a channeltron and counted as a function of laser frequency. Fig. 3.20 shows a scan of ^{144}Eu together with reference lines from stable isotopes and fringes from a calibrating interferometer. The nuclear physics interest in this experiment focussed on the very neutron-deficient isotopes around and below the shell closure N = 82 (see section 4.). The group has extended these measurements recently to still lighter Eu isotopes and neighbouring elements (Le 86).

The RIS technique is usually based on pulsed, synchronized lasers with preferably high repetition rate. We quote five principal reasons for this choice:

1. The power, necessary to saturate the intermediate and ionizing transition with broadband irradiation, is only available from pulsed lasers.
2. The pulse width of the order of 10 ns is smaller as or at least comparable with spontaneous decay times into any other atomic state. By running up the ladder very fast one prevents, therefore, that the atoms get lost on the way by OP.
3. The demand for a high pulse rate is self-explaining in view of a high efficiency desired. In the experiment discussed above

Fig. 3.19: Set-up for on-line resonance ionization spectroscopy at the Leningrad mass separator. The inset on the left shows the ionization region blown up (Fe 84).

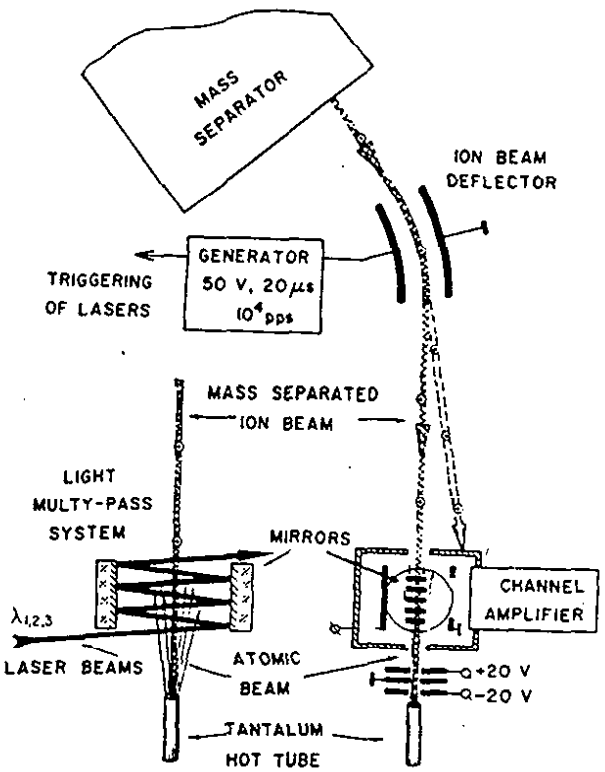

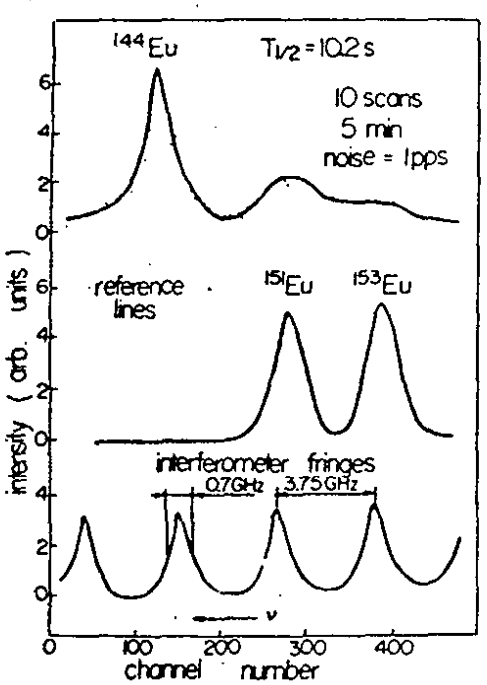

Fig. 3.20: Scan of the ^{144}Eu resonance by the RIS technique together with reference signals from stable isotopes. Bottom: Interferometer fringes for calibrating the laser frequency (Fe 84).

a copper vapour laser was used to pump the dye lasers. Its repetition rate of the order of 10 kHz comes already close to the optimum at which each atom experiences at least one laser pulse during its transit time through the interaction region. An overall efficiency of $3 \cdot 10^{-4}$ was reached in the Eu experiment (Fe 84) which is a very good number in comparison to others.

4. A sharp (delayed) coincidence between the laser pulse and the ion signal allows to cut down the background by the factor of the duty cycle of the laser which was of the order of 10^{-4} in the Eu experiment; this resulted in a noise level of 0.1 count/s (Fe 84).

5. Pulsed operation provides the very important advantage of combining a mass-separation with the RIS technique by a time-of-flight measurement. For this purpose the acceleration voltages and the geometry of acceleration and drift regions of the ions are adjusted to each other such that a time focus is created at the site of the ion detector. In that focus the total time-of-flight is independent (to first or even higher order) from the spatial extension of the ionization region. Fig. 3.21 shows the time-of-flight spectrum obtained in an experiment on neutron-deficient Au isotopes at ISOLDE (Wa 87). The peak of ^{186}Au is clearly separated from the stable ^{197}Au and also from the background of lighter molecular masses. The latter point was very important since the high laser power, necessary for the ionization step in Au, led also to non-resonant multiphoton ionization of rest gas molecules. The Au series is very interesting from the nuclear physics standpoint of view, since it repeats the shape transition observed earlier in light Hg isotopes (see section 4.).

3.7. Collinear Laser Spectroscopy

3.7.1. The Standard Method with Fluorescence Detection

In the optical on-line experiments discussed so far an ion beam has been converted by stopping and reevaporating into thermal atoms forming either a vapour in a cell or a collimated beam. In the former case chemical stability is a restrictive condition, in the latter a large factor is lost by collimation if high resolution is required. The original idea behind collinear laser spectroscopy was simply to avoid these problems by using the mass-separated beam directly as the spectroscopic sample. Since at typical ion velocities of 10^7 cm/s the interaction time with the laser in a crossed geometry would shrink to about 10^{-8} s, a collinear superposition of laser and ion beam seemed favourable. Thereby interaction time and length are easily increased by a factor of 100, when observing fluorescence light from a pathlength of 10 - 20 cm. This can be achieved, e.g. by means of a cylindrical lens which images the beam onto the entrance slit of a light pipe, that adapts the image to the geometry of the photocathode (see Fig. 3.22).

A surprising, crucial advantage of the collinear geometry has been found by Kaufman and published in his proposal (Ka 76) and independently by Wing et al. (Wi 76): The spread of kinetic energy (δE) in the beam remains unchanged under electrostatic acceleration,

$$\delta E = \delta(mv^2/2) = mv\delta v = (mc^2/v^2)\Delta\nu_D\delta\nu_D = \text{const.} \qquad (3.17)$$

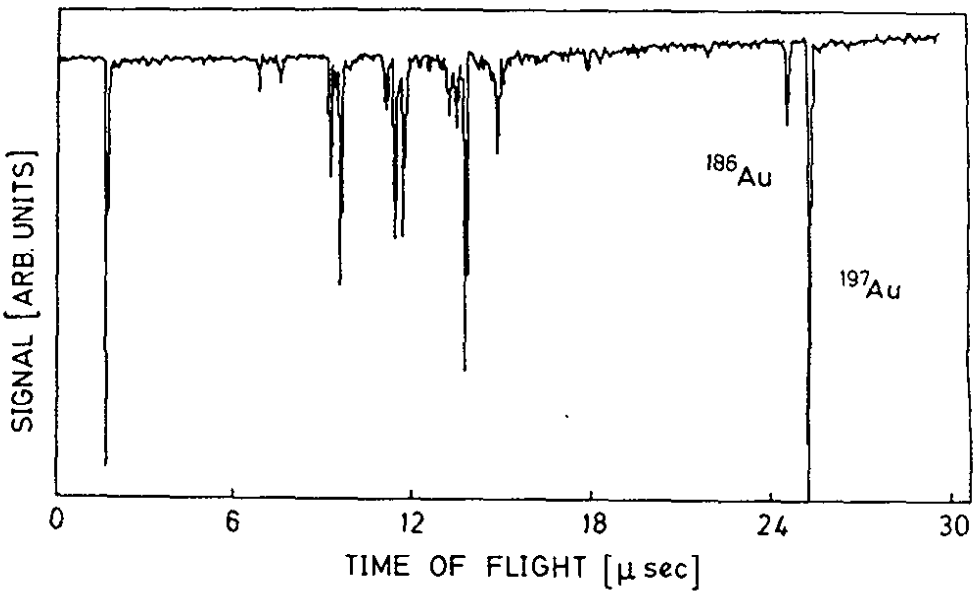

Fig. 3.21: Time-of-flight spectrum obtained in a resonance ionization mass spectrometry experiment (RIMS). ^{186}Au was collected in the atomic beam oven. Stable ^{197}Au was added to serve as a mass marker. The medium-mass ions are due to photoionization of rest gas and can be suppressed by setting an appropriate time window (Wa 87).

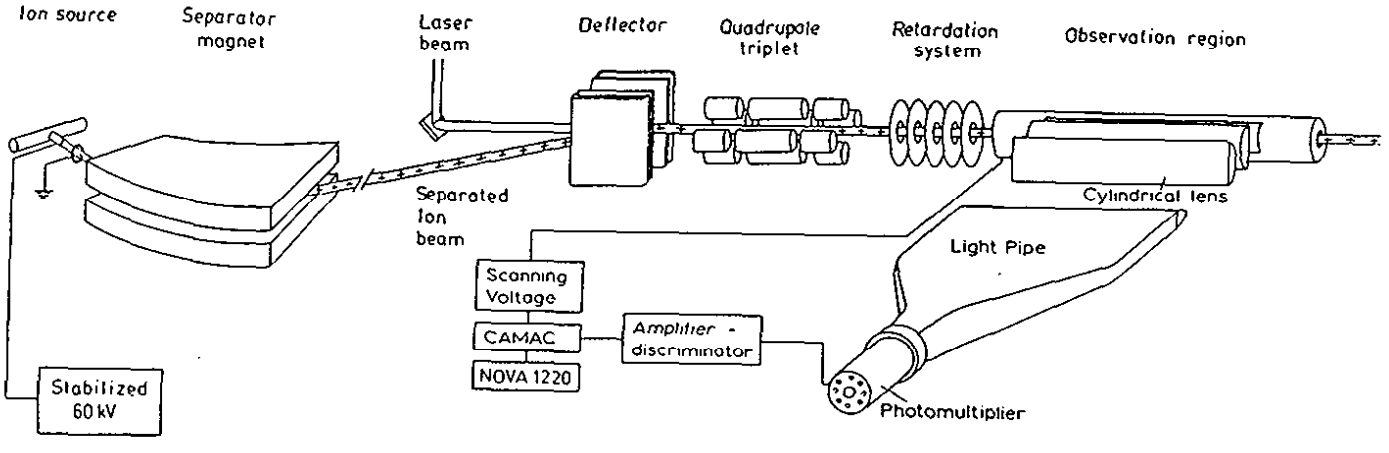

Fig. 3.22: Scheme of a standard collinear laser spectroscopy experiment using fluorescence detection (Mu 83).

Therefore, the product of the average velocity v and the velocity spread δv or likewise the product of the Doppler shift $\Delta\nu_D$ and the Doppler width $\delta\nu_D$ are constants of the motion. In other words: Acceleration reduces the Doppler width along the beam direction by a large factor from its original value in the ion source. Assuming ideal starting conditions, i.e. thermal velocity distribution at the ion source, one observes after acceleration a reduced Doppler width of:

$$\delta\nu_D = 1/2\ (kT/eU)^{1/2}\delta\nu_D(0). \qquad (3.18)$$

The reduction factor is about 10^3 for a source temperature of 2000 K and an acceleration voltage of 60 kV. Under these conditions the residual Doppler width of the green barium resonance line at 535 nm, for example, would be abcut 1 MHz, far below the natural linewidth of 19 MHz. In practice the linewidth ranges from 10 to 50 MHz, depending on the type and performance of the ion source, the stability of the acceleration voltage and the quality of the beam optics. The angular emittances of the laser and ion beams which deterioate collinearity do not contribute significantly to the linewidth, if they do not exceed the order of 1 mRad.

The effect of velocity bunching increases not only the resolution but also the sensitivity: Since the total area under the resonance curve remains unchanged the peak intensity rises by the same factor by which the linewidth narrows.

Another very useful feature of the concept is the charge exchange cell containing an alkali vapour which neutralizes the beam in flight. By that means laser spectroscopy is facilitated decisively since most ions do not have resonance lines in the visible. It is presumed, of course, that the charge exchange process does not disturb the velocity distribution of the beam. This is guarented actually by the large cross-section of about 10^{-15} - 10^{-14} cm^2. Since it exceeds the kinetic cross-section by 2 orders of magnitude most exchange collisions are peripheric. If the charge exchange is non-resonant then the beam energy is changed by (almost) exactly the energy defect ΔE. (The energy transferred in forward scattering to the target atom is only of the order of $(\Delta E)^2/eU$ which is negligible). As seen below charge exchange may also populate a metastable state of the atom which can serve as the lower spectroscopic state from which laser light is absorbed. Collinear laser spectroscopy owes its wide application nowadays to these four aforesaid qualities: (i) good adaptation to mass-separators, (ii) high resolution and (iii) high sensitivity due to velocity bunching, (iv) great versatility due to preparation of suitable spectroscopic states by charge exchange.

Fig. 3.22 shows in some more detail the procedure of measurement for the example of the collinear set-up at the ISOLDE (Mu 83) which was built with the experience of pilot experiments on stable Na (An 78) and on unstable fission isotopes of Rb and Cs (Sc 78, Kl 79). The determination of the atomic transition frequency requires the precise knowledge of the laser frequency, the acceleration voltage and the atomic mass. Instead of measuring

the two former quantities independently, it is safer and easier to run alternatively stable isotopes through the apparatus for calibration. For this purpose the separator magnet is switched periodically from one to the other mass and an appropriate correction voltage is fed to the post acceleration stage just in front of the charge exchange cell. It generates a Doppler shift such that the resonances of the different isotopes coincide in the lab system, that is, for one and the same laser frequency. Scanning of the resonances, finally, is achieved by adding another small voltage stepwise to the charge exchange cell. Thus it is sufficient to run the laser at constant frequency in a stabilized but uncalibrated mode.

Fig. 3.23 shows a set of resonances for three even Ra isotopes recorded in the manner described above (We 85). In Ra the atomic resonance leads from a single, diamagnetic ground state ($7s^2\ ^1S_0$) to an excited $^1P_1$ state from where branching into a metastable $^1D_2$ state is a few percent only. Therefore, the atom emits many fluorescence quanta in the observation region before decaying into the "mute" $^1D_2$ state (compare section 3.3. and Fig. 3.9 explaining the principle). The total detection efficiency of an atom under these conditions has been found to be about 1 %. At typical background levels of 10 kHz on the PM from straylight, surrounding radioactivity etc. measurements were feasible down to currents of about 10^4 atoms/s. The resonances of ^{208,232}Ra shown in Fig. 3.23 were taken under these ultimate conditions.

In complex spectra the sensitivity is cut down by the multiplicity of (metastable) fine structure and hfs levels. The example of the hfs spectrum of ^{151}Dy with $J_1 = 8$ and $J_2 = 9$ and $I = 7/2$

shows, nevertheless, that also such cases can be mastered at an on-line mass-separator of sufficient intensity, although the detection efficiency per separated atom has now dropped to the range of 10^{-4} to 10^{-5} (see Fig. 3.24) (Ne 82).

The high resolution of the collinear method also pays in cases where several isomers are produced and separated simultaneously with the nuclear ground state. Fig. 3.25 shows the example of ^{122}In; 13 out of the 15 hfs components are resolved stemming from spins I = 8, 5, 1 (Eb 87b). This way altogether 37 nuclear states could be investigated in the In chain $104 \leq A \leq 127$.

In a number of cases one can leave out the neutralization by charge exchange considering the fact that ion sources (especially plasma sources) produce ions also in metastable states which display resonance lines in a convenient spectral range. One of the first collinear experiments was conducted this way on a metastable Xe^+-beam (Me 77). The same technique was applied to a series of Eu isotopes at the Leningrad on-line mass separator (Dö 83, Dö 84).

Access to metastable states of noble elements is also provided by charge exchange with an alkali vapor. Consider for instance the case of the noble gas Rn which has a metastable state $(7s\,[3/2]_2)$ bound by - 3.9 eV. This is very close to the ionization potential of a Cs atom in its ground state (see Fig. 3.26). Since charge exchange prefers resonant conditions, the transfer rate into the metastable state is much stronger than into

Fig. 3.23: Lower part: Yield curve of Ra isotopes separated at the ISOLDE facility at CERN. Upper part: Scanning signals from collinear laser spectroscopy of some even Ra isotopes. The integration time is about 30s/channel for ^{208,232}Ra and a fraction of a second per channel for the abundant ^{222}Ra (We 85).

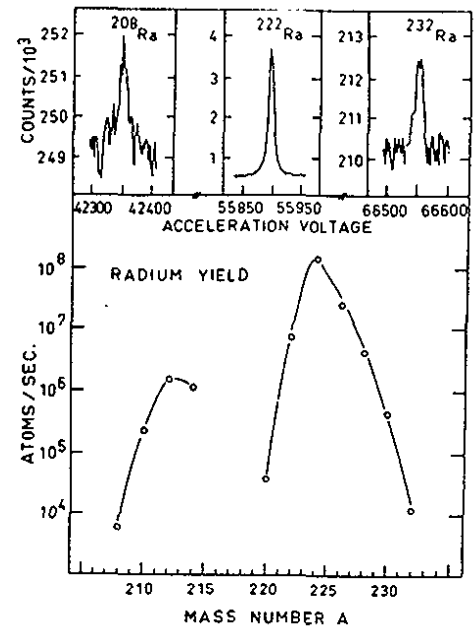

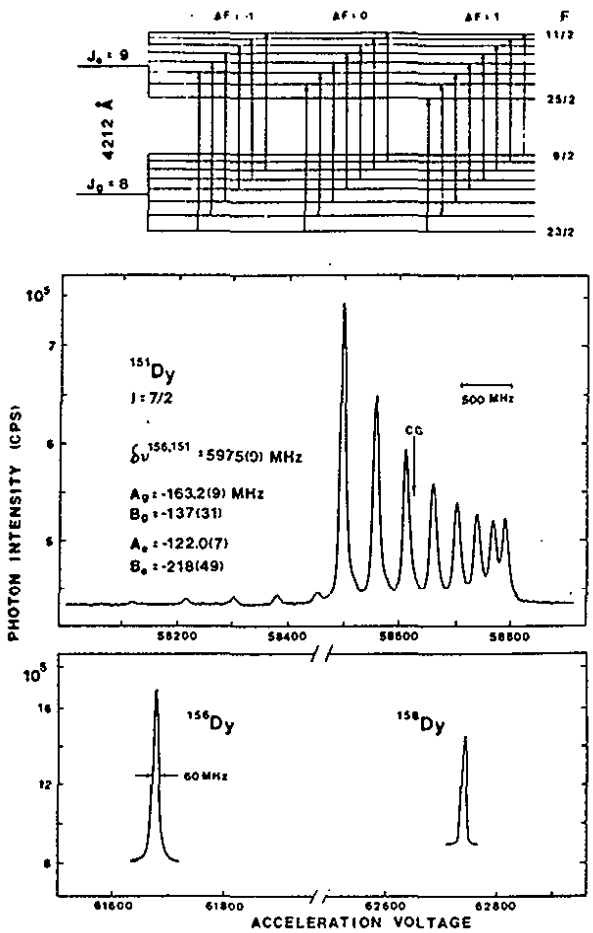

Fig. 3.24: Scan of the hfs of ^{151}Dy by collinear laser spectroscopy. The strong group of resonances belongs to $\Delta F = +1$ transitions, the weak one to $\Delta F = 0$ (compare level scheme on top). $\Delta F = -1$ transitions are too weak to be seen. Bottom: Reference signals from stable Dy isotopes (Ne 82).

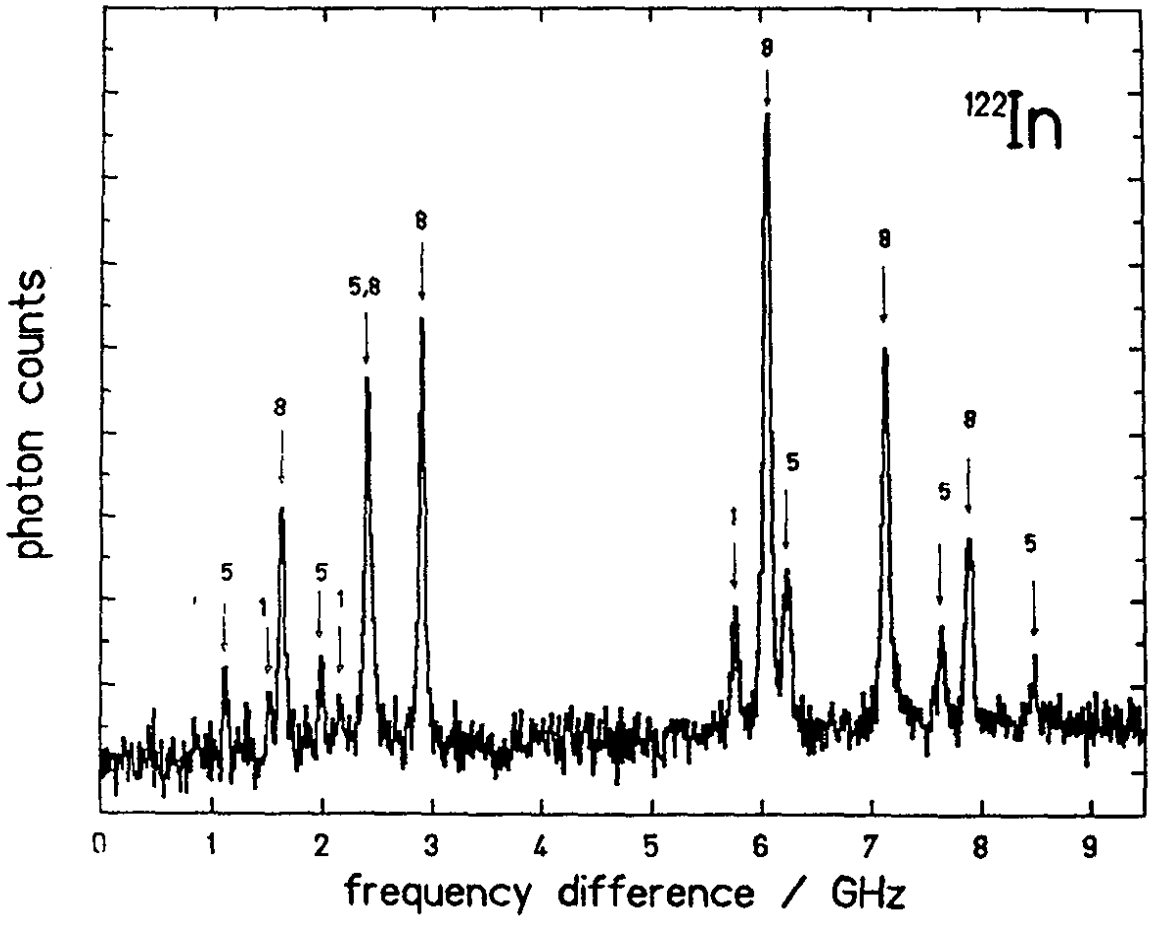

Fig. 3.25: Scan of hfs of ^{122}In in the transition 5p $^2P_{3/2}$ → 6s $^2S_{1/2}$ (λ = 451 nm) obtained by collinear laser spectroscopy (Eb 87b). The hfs components of the nuclear ground state (I = 1) and the two isomers are marked by their spin values. Fluorescence is detected on the other doublet component down to the 5p $^2P_{1/2}$ state (λ = 410 nm). Straylight from the laser can thus be cut off by a colour filter.

the ground state which is bound by 10.7eV. This metastable state is connected by a group of lines in the red spectral range to levels of the $7p6p^5$ configuration which are easily excited by a cw laser. This way spins, moments and charge radii of Rn isotopes could be measured for the first time, ranging from ^{202}Rn to ^{222}Rn (Bo 87). This example proves once more how much charge exchange has enhanced the versatility of the method.

So far collinear laser spectroscopy has been applied to unstable isotopes of the following elements: Li, Rb, Sr, In, Sn, Cs, Ba, Sm, Dy, Eu, Gd, Er, Yb, Hg, Tl, Pb, Rn, Fr, Ra (for references see Table 7.1). Experience tells us that it may be applied to any element for which beams of good ion optical quality and an intensity exceeding 10^4 to 10^7 particles/s are available. The lower number applies to the simplest, the higher to very complex atomic spectra.

3.7.2. Variants of Collinear Laser Spectroscopy

Very far off stability as well as for refractory elements present on-line mass separators cannot provide the intensity required for the standard collinear technique. The separation yields from heavy ion reactions, for instance, which are competitive to spallation very far from stability lie in the critical region of 10^4 to 10^7/s mentioned above. Most of the methodological development in recent years concentrated, therefore, on the increase of sensitivity of on-line optical methods. Three out of the four variants of collinear laser spectroscopy which are discussed in the following aim at that end.

3.7.2a. Fluorescent Atom Coincidence Spectroscopy (FACS).

In the standard scheme the sensitivity is limited primarily by background from laser stray light, radioactivity, PM noise, etc. which add up to typically 10000/s. A group at the Daresbury on-line separator recently succeeded in suppressing this background by tagging true fluorescence photons with the coincidence signal of the incoming beam particle which was detected downstream by a channeltron (see Fig. 3.27a). This way they were able to measure the resonance transition of light Sr isotopes at a beam level as low as 60 particles/s (Ea 86, Ea 87). Fig. 3.27b shows the coincidence count rates for ^{80}Sr and ^{78}Sr as a function of the scanning voltage.

This elegant method requires a very clean beam, of course. Contaminations by other isotopes or isobars will bury the signal in the background from accidental coincidences, especially, since the coincidence window has to be as wide as ≈ 100 ns; because that is the time-of-flight of the particle through the observation region of the PM. In the Daresbury experiment this difficulty was surmounted by carefully conditioning the surface ionization source. The requirement may also be met by a mass separator of high resolution, capable of separating isobars. Another possibility of getting clean beams will be offered by laser ion sources in the near future using the RIS technique. In a pilot experiment on stable Sr a total ionization efficiency of 10 % was recently reached (An 86d). Since these laser ion sources are pulsed they will allow triple coincidence between the times of ion birth (t_0) of fluorescence detection (t_1) and of ion stopping (t_2). The foregoing discussion evidences the great impact which the development

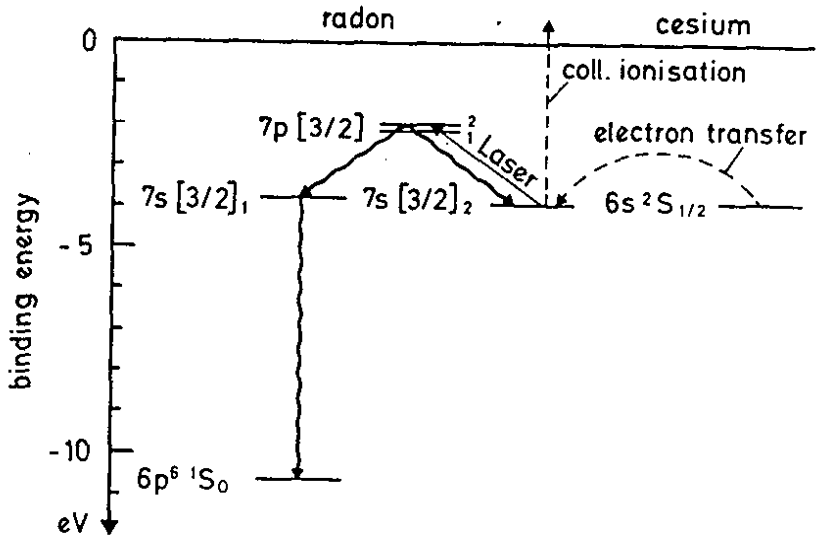

Fig. 3.26: Level diagrams of Rn and Cs. The metastable Rn state at - 3.9 eV is populated by resonant charge exchange with Cs. It is then excited by a laser followed by branched fluorescence decay. Also shown is collisional ionization of the metastable state (compare section 3.7.2.).

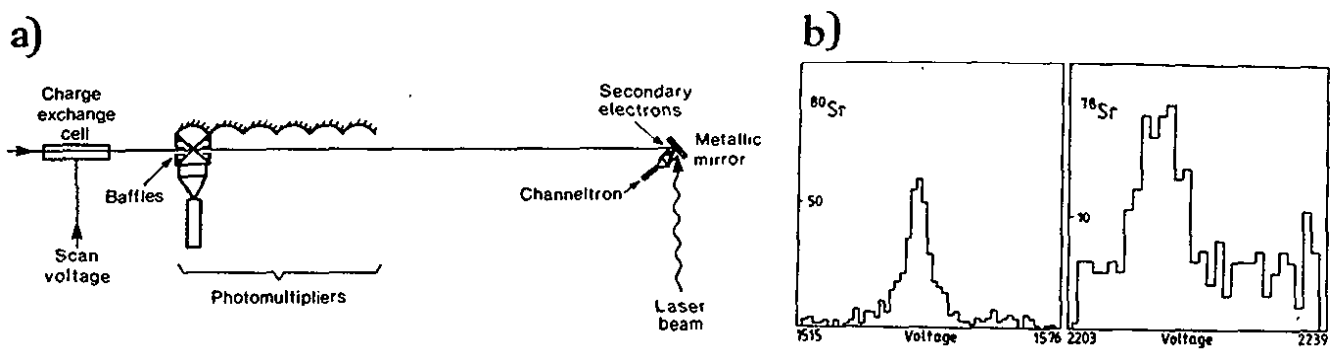

Fig. 3.27: a) Set-up for photon-atom coincidence detection in collinear laser spectroscopy (Ea 86).
b) Number of photon-atom coincidences from a fast beam of Sr atoms as a function of the voltage scanning through the resonance (Ea 87).

of new, sophisticated ion source separator combinations will have on the prcgress of on-line optical spectroscopy in the future.

3.7.2b. Detection by Collisional Ionization and Charge Exchange. As pointed out earlier detection efficiency as well as background rejection may be improved by shifting the signal from photon to particle counting. In the scheme under discussion here, this is achieved by optical pumping into another electronic state of different binding energy. The OP effect is then sensed by the energy dependence of the collisional ionization or charge exchange cross-section. Such a scheme has been developed by Neugart et al. (Ne 86) and is explained in Fig. 3.26 for the case of Rn. The metastable $7s[3/2]_2$ state of Rn is populated by charge exchange with Cs. This state is then excited by a laser to a level of the 7p configuration the decay of which branches into the tightly bound ground state by a cascade. Downstream of the OP region the beam passes another gas filled cell (containing preferentially an electrcnegative gas) in which the remaining metastable fraction of the beam is ionized by collisions (see Fig. 3.28a). The reionized fraction is finally deflected onto a detector giving the signal. The pilot experiment was performed actually on the analogue case of a stable Kr beam for which the reionization signal is shown in Fig. 3.28b in comparison with the standard fluorescence signal. The former which has the character of a flop out signal is a factor of 1000 stronger (Ne 86).

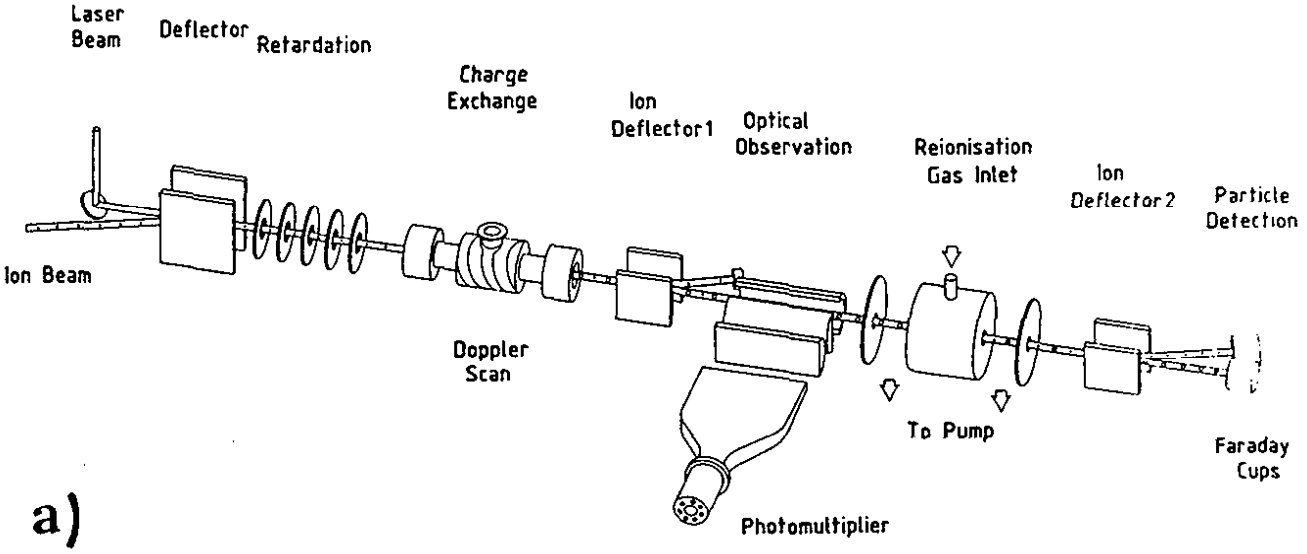

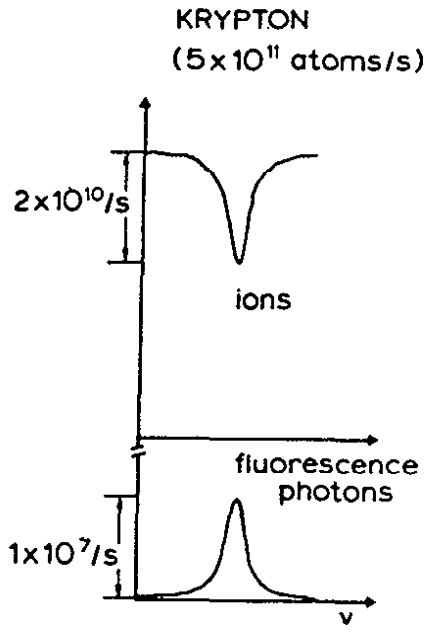

Fig. 3.28: a) Set-up for collisional ionization detection in collinear laser spectroscopy.
b) Resonance signals from a beam of $5 \cdot 10^{11}$ krypton atoms/s; top: reionized fraction of beam; bottom: standard fluorescence signal (Ne 86).

A similar idea was realized independently by Silverans et al. in a reversed sense (Si 85). In his scheme Sr^+ ions were pumped from the 5s ground state via excitation to 6p and subsequent branching into a metastable 4d state (compare the basic level diagramm in Fig. 3.9). The pumping effect was monitored by the difference in neutralization probability of the two ionic states in a subsequent charge exchange cell. This technique was applied recently at the collinear set-up at ISOLDE and enabled to measure ^{100}Sr far out on the wing of the yield curve (Si 86).

3.7.2c. Collinear Laser RADOP. This experiment transfers the ideas of RADOP (section 3.2.) to collinear fast-beam laser spectroscopy (see Fig. 3.29a). A circularly polarized laser polarizes a fast beam of alkali atoms in flight by optical pumping. The beam is stopped in a suitable matrix exposed to an external field B. If relaxation times in this matrix are longer or at least comparable to the nuclear lifetime, the nuclear polarization P_I can be detected by the decay asymmetry measured by a pair of ß-telescopes at 0° and 180° with respect to the field axis. A pilot experiment was conducted on some neutron-rich Rb isotopes at an on-line facility at the Mainz Triga reactor (Bo 85, Sp 85, Ge 86) followed by measurements on short-lived Li isotopes at ISOLDE. Fig. 3.29b shows asymmetry signals of ^{9}Li and ^{11}Li. The signal is small, of the order of 1 % only, although a polarization P_I = 30 % was reached in the beam as could be checked by fluorescence signals from stable ^{7}Li in the same apparatus. The ^{11}Li current was 600 atoms/s. Spin and

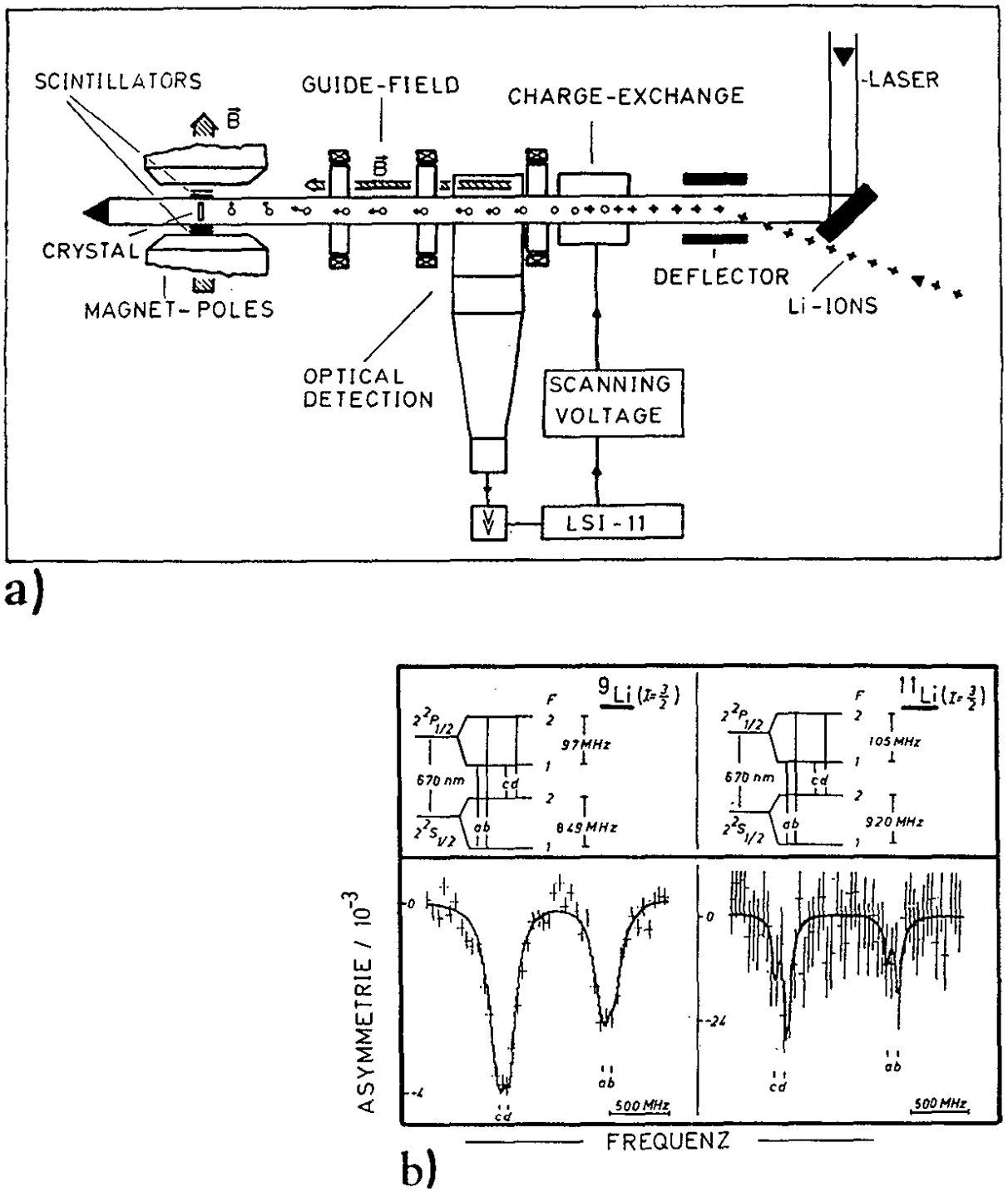

Fig. 3.29: a) Set-up for collinear laser RADOP experiment.
b) ß-asymmetry signals from ^{9}Li and ^{11}Li when scanning the hfs of the D_1-resonance line (bottom); corresponding level schemes (top) (Ar 86).

magnetic moment were determined. The IS, however, is dominated so much by the mass shift that the field shift which would be very interesting to know for such a light nucleus could not be disentangled at the present level of accuracy (Ar 86).

3.7.2d. g_I-Measurement by Spin Rotation. This variant of collinear laser spectroscopy makes also use of spin polarization of a fast beam induced by optical pumping (see Fig. 3.30a). After being neutralized in a charge exchange cell the beam passes the pumping zone I which is followed by a region of length L of a perpendicular magnetic field H_o in which the oriented spins precess by an anlge $\vartheta = \gamma H_o L/v$, where v is the velocity of the beam. Note that H_o is strong enough to decouple the atoms by Zeeman splitting from the interaction with the laser during the precession phase. The precession angle can be measured downstream in the field free zone III by the modulation of the fluorescence intensity as function of H_o; because excitation by a polarized laser beam strongly depends on the angle of orientation of the ground state spin. If the atom in question has a diamagnetic ground state, as in the case of alkaline earths, it is the nuclear spin which precesses and the measurement of ϑ determines directly g_I. The method described was developed by Vialle and collaborators for the examples of Na (Be 84b) and Ba (Ca 86b). The method has then been applied to Ra at the collinear set-up at ISOLDE. It yielded the first direct g_I-measurements for some isotopes of this element, namely ^{213}Ra and ^{225}Ra (Ar 87). Fig. 3.30b shows the precession signal of ^{213}Ra. This measurement also served to calibrate hyperfine

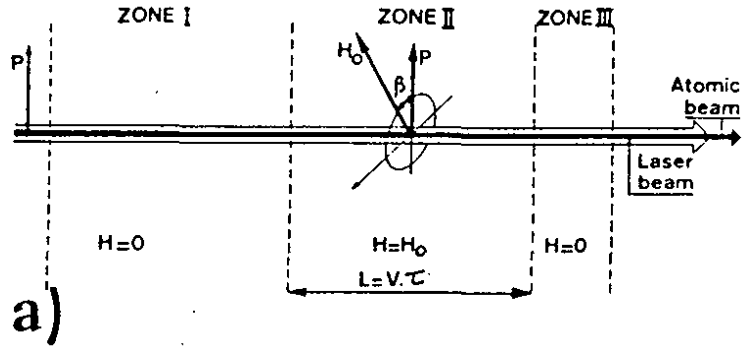

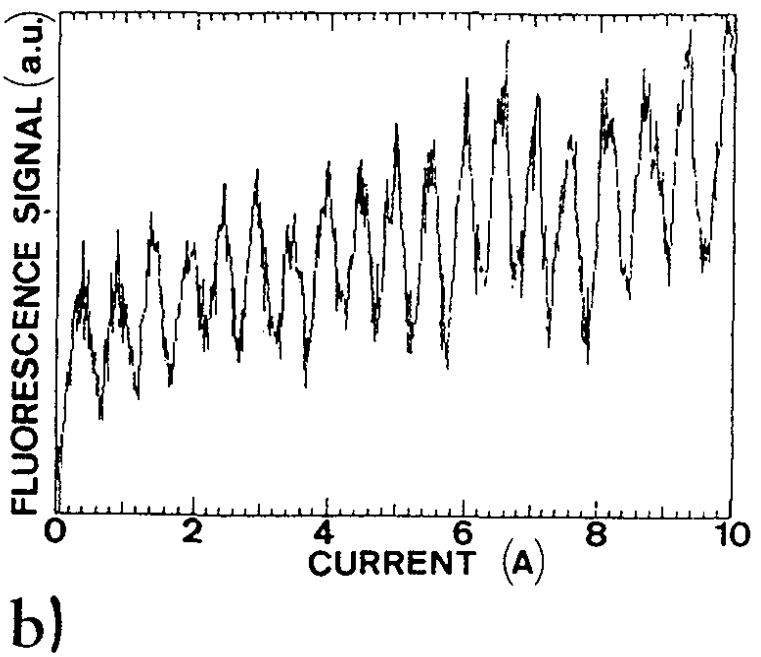

Fig. 3.30: a) Set-up for observation of spin precession in collinear laser spectroscopy (Be 86); I = pumping zone, II = precession zone, III = detection zone. b) Fluorescence intensity of ^{213}Ra observed in zone III as a function of field H_o in zone II (Ar 87).

fields in Ra spectra from measured A-factors (Ah 83) and to compare them to Hartree-Fock calculations for this highly relativistic case. The hyperfine field of the 7s ionic ground state has been determined in this way to be 1226 T in comparison to the following theoretical values: 1293 T (Da 86), 1304 T (He 85), 1266 T (Dz 85). The simple semi-empirical Goudsmit-Fermi-Segrè formula yields 1285 T (We 87).

3.8. Summary of the Experimental Part

In the 20 years of on-line optical spectroscopy the methods have shifted radically from using traditional light sources to the use of tunable lasers. In fact, some of the new techniques, like resonance ionization and collinear laser spectroscopy, are absolutely impossible without lasers. Most of the methods discussed have yielded abundant results; Table 7.1 lists about 400 nuclei whose spins, moments or charge radii have been determined by these experiments. But we should also emphasize the importance and the elegance of some side stream developments, variants of the main methods, which are dedicated to the solution of a certain special problem.

At present methodological work is progressing very efficiently towards higher sensitivity, pushing the exploration of nuclear structure by optical means further off stability and to refractory elements. In parallel, new schemes of ion source and separation techniques are being installed which enrich the scope of separable elements and correspond better to

the demands of on-line optical methods, regarding isobaric purity, beam quality, beam pulsing, etc. It is foreseeable that also laser spectroscopy of ions, stored in traps, will soon have a chance in on-line experiments. In view of the many vigorous activities one may expect that the knowledge of spins, moments and charge radii of nuclear ground states will be essentially completed in the next decade.

4. DISCUSSION OF NUCLEAR MOMENTS AND RADII IN EXTENDED CHAINS OF ISOTOPES

As has been mentioned already the results of optical investigations off stability, described in the preceding section, cover around 400 nuclear states. They are collected in Table 7.1 which lists spins, moments and $\delta\langle r^2\rangle$ values. It cannot be the object of this discussion to discuss this vast amount of new material nucleus by nucleus. Instead, we will try to work up this field (i) by putting spotlights on exemplaric and particularly interesting cases and (ii) by analyzing systematic features of nuclear structure which are shown up in the data. The latter aim envisages in particular nuclear radii and shapes, whereas the single particle structure, displayed by spins and magnetic moments, is treated only briefly and oaccasionally.

4.1. Spins and Moments

4.1.1. Interpretation in Terms of the Particle Plus Rotor Model

The quantitative interpretation of spins and moments requires for each case not only the knowledge of the gross and collective structure but also a detailed analysis of the single-particle character of the particular nuclear state in question which implies a large effort. In fact, the published literature on systematic calculations of moments far off stability is sparse. Ekström's review article covers the material up to 1980 (Ek 81). As mentioned already he calculates magnetic and

quadrupole moments by the particle plus rotor model (La 78) based on the Nilsson model. With respect to magnetic moments the model works the better, quite naturally, the clearer the state in question can be identified with an asymptotic Nilsson state in a well deformed nucleus. In the region of intermediate coupling which applies to moderately deformed nuclei the model calculates the wave function of an odd nucleus as superposition of individual single-particle Nilsson states. In this region the model still produces qualitatively correct results concerning magnitude and trends of magnetic moments, although its predictions of level ordering and of indentifying the ground state tend to be less reliable there. The model may be extrapolated to spherical nuclei as long as their states correspond to single-particle shell model configurations and not to complex ones. Core polarization and mesonic effects on μ_I are taken into account schematically by introducing fixed, effective nucleon g-factors.

4.1.2. Trends of Magnetic Moments near Shell Closures

The kind of systematics obtained nowadays is demonstrated in Fig. 4.1 by a few selected chains of magnetic moments; they were not jet, or only partly known at the time of Ekström's review (Ek 81). The Li, Eu and Tl moments in Fig. 4.1a concern sequences of constant spin which should represent always the same dominant single-particle proton state (or hole) just above (or below) a closed proton shell. The moments always peak at the neutron shell closure where 100 % of the Schmidt value is

reached in case of ^{11}Li, 80 % for ^{145}Eu and 70 % for ^{207}Tl. The corresponding states are $1p_{3/2}$, $2d_{5/2}$ and $3s_{1/2}$, respectively.

The moments of direct neighbours of double magic nuclei have always attracted much theoretical interest. For the case of ^{207}Tl Neugart et al. (Ne 85b) have discussed the various theoretical results in comparison to their experimental value. The increase of the moment at the magic number is explained by two effects: (i) first-order core polarization from the $\nu(p_{3/2}^{-1} \otimes p_{1/2})\ 1^+$ particle hole excitation vanishes because of the closed neutron shell. (ii) Admixture of collective excitations like $(2^+ \otimes d_{3/2}^{-1})\ 1/2^+$ are suppressed by the sharp rise of the excitation energy at the magic number. The closest theoretical results lie about 3 % off the experimental value (Hy 80, Ba 73).

4.1.3. Checking the Odd Group Coupling Rule

Fig. 4.1b shows the series of odd-odd magnetic moments in In (Eb 87b). Since the moments of most of the relevant states in neighbouring isotopes and isotones (in Cd and Sn) are known as well, this total set of data offers an excellent chance for checking systematically the odd group coupling model. It predicts $\mu_{I,odd,odd}$ to be the vector sum of the moments of the odd proton group (p) in the adjacent odd-even nucleus and of the odd neutron group (n) in the adjacent even-odd nucleus, provided the configurations are the same. The relation reads

$$\mu_{I,odd,odd} = \frac{I}{2}\left[g_p+g_n+(g_p-g_n)\,\frac{I_p(I_p+1)-I_n(I_n+1)}{I(I+1)}\right]. \qquad (4.1)$$

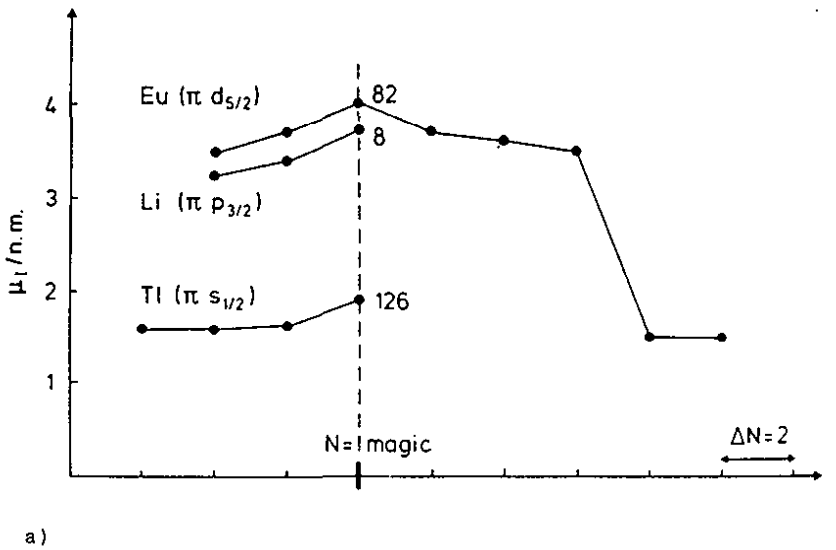

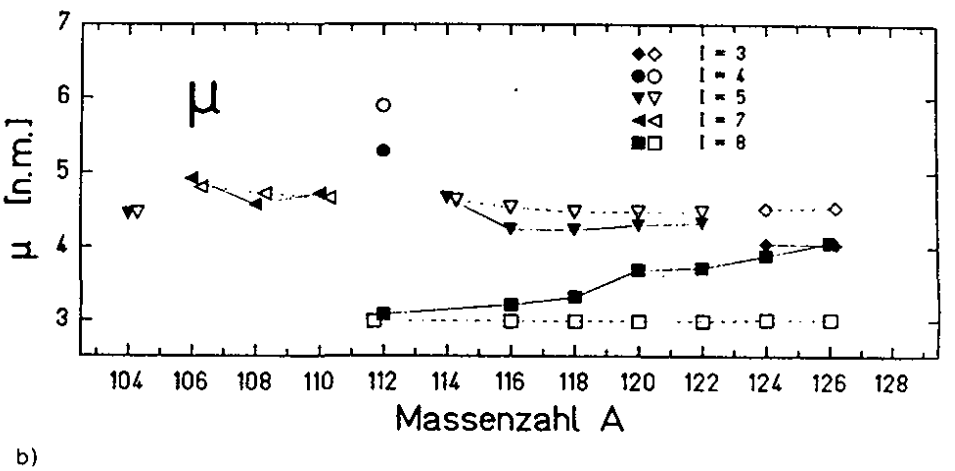

Fig. 4.1: a) Isotopic sequences of magnetic moments of some single particle proton states near shell closures. Numbers indicate neutron numbers. The ($\pi 3s_{1/2}$) moments in Tl are known down to N = 114 and remain at a constant value of = 1.6 nm (data and references given in Table 7.1).

b) μ_I-values of odd-odd In-isotopes (Eb 87b). Equal spins are connected by lines. Full symbols represent experimental, open ones semi-empirical values.

These semi-empirical moments are plotted together with the experimental ones in Fig. 4.1b (Eb 87b). The configurations involved are $(\pi g_{9/2})^{-1} \otimes (\nu d_{5/2})$, $(\nu g_{7/2})$, $(\nu s_{1/2})$, $(\nu d_{3/2})$, $(\nu h_{11/2})$. For I < 8 the agreement varies from fair (I = 3) to very good (I = 5). For the discrepancy at I = 8 see below.

The odd group coupling model may be applied as well to spectroscopic quadrupole moments as to magnetic ones, although the quadrupole case is hardly discussed in the literature. The odd group moments $Q_{s,p}$ and $Q_{s,n}$ are added with tensor coupling coefficients q_1, q_2, defined in ref. (Bo 69), to the resulting moment

$$Q_{s,odd,odd} = q_1 Q_{s,p} + q_2 Q_{s,n}. \qquad (4.2)$$

The perfect agreement of these semi-empirical moments with the measured ones shown in Fig. 4.2 is a great surprise, indeed (Eb 87b).

4.1.4. Quadrupole Moments of Decoupled States

The Q_s-values of the I = 8 states form an exception from the odd group coupling rule again. The experimental moments rise much faster than the semi-empirical ones. In both cases the experimental odd neutron group moments had to be taken from Sn isotones since they are not available in Cd (except for N=67). The discrepancy might be connected, therefore, to the strong, polarizing power of the $\nu(h^n_{11/2})$ group which affects the In

core more than the proton magic Sn core. A change in nuclear structure would invalidate the odd group coupling model, of course.

Another very interesting phenomenon in Fig. 4.2 is the steady increase of Q_s from 0 to 0.6 barn in the I = 8 series. It can hardly be ascribed to a corresponding change in deformation since Q_s remains pretty constant for other spin values. An explanation can be found if one assumes, that the high spin states decouple from the core (Eb 87b).

The interpretation of spectroscopic quadrupole moments of intermediate nuclei in terms of decoupled states and its quantitative proof by calculations with the particle plus rotor model has thrown light into this hitherto very dark problem (Vo 77, Da 79, Ra 80, Fa 81, Ek 81). Let Ω be the projection of the spin on the intrinsic nuclear symmetry axis, then Q_s varies with Ω like

$$Q_s = \frac{3\Omega^2 - I(I+1)}{(I+1)\ (2I+3)}\ Q_o \qquad (4.3)$$

where Q_o is the intrinsic quadrupole moment. At moderate deformation a single nucleon in a high j-shell decouples from the intrinsic axis and orients itself such that the wave function has maximum overlap with the core. For oblate shape ($Q_o < 0$) this is achieved at $\Omega = j = I$, for prolate one ($Q_o > 0$) at $\Omega = 1/2$. In both cases Q_s will be negative according to eq. (4.3). With Ω-levels getting filled, Q_s will increase, pass

zero in the middle of the shell and will reach its maximum positive value finally for the single hole state*). Q_s values of $i_{13/2}$-isomers of Hg were first interpreted this way; they represent a favourable example since the intrinsic deformation of this series of nuclei is known to be rather constant. Fig. 4.3 shows the results of the first quantitative theoretical treatment of this problem in the frame of the particle plus rotor model by Ragnarsson. An equilibrium deformation of $\varepsilon = -0.125$ was chosen throughout the series (Ra 80). The agreement with experiment is quite satisfactory.

Ekström has extended these calculations systematically to other regions of nuclei and could interpret many other Q_s values of intermediate nuclei in this manner (Ek 81). The course of the 8^+-In moments in Fig. 4.2 perfectly resembles the one of Hg moments; therefore the same cause is advocated, namely, filling up a shell of decoupled high spin states.

The general discussion of nuclear moments shall be finished with these examples; but it will be resumed at certain particular points of interest in the following discussion of nuclear radii and shapes where spins and moments helped to identify collective structure.

4.2. Decomposition of ms Charge Radii into Volume and Shape Effect

Since the field effect of the isotope shift measures the change of the mean-squared charge distribution one expects it

*) We have to remind that in case of a $(j)^n$ shell model configuration Q_s shows the same qualitative behaviour as function of n as ascribed to decoupled states above. A decision between both interpretations has to be taken on quantitative grounds and with the input of additional spectroscopic information.

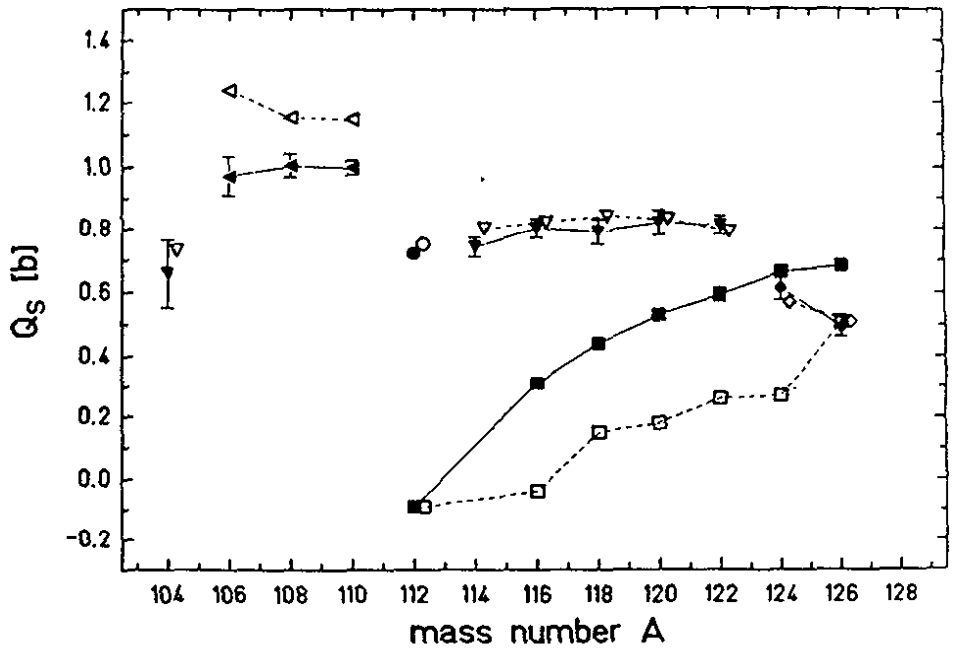

Fig. 4.2: Experimental and semi-empirical Q_s values of odd-odd In isotopes. Symbols defined as in Fig. 4.1b (Eb 87b).

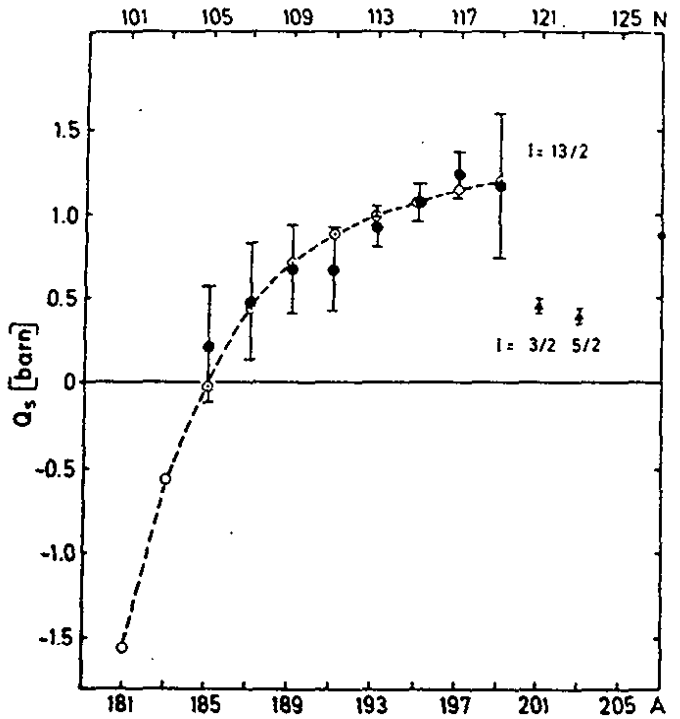

Fig. 4.3: Q_s of $i_{13/2}$ isomers of Hg isotopes; full symbols: experiment (Ul 86); open symbols: particle plus rotor calculation (Ra 80).

to be governed by nuclear gross properties rather than by fine details of the single-particle structure. According to any nuclear model with saturated short range binding, the nuclear volume should increase proportional to the mass number and hence $\langle r^2 \rangle$ in proportion to $A^{2/3}$ (eq. (2.12)). From a brief look to some plots of isotope shifts in sections 4.5.ff below one learns, on the other hand, that $\delta\langle r^2 \rangle$ is not a smooth function of A. Obviously it cannot be explained by a liquid drop estimate of the change of nuclear volume alone, but one has to consider the influence of nuclear shape in addition; the latter has a strong and sometimes even abrupt A-dependence as a consequence of shell structure. The interpretation of isotope shifts will be started therefore by discussing some general relations between nuclear volume and shape, and $\delta\langle r^2 \rangle$. This field has been reviewed by Barret (Ba 74) and by Brix (Br 77).

4.2.1. Models of Charge Distribution for Spherical Nuclei

The assumption of a uniformly charged, spherical liquid drop (eq. (2.10) and eq. (2.12)) leads to the so-called standard or uniform shift

$$\delta\langle r^2 \rangle^{A-A'}_{unif} = 2/5\ r_o^2\ A^{-1/3}\ (A-A'). \qquad (4.4)$$

A choice of r_o = 1.2 fm was supported by early electron scattering experiments which analyzed the formfactor in terms of the two parameter Fermi distribution

$$\rho(r) = \rho(0)\ /\{1 + \exp\ (4\ \ln 3\ \frac{r-c}{t})\}. \qquad (4.5)$$

The two parameters are the skin thickness t and the half density radius c. In this model $\langle r^2 \rangle$ is given to very good approximation by (En 74)

$$\langle r^2 \rangle = 3/5\ c^2\ [1 + \frac{7}{3}\ \frac{\pi}{4 \ln (3c/t)}]. \qquad (4.6)$$

More recent results including those from muonic spectra have shown that nuclear expansion along the stable valley is somewhat weaker than $A^{1/3}$; instead the parametrization

$$c = (1.146\ A^{1/3} - 0.784\ A^{-1/3} + 0.122\ A^{-5/3})\ \text{fm}$$
$$t = 2.3\ \text{fm} \qquad (4.7)$$

fits the data better (En 74). Eq. (4.7) implies a reduction of the standard shift (4.4) by about 10 % for the heaviest nuclei.

For the isotope shift, however, neither of these formulae apply; in the average it is a factor of two smaller than the standard shift. This deficit of the isotope shift has to be compensated by a correspondingly larger isotone shift, in order to recover the validity of the $A^{1/3}$ law or, more precisely, of eq. (4.7) along the stable valley.

These facts tell immediately that protons and neutrons cannot be equally distributed over the nucleus such that the ratio of their densities would be Z/N everywhere. A more realistic substitute for the uniform model was found in the spherical

droplet model by Myers et al. (My 69, My 77, My 83); it turned out to be a very satisfactory gross model not only for the interpretation of nuclear masses but also of the average isotope shift, i.e. for its volume dependent part, measured at constant nuclear shape. This success is mainly due to an additional degree of freedom of this model: proton and neutron distributions are allowed to vary from each other in order to balance isospin dependent forces (Coulomb and symmetry force) against isospin independent ones. Therefore, the model discriminates inherently between isotope and isotone shift. Its predictions for isotone and isobar shifts will be discussed in section 4.10.

In the following $\langle r^2 \rangle_s$ and $\delta\langle r^2 \rangle_s$ define the ms radius and its change for any spherical charge distribution; $\delta\langle r^2 \rangle_s$ will be called the volume contribution to $\delta\langle r^2 \rangle$. $\langle r^2 \rangle_{sD}$ and $\delta\langle r^2 \rangle_{sD}$ are the corresponding values calculated from the spherical droplet model with parameters as given in ref. (My 83).

4.2.2. The Shape Effect on the ms Radius

The surface of an axially symmetric, deformed and uniformly charged nucleus may be obtained from a spherical one by the transformation (for the following we refer to ref. (My 83))

$$R_d = R_o \, n \, (1 + \sum_i \beta_i \, Y_{io}(\vartheta)). \qquad (4.8)$$

The parameters β are a measure of the multipole deformations of order i. The normalization factor n is a function of the β_i and ensures volume conservation. The lowest order contribution of β_i to $\langle r^2 \rangle$ is given by

$$\langle r^2 \rangle_d = \langle r^2 \rangle_s \left[1 + \frac{5}{4\pi} \sum_i \langle \beta_i^2 \rangle\right] \qquad (4.9)$$

and hence to first-order

$$\delta\langle r^2\rangle_d = \delta\langle r^2\rangle_s + \langle r^2\rangle_s \frac{5}{4\pi} \sum_i \delta\langle \beta_i^2\rangle \qquad (4.10)$$

with $\langle r^2\rangle_s = 3/5\ R_o^2$. Literature uses for R_o either the droplet value or the simple liquid drop value $1.2\ A^{1/3}$ fm. The difference is tolerable in evaluating $\delta\langle\beta^2\rangle$ from eq. (4.10). With eq. (4.9) and eq. (4.10) we have found the separation of $\delta\langle r^2\rangle$ into volume and shape effect, sought for. Myers and Schmidt (My 83) have also given higher-order corrections to eq. (4.9) from which we quote the contribution of third-order in the quadrupole deformation. It equals to

$$\langle r^2\rangle_s \frac{10}{21} \left(\frac{5}{4\pi}\right)^{3/2} \langle\beta_2^3\rangle \qquad (4.11)$$

and discriminates between prolate and oblate shape. The term (4.11) may be generalized to include triaxial shape, characterized by the parameters β and γ (defined e.g. in ref. (Ei 70)); it then reads (Gr 60) (corrected for a numerical factor of 5)

$$\langle r^2\rangle_s \frac{3}{8\pi} \beta^3 \cos\gamma\,[1 - 4\sin^2\gamma] \qquad (4.12)$$

For a nucleus with $\gamma = 30°$ which is neither prolate nor oblate the third-order term vanishes. At $\beta = 0.3$, $\gamma = 0°$ or $60°$ it contributes $\pm$ 9 % to the total shape effect, but is neglected in most analyses, nevertheless. This procedure is consistent in so far as in the evaluation of deformation parameters from other collective observables, like BE2 or Q_s values, higher-order corrections are neglected as well in the common literature.

One should keep in mind, however, that this procedure is not quite satisfactory at large deformation, although the validity of the model is subjected to certain limits of accuracy by itself.

In droplet model calculations one considers a redistribution of the nucleon densities from its primary droplet ansatz which allows residual forces to relax towards maximum binding energy. The effect of redistribution on $\langle r^2 \rangle$ is calculated for spherical as well as for deformed nuclei. In analyses of isotope shifts by eq. (4.10) one only takes into account the spherical redistribution, since the deformation is not known a priori but should be extracted from the IS. This deficiency could be avoided in principal by iteration, but it is not significant in comparison to other short-comings of the analysis.

All deformation parameters contribute with equal weight to eq. (4.9) and eq. (4.10) and always by their mean-squared value. Therefore, the IS measures not only the static deformation $\langle \beta \rangle$, as Q_s does, but in addition its zero point fluctuation $\langle (\langle \beta \rangle - \beta)^2 \rangle$. This point plays a fundamental role in the discussion of results.

A typical deformation of $\beta_2 = 0.3$ causes an increase in $\langle r^2 \rangle$ by about 4 % (according to eq. (4.9)). At first sight this seems to be a small effect. But it is very large, in fact, as compared to the volume effect caused by the addition of one neutron. The latter is of order

$$\delta \langle r^2 \rangle_s^{N,N-1} \; / \; \langle r^2 \rangle_s \approx 1 \; / \; 3A \qquad (4.13)$$

which is 0.3 % at mass A = 100. The example illustrates how sensitive the isotope shifts react on a change in nuclear shape.

4.2.3. Influence of Surface Diffuseness

Eq. (4.9) and eq. (4.10) were derived under the assumption of a sharp nuclear surface. They remain valid, in fact, if instead of the awkward Fermi function, the Helm model (He 56) is used to create diffuseness of the nuclear surface. It consists in folding a sharp-edged distribution with a Gaussian

$$G(r) = (2\pi\sigma)^{-3/2} \cdot e^{r^2/2\sigma^2} \qquad (4.14)$$

of width σ. It has the following mathematical advantages (My 83): (i) All multipole moments of $\rho(r)$, i.e. the total charge, the quadrupole moment, etc., are independent of σ and hence the same as for the original, sharp-edged distribution; (ii) the deformation part of $\delta\langle r^2\rangle$ remains unchanged as said above. (iii) The increase of the total $\langle r^2\rangle$ due to diffuseness is given by the very simple formula:

$$\Delta\langle r^2\rangle_\sigma = 3\sigma^2. \qquad (4.15)$$

The Helm model is certainly as good an approximation for the surface diffuseness as the Fermi function. Friedrich and Voegler were able to fit form factors from electron scattering data quite well by droplet charge distributions folded with a Gaussian of width σ = 0.99 fm (Fr 82, Fr 81b).

4.3. The Two-Parameter Model of $\delta\langle r^2\rangle$ and its Relation to other Collective Observables

In many cases the shape effect on $\langle r^2\rangle$ will be dominated by the quadrupole mode (β_2) and others are negligible. With this simplification eq. (4.9) and eq. (4.10) are known as the two parameter model. The change in deformation $\delta\langle\beta_2^2\rangle$ may then be extracted from experimental $\delta\langle r^2\rangle$ values with the help of a model assumption for $\delta\langle r^2\rangle_s$ (e.g. the droplet model) or vice versa.

For very heavy elements the simple decomposition into volume and shape effect is being complicated by the Seltzer expansion (2.14). The higher radial moments react stronger on a change of shape than of volume. But since their contributions are small one may expand them in terms of $\delta\langle r^2\rangle_s$ and $\delta\langle\beta_2^2\rangle$ to obtain

$$\lambda = (1+x)\,\delta\langle r^2\rangle_s + (1+y)\,\frac{5}{4\pi}\,\langle r^2\rangle_s\,\delta\langle\beta_2^2\rangle \qquad (4.16)$$

which is now the two parameter model for λ. The correction factors

$$x = \frac{10}{7}\,\frac{G}{F}\,R_o^2 + \frac{5}{3}\,\frac{H}{F}\,R_o^4 \qquad (4.17)$$

$$y = 2\,\frac{G}{F}\,R_o^2 + 3\,\frac{H}{F}\,R_o^4 \qquad (4.18)$$

are of order 10 % for the heaviest nuclei (Ah 85). Eq. (4.16) can also be used to convert the experimental λ into $\delta\langle r^2\rangle$ values,

where model dependence enters only with the small weights of x and y. Table 7.1 lists $\delta\langle r^2\rangle$ instead of λ since the former is more convenient for comparison with theory.

4.3.1. Relation to the Geometrical Model

It is interesting, of course, to relate $\langle\beta_2^2\rangle_{IS}$ or $\delta\langle\beta_2^2\rangle_{IS}$ values, extracted from the isotope shift, to other collective observables. A stringent relation to quadrupole transition strengths can be derived from the closure rule of quantum mechanics yielding

$$\langle\beta_2^2\rangle = \left(\frac{4}{3ZR_o^2}\right)^2 \sum_i B(E2, 0^+ \rightarrow 2_i^+). \qquad (4.19)$$

Eq. (4.19) should be model-independent except for the basic assumptions about size and shape of the geometrical model of the nucleus. The sum is exhausted by its first term, already, in two limits of collective motion: (i) harmonic vibrator and (ii) rigid rotor (Ku 72). Since in the latter case $\langle\beta_2^2\rangle = \langle\beta_2\rangle^2$, one may introduce the concept of the intrinsic quadrupole moment, related to $\langle\beta_2\rangle$ by

$$Q_o = 3\,Z\,R_o^2\,\langle\beta_2\rangle/\sqrt{5\pi}. \qquad (4.20)$$

In the limit of a well-deformed rigid rotor also the strong coupling rule $\Omega = I$ is expected to be valid. Hence one can project Q_o onto Q_s via eq. (2.26) and finally relate the shape effect of the IS to the spectroscopic quadrupole moment Q_s.

4.3.2. Relation to the Interacting Boson Model

An expression similar to the two parameter model (4.9, 4.10) is also derived from the interacting boson model (IBA). The ms radius is given there by that of the closed shell nucleus $\langle r^2 \rangle^{cs}$ plus four more terms which are proportional to the number of pairs of valence protons N_π, of valence neutrons N_ν, of proton bosons $\langle n_{d\pi} \rangle$ and of neutron bosons $\langle n_{d\nu} \rangle$ (Ia 81):

$$\langle r^2 \rangle = \langle r^2 \rangle^{cs} + \gamma_{\pi\pi} N_\pi + \gamma_{\pi\nu} N_\nu + \beta_{\pi\pi} \langle n_{d\pi} \rangle + \beta_{\pi\nu} \langle n_{d\nu} \rangle \quad (4.21)$$

The fore factors γ, β are free parameters of the model. The first and the second term describe the isotone and isotope shift, respectively, for a spherical nucleus. Since the expectation value of d bosons, $\langle n_d \rangle$, is proportional to $\langle \beta_2^2 \rangle$ eq. (4.21) is equivalent to the two parameter model (4.9), except that the deformation part is splitted up into separate contributions of proton and neutron d-bosons; the latter is usually neglected. As far as $\delta\langle r^2 \rangle$ values are to be compared to BE2 values only, the IBA equation is short-circuited by eq. (4.9) already and yields no additional information. It becomes useful as soon as $\delta\langle r^2 \rangle$ values are included and discussed within the frame of a general fit of IBA parameters from spectroscopic data. Some analyses in regions around N = 82 have been published (Ia 83).

Alonso et al. (Al 85) extended the model to odd nuclei and applied it to neutron-deficient Cs and Xe isotopes. Focus-

sing on differential isotope shifts $\delta\langle r^2\rangle^{N,N-2}$ and $\delta\langle r^2\rangle^{N,N-1}$ they could reproduce the odd-even staggering in Xe and in particular the isotope shift of intruder states in Cs (see also sections 4.5.2. and 4.11.).

4.4. Effects of Nuclear Core Polarization on the Optical Isotope Shift

It is well known that muonic spectra are seriously affected by the so-called dynamical muon-nucleus interaction which describes nuclear excitation by the muon. At first sight it seems to be very unlikely that the much weaker matrix elements of the electronic interaction could cause any measurable second-order effect of that kind. However, in comparison to the atomic IS which is a tiny effect itself, the effect of nuclear polarization is not completely negligible as has been pointed out by Reiner and Wilets (Re 62). Their results have recently been confirmed and extended by Hoffmann et al. (Ho 84) in a more general second-order perturbation treatment of the problem using quantitative models for the nuclear polarizability. They show explicitely that the interaction strength is centered far out in the electron continuum at energies of 20 - 100 MeV, contrary to dynamical muon-nucleus interaction which is strongest among neighbouring fine structure levels.

The high electron excitation energy has three consequences: (i) The nuclear excitation energy may be neglected against the electronic one in the denominator of the perturbation energy

which may be written formally as a multipole expansion

$$\Delta E = - \sum_{i,j\neq 0,k=0}^{\infty} \frac{|\langle \psi_i^{(e)}\psi_j^{(n)}|\, F_k^{(e)} \otimes M_k^{(n)} |\psi_o^{(e)}\psi_o^{(n)}\rangle|^2}{E_i^{(e)} + E_j^{(n)} - E_o^{(e)} - E_o^{(n)}} \qquad (4.22)$$

(The $F_k^{(e)}$, $M_k^{(n)}$ are operators of the electronic multipole fields and nuclear multipole moments, respectively.) With the neglection of $E_j^{(n)} - E_o^{(n)}$ one can approximate the sum over nuclear matrix elements by $\langle (M_k^{(n)})^2 \rangle$ via the closure relation, that is by the ms zero point amplitude of the mode k like in eq. (4.19).

(ii) The de Broglie wavelength of the admixed electronic states is of the order of nuclear dimensions. Therefore, the electronic wave funtion is reshaped at the site of the nucleus and remains unchanged farer out.

(iii) ΔE is proportional to the electron density at the nuclear site like in the case of the ordinary IS.

From these observations we learn that nuclear excitation effects are very similar to those which led to the corrected field shift formulae (2.11), (2.13), discussed in section 2.1.: There the Dirac wave function was readjusted from the point charge solution to the one obtained for an extended, static monopole charge distribution. The correction of the wave function considered here accounts in addition for the "dynamic" charge distribution of any multipole shape. Both effects are of second-order and hence a priori of comparable size. Hoffmann et al. have calculated the effect for some characteristic cases (Ho 84):

(i) ^{208}Pb: the <u>total</u> nuclear polarization effect ΔE amounts

to about 5 % of the ordinary $IS^{206/208}$. For such a stiff nucleus all of the excitation strength lies in the giant resonances which have a weak and smooth A-dependence. Hence the differential contribution $\delta(\Delta E)^{AA'}$ to the $IS^{AA'}$ is negligible.
(ii) The sudden onset of deformation in the Sm chain leads also to a sharp increase in the nuclear quadrupole polarizability. Whereas the expansion of the nuclear charge distribution lowers the electronic binding energy in first-order perturbation theory, the enhanced polarizability strengthens it in second-order. In that way the IS in the pair ^{150,152}Sm is reduced by 5 %.

In summary contributions from nuclear polarization to the IS are negligible in most cases, but are worth considering at shape transitions. Although this effect has been proved to be small, eventually, it had to be treated here, since the question was open or has simply been ignored for so many years.

4.5. The Exemplaric Region of Rare Earths and its Neighbourhood

4.5.1. Europium Isotope Shift

Many characteristic features of isotope shift and its relation to nuclear structure can be learned from the well investigated region of rare earths. Fig. 4.4 shows a plot of $\delta\langle r^2\rangle^{A,145}$ for Eu isotopes in the range $140 \leq A \leq 156$ (Dö 83, Dö 84, Al 83, Fe 84, Ah 85). The reference isotope $^{145}_{63}Eu^{82}$ has a closed neutron shell and the proton number is one below the magic Z=64

of Gd. Although the proton shell gap at Z = 64 is not as wide as at the major shell closures Z = 50, 82, it should establish in cooperation with the closed neutron shell a spherical ground state for ^{145}Eu. A straight line $\langle\beta_2^2\rangle^{1/2} = 0$ with the slope of the spherical droplet model $\delta\langle r^2\rangle_{sD}/\delta A$ has been plotted through that reference point, therefore. The assumption of zero deformation for closed shell nuclei cannot be valid in a strict sense, since at least the zero point motion of giant resonances is still present at the shell closures. Its smooth A-dependence cannot be verified in an analysis of $\delta\langle r^2\rangle$. Moreover, the strength of the shell-dependent low energy collective motion has not died out completely at shell closures, especially not for the octupole mode (compare section 4.8.1.) which we do not consider for the moment. On the other hand, a small residual deformation at the magic reference point will hardly influence the determination of $\langle\beta_2^2\rangle^{1/2}$ through eq. (4.10) for another isotope, if this is well deformed. This is seen easily from the progressive distance of equi-deformation lines in Fig. 4.4. Only close to $\langle\beta_2^2\rangle^{1/2} = 0$ the scale is critical.

4.5.1a. The Kink of $\delta\langle r^2\rangle$ at the Shell Closure. The point of shell closure is marked out by a characteristic kink of the $\delta\langle r^2\rangle$ plot. (Actually the kink is rounded somewhat by the strong odd-even staggering at N = 81 which may be ignored for the moment, (compare section 4.11.). Below N = 82 the ms radius remains almost constant, above it expands rapidly at twice the rate of the spherical droplet model. Although this kink signalizes a strong and very pertinent shell effect (compare also the figures below), it can hardly be explained within the limits of a strictly

spherical shell model. One could argue that the neutron distribution expands faster above the shell closure due to the new particles in the outer shell. The proton distribution would have to follow through the neutron proton force. From the view point of nuclear gross structure, however, it would cost a lot of energy to lower the central density in favour of the surface because of the high compression modulus of nuclear matter. Seen this way it seems cheaper to increase $\langle r^2 \rangle$ by deformation rather than by volume expansion. Adopting the latter interpretation of the kink the ms deformation increases steadily to both sides of the magic number at about equal rate. If one would choose $\delta\langle r^2 \rangle_{unif}$ from eq. (4.4) as basis for the volume effect of $\delta\langle r^2 \rangle$ then the equi-deformation lines in Fig. 4.4 would be a factor two steeper. That would imply the unphysical consequences of observing no deformation on the neutron-rich side but an extremely large one on the neutron-deficient side.

4.5.1b. The Shape Transition at N = 88. Another outstanding feature in Fig. 4.4 is the sharp jump of $\delta\langle r^2 \rangle$ at A = 151. The two stable isotopes ^{151}Eu and ^{153}Eu have represented for a long time the classical example of a nuclear shape transition which was discovered in the spectroscopic quadrupole moments (Sc 35, Ca 35) and later found to manifest itself also by an exceptionally large isotope shift (Br 52) (reviewed by Brix in ref. (Br 85)). A later off-line measurement on ^{152}Eu (He 71) made clear that the shape transition actually occurs between the 88th and 89th neutron in one single step. Very interesting is the intermediate position of the 0^--isomer ^{152m}Eu. The authors

conclude that it is a permanently deformed, prolate nucleus but with a single particle configuration completely different from that of the ground state (Dö 84, Eg 78). However, that interpretation does not advance an explicit argument in favour of the intermediate position which is never observed at other shape transitions unless they are washed out anyway (see below).

Beyond the point of transition nuclear shape seems to be stabilized; the rms deformation remains constant (apart from odd-even staggering) at the level $\langle\beta_2^2\rangle_{IS}^{1/2} = 0.32$. This value is to be compared with $\langle\beta_2^2\rangle_{BE2}^{1/2} = 0.31$ obtained from BE2($0^+ \rightarrow 2_1^+$) values (Lö 70) and with $\langle\beta_2\rangle_{Q_s} = 0.32$, derived from the spectroscopic quadrupole moment $Q_s = 2.414(21)$ (Ta 83) via eq.s (2.26, 4.20). The excellent consistency seems to confirm quantitatively the assumptions and prepositions involved in the different analyses, namely: (i) the evaluation of the field shift constant F (eq. (2.13)), (ii) the two parameter model and the droplet prediction for $\delta\langle r^2\rangle_s$, (iii) the closure relation (4.19) and in particular its truncation to the first BE2 value, (iv) the static character of the deformation, (v) the evaluation of Q_s from muonic spectra, (vi) the projection formulae (2.26, 4.3) with the strong coupling rule $\Omega = I$ for well deformed nuclei.

One must admit, however, that in other regions of nuclei this level of consistency is usually not reached. Moreover, a consistency on the level of accuracy of a few percent appears a bit fortiuous in view of neglecting higher-order corrections (see section 4.2.2.). But still the statement applies that the

two parameter model works the best in general, when it bridges large distancies between rigid spherical and rigid deformed nuclei.

4.5.2. Isotope Shifts in Xe, Cs, Ba

Due to the systematic measurements in recent years the neighbourhood of Eu has been explored in the extended area $54 \leq Z \leq 70$, $63 \leq N \leq 106$. Fig. 4.5 shows $\delta\langle r^2\rangle$ for Xe (Fi 74b), Cs and Ba (data and ref.s given in Table 7.1) at the low Z borderline of this region. They look similar to the Eu case except for the missing shape transition at N = 88. The neutron-rich Cs and Ba isotopes run completely steady and parallel to each other into deformation. $\langle\beta_2^2\rangle^{1/2} = 0.29$ is reached at N = 92 (Mu 83, We 87). For all three elements the reference point at N = 82 is chosen at $\langle\beta_2^2\rangle^{1/2} = 0.09$ which is derived from the $BE2(0^+ \rightarrow 2_1^+)$ value of ^{138}Ba. The kink at N = 82 is getting stronger with increasing distance from the closed proton shell Z = 50. This phenomenon reflects the well known fact that the deformation of the core increases with the total number of valence nucleons as has been formulated in a most simple way by Casten's empirical rule. It states that the value of a collective quantity is a function of the product $N_\pi \cdot N_\nu$, the number of proton and neutron pairs (or holes) in a shell (Ca 85c).

Very interesting is the staggering of Cs radii for very neutron-deficient isotopes and isomers (Th 81, Co 87). The spins of $^{119,121,122}Cs$ are 9/2, 3/2, 1, those of their isomers 3/2, 9/2, 8. The three high spin states are due to the $\pi[404]9/2$

Fig. 4.4: $\delta\langle r^2\rangle^{A,145}$-values in the series $^{140-156}$Eu with respect to the magic ^{145}Eu. Isomers are indicated by open circles. The straight lines are equi-deformation lines with the slope of the droplet model at N = 82. The weak curvature of the correct droplet line is neglected in the plot (data and references given in Table 7.1.).

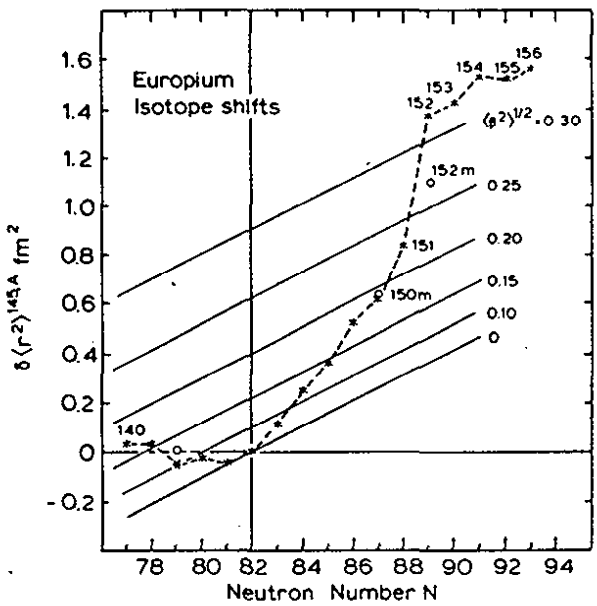

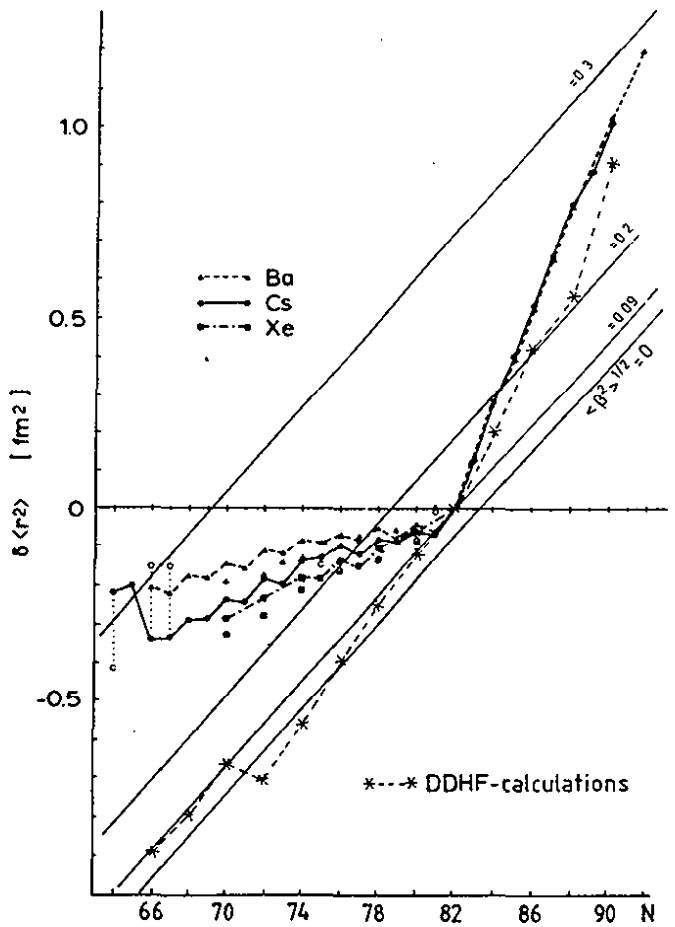

Fig. 4.5: Plots of $\delta\langle r^2\rangle^{N,82}$ for Xe (Fi 74), Cs and Ba (data and references for Cs and Ba given in Table 7.1). The open circles refer to isomers of Cs. Also shown are equi-deformation lines according to the droplet model and the result of a density-dependent Hartree-Fock calculation (stars) (Ca 75, Ep 81).

Nilsson level out of the $1g_{9/2}$ proton shell which is closed at Z = 50 already. But this level rises very steeply with deformation, passes the Fermi surface around $\beta_2 = 0.3$ and replaces beyond the $\pi[422]3/2$ level as ground state (Ek 81). That interchange happens between mass numbers 121 and 119. It is accompanied by a distinct increase of deformation as seen from the strong isomer shift.

Fig. 4.6, taken from Thibault et al. (Th 81b), compares deformation parameters of Cs isotopes derived from $\delta\langle r^2\rangle$ and Q_s values with those of Xe and Ba. The latter have been calculated from energies and transition strengths of the first 2^+ states. A similar systematics of off-line results in this region had been prepared by Ullrich et al. already (Ul 75). The more recent on-line optical experiments have expanded the scope by a factor two on the neutron-deficient side and have also added the neutron-rich branch N > 82. Thereby a much more complete view on the development of nuclear structure as a function of N has been reveiled. The consistency of data is convincing on the neutron-deficient side. In particular the $\langle\beta_2\rangle_{Q_s}$ values of the lightest isotopes constitute the first and only proof of a static and prolate deformation in this region. ß-values of Cs are framed in between those of Xe and Ba, as was observed for the isotope shift (Fig. 4.5). On the neutron-rich side $\langle\beta_2\rangle_{Q_s}$ is much smaller than expected from IS. The reasons are difficult to trace. Probably a static deformation is not established there. Q_s values of Ba isotopes do not give a clear answer either (Ek 81, Mu 83).

4.5.3. Heavier Rare Earths

The heavier rare earths Gd, Dy, Er, Yb have been investigated systematically by R. Neugart and collaborators (Bu 82, Ne 83, Ne 82, Ne 85). Although part of the numerous data has not jet been published in final form, the essential features are very clear and have been discussed at conferences (Ne 82, Ne 85, Ot 85c). Fig. 4.7 shows the ms deformation of some even elements in the range $78 \leq N \leq 106$ derived from $\delta\langle r^2\rangle$ as well as from $BE2(0^+ \rightarrow 2_1^+)$ values. The agreement is generally good. One notices again the sharp minimum at the shell closure, the symmetric rise at both sides of it, and the flat maximum of deformation around $N = 102$. One observes further that the drastic jump into deformed shape beyond $N = 88$ (which is strongest for Eu) is getting washed out for heavier elements. It has completely vanished for Yb at $Z = 70$ as well as for Ba at $Z = 56$ (mentioned already before). Nevertheless, the heavy Yb isotopes are well deformed nuclei, but the transition from spherical to deformed shape is smooth. Thus the sharp shape transition is confined to a few elements around $Z = 64$.

Local changes in the course of the IS can be accentuated in a differential plot $\delta\langle r^2\rangle^{N,N-2}$, the so-called Brix-Kopfermann plot (Ko 58). By this plotting the kink at the magic number transforms into a step, and the step at the shape transition into a needle as seen from Fig. 4.8. For the sake of clarity, only some of the more recently measured chains are shown and for even N only, except for the critical pair $N = 90,88$, at the place of the shape transition where all known data are given. One sees that the needle

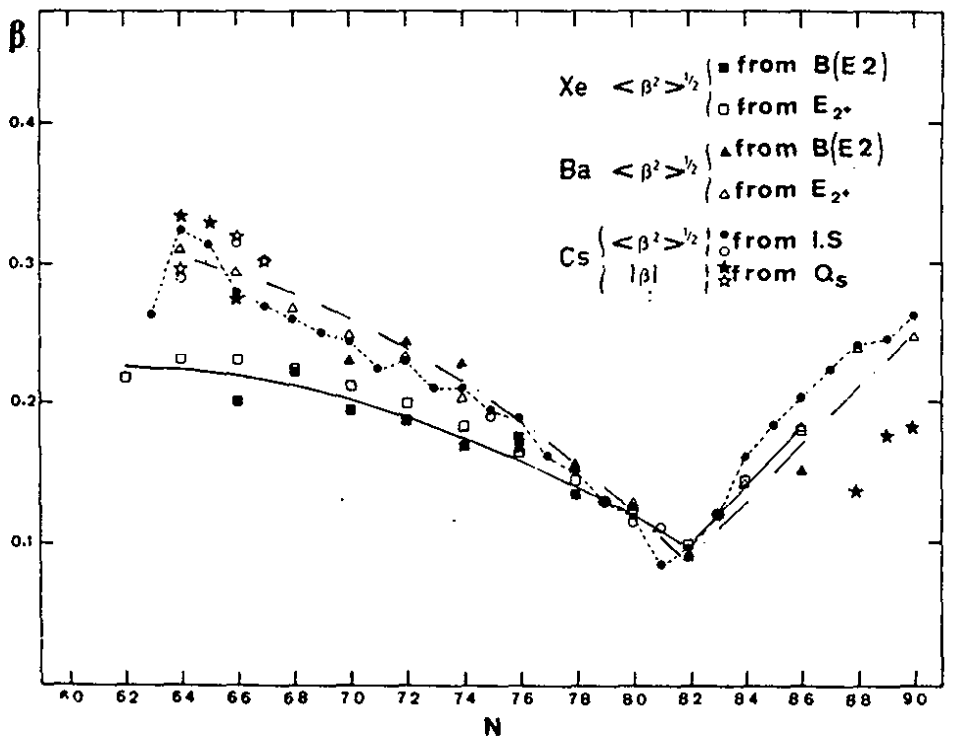

Fig. 4.6: Values of the deformation parameter $<\beta^2>^{1/2}$ for Xe and Ba deduced from B(E2) and E_2^+ and for Cs isotopes and isomers deduced from IS. Values of $<\beta>$ deduced from Q_s are also given for some Cs isotopes (full symbols) and isomers (open symbols) (Th 81b).

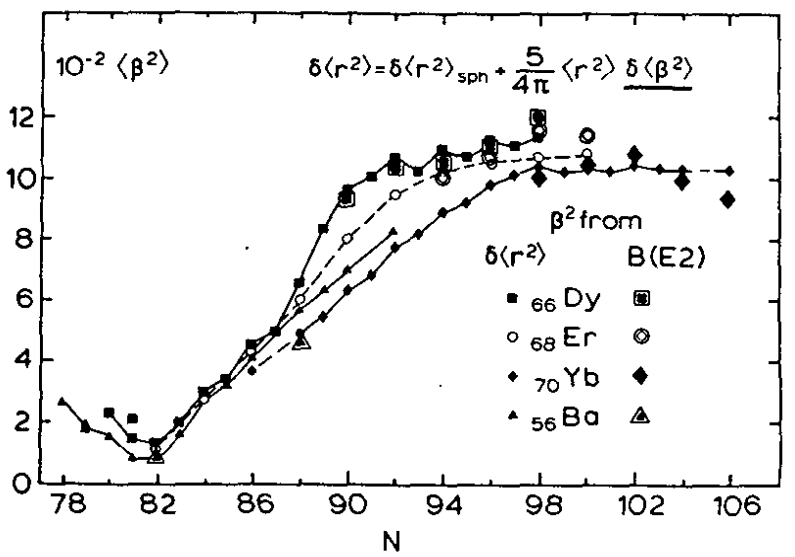

Fig. 4.7: Course of $<\beta_2^2>$ in the isotopic sequences of Ba, Dy, Er, Yb as determined from isotope shift data. Values from BE2-measurements are given by double symbols for comparison (Ot 85c).

is highest for Eu and decays gradually for the neighbouring elements. Also the step at the magic number N = 82 is a very clear and regular phenomenon.

4.5.4. Shape Transition and Subshell Closure at Z = 64

The localization of the shape transition around Z = 64 has been emphasized by Casten et al. on behalf of a systematics of energies of the 4^+ and 2^+ states in the ground state vibrational/rotational bands; it has been associated to the subshell closure at Z = 64 (Ca 81). Although that subshell closure lies in the middle of the major proton shell $50 \leq Z \leq 82$, it manages to keep the rate of deformation increase above N = 82 down to a moderate value which compares to the one observed for isotones farer off midshell. This goes on until the $f_{7/2}$ neutron orbits are filled at N = 88. Beyond that point, $\nu h_{9/2}$ orbits in cooperation with intruding $\pi h_{11/2}$ orbits drive the nuclei all of a sudden in a well deformed shape and eradicate the Z = 64 subshell gap (Fe 77, Fe 78). As soon as the proton subshell is dissolved into the major one for N > 88, the nuclei around Z = 64 now experience their midshell situation with a maximum number of active valence protons. Therefore, they attain a more deformed shape than their isotones farer off midshell which need still more neutrons to reach maximum deformation (compare also ref. (Ca 85c)). All these features can be recognized in Fig. 4.7 and Fig. 4.8.

4.6. The Rb Region

Fig. 4.9 displays $\delta\langle r^2\rangle$ for the span of 22 Rb isotopes (Th 81,

Fig. 4.8: Brix-Kopfermann plot of differential IS in the region of rare earths, normalized to the uniform shift eq. (4.4). The value expected from the spherical droplet model is shown for comparison (Ot 85c).

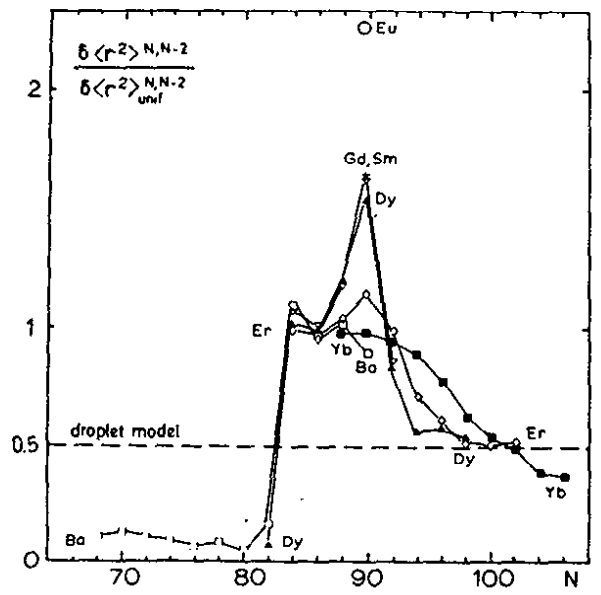

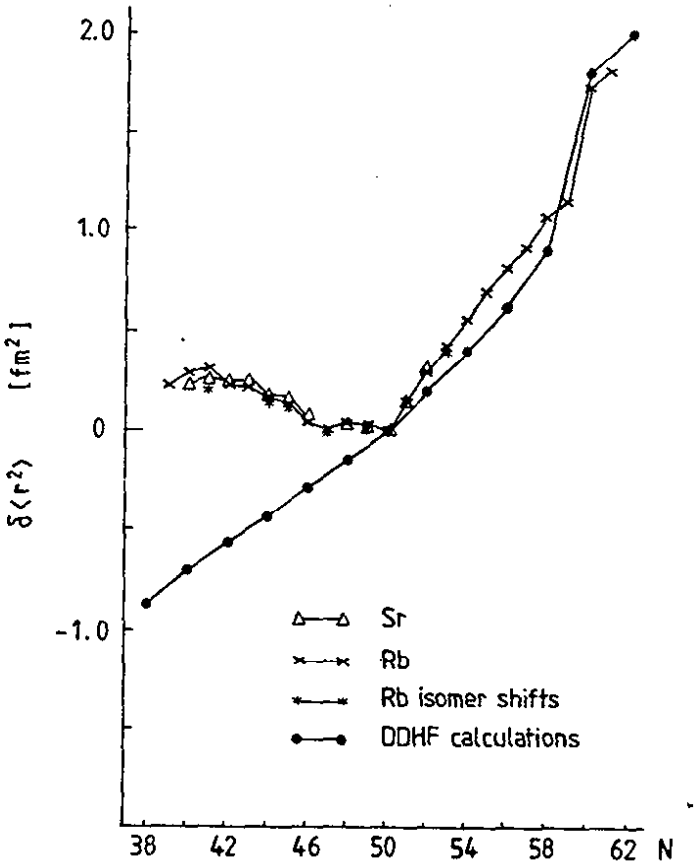

Fig. 4.9: $\delta\langle r^2\rangle^{N,50}$ for Rb and Sr isotopes together with equi-deformation lines according to the droplet model (data and references in Table 7.1). Theoretical results from a density-dependent Hartree-Fock calculation are also shown (Ca 80).

Kl 79b) together with data on Sr; the latter concentrate mainly on the neutron-deficient side (Bu 85, Ea 87). Comparison with the Eu plot, Fig. 4.4, e.g., shows that all the characteristics are repeated one shell lower. The kink at the magic number N=50 is still more accentuated, to the extent that the IS even reverses sign below. The magic isotopes ^{87}Rb, ^{88}Sr have the absolute smallest ms charge radius in their respective chains, even if compared to nuclei ten mass numbers below. This strong kink has been known from classical optical spectroscopy before (He 61), but limited close to stability of course.

4.6.1. The Shape Transition at N = 59

At N = 59 a shape transition to strong stable deformation occurs. Far off stability one has reached here a region of shape coexistence around Z = 38, N = 60 which has been extensively studied by nuclear spectroscopy in recent years (reviewed e.g. in ref. (Ha 85)). Similar to the rare earths region the shape transition is triggered by the competion of a spherical subshell gap at Z = 40 and a deformed shell gap at Z = 38. The latter is preferred when neutrons start to fill the $\nu g_{7/2}$ orbits around N = 60 and interact with intruding $\pi g_{9/2}$ orbits. Nuclear spectroscopy has observed spherical and deformed bands to coexist at almost degenerate positions in nuclei like $^{100}_{38}Sr^{62}$ or $^{100}_{40}Zr^{60}$ (Ha 85).

Optical spectroscopy has just touched this region. In addition to Rb, the Sr chain has been measured up to A = 100 (just at the time of finishing this manuscript); its isotope shift

runs in parallel to the one of Rb (Si 86). Beyond Sr a region of refractory elements starts, which hardly can be managed in on-line optical experiments for the time being.

A direct measurement of shape coexistence by the isomer shift would be extremely desirable but requires a sufficiently long isomeric lifetime. In odd nuclei around A = 100 one might have a chance to find one (compare the Hg case below).

Although optical spectroscopy on Rb so far covered only a few nuclear ground states in the critical region it yielded decisive information on the shape transition: (i) its size has been fixed from $\delta\langle r^2\rangle^{97,96}$ to be $\delta\langle\beta^2\rangle^{97,96}_{IS} = 0.08$. (ii) From spin and moments of ^{97}Rb, I = 3/2, $\mu_I = 1.84$, $Q_s = 0.6$ b, one obtains a prolate static deformation $\langle\beta_2\rangle_{Q_s} = + 0.33(3)$ and identifies the Nilsson state to be either [301]3/2 with μ_I = 1.9 or [431]3/2 with $\mu_I = 1.99$. These magnetic moments which were calculated with the particle plus rotor model fit for both states; but the calculation of energies by the shell correction method favours strongly the latter one (Ra 81).

4.6.2. The General Course of $\delta\langle r^2\rangle$ and Deformation Parameters

On the neutron-deficient side nuclear spectroscopy has not confirmed a clear cut, stable deformation, although the collectivity of transitions is high. However, Q_s values of ^{77}Rb and ^{76}Rb indicate strong prolate static deformation of $\langle\beta_2\rangle_{Q_s}$ = 0.31(5) and 0.52(20), respectively.

The evaluation of the total rms deformation from $\delta\langle r^2\rangle^{N,50}$ under the assumption $\langle\beta_2^2\rangle^{N=50} = 0$ leads to surprisingly high values, namely 0.38 for ^{76}Rb and 0.39 for ^{97}Rb. The BE2($0^+ \rightarrow 2_1^+$) value for ^{98}Sr yields $\beta_2 = 0.34$ (Wo 77) in agreement with Strutinsky-type calculations (0.35) (Ra 80) and density dependent Hartree-Fock calculations (0.36) (Ep 81). Closer to N = 50 the Rb isotope shift also indicates a considerably stronger deformation than BE2 values from neighbouring elements. Gerhardt et al. have observed and discussed this discrepancy in Kr isotopes already and introduced a variable skin thickness in order to remove it (Ge 79, Ge 81). Buchinger et al. have discussed the same phenomenon in Sr nuclei close to N = 50 (Bu 85). The problem is met in the Cd-Sn region again and will be discussed there in more detail (see section 4.8.).

4.6.3. Comparison to Microscopic Calculations of $\delta\langle r^2\rangle$

The Hatree-Fock calculation by Campi and Epherre (Ca 80) is quite successful in reproducing the Rb shape transition at the right place but overestimates its size appreciably. The kink at the magic number is virtually absent in the calculated line. Also the calculation in Ba failed to show the kink (Ca 75, Ep 81, compare Fig. 4.5). The authors explain this deficiency from the fact that their calculation includes only static deformation but not the dynamic one from the zero point motion of the collective modes. Therefore, the calculated $\delta\langle r^2\rangle$ line lies below the experimental one, except for the well deformed N = 60 case where the agreement is fairly good. Thus we can conclude again

that the deformation is static beyond the shape transition and that dynamic effects are small there as well as at the magic number.

4.7. The Mercury Region and the Problem of Shape Coexistence Near Closed Shells

4.7.1. Observation of Shape Staggering and Shape Isomerism

Historically the Hg chain was the first one investigated by optical means far off stability at an on-line mass separator. Unexpectedly a large, sudden increase in $\langle r^2 \rangle$ was discovered between ^{187}Hg and ^{185}Hg (see Fig. 4.10) and interpreted tentatively as a transition from weakly ($\beta_2 \approx 0.15$) to strongly deformed ($\beta \approx 0.27$) shape (Bo 72). In-beam γ-spectroscopy experiments on neighbouring even Hg isotopes, following soon after, did not confirm this finding with respect to the ground states; they continue being the head of a quasi-spherical band which is observed as well in all the heavier isotopes with remarkably constant parameters. Instead they found a coexisting, excited band whose energies and transition strengths fitted to the large deformation claimed from the isotope shift (Pr 73, Ru 73, Co 76). The experimental and theoretical literature on the problem up to 1976 is summarized in ref. (Bo 76).

Laser spectroscopic experiments corroborated later the quasi-spherical shape of the even isotopes down to ^{182}Hg by the observation of an extremely large odd-even staggering (Kü 77, Ul 86). In addition a shape isomerism was discovered in ^{185}Hg

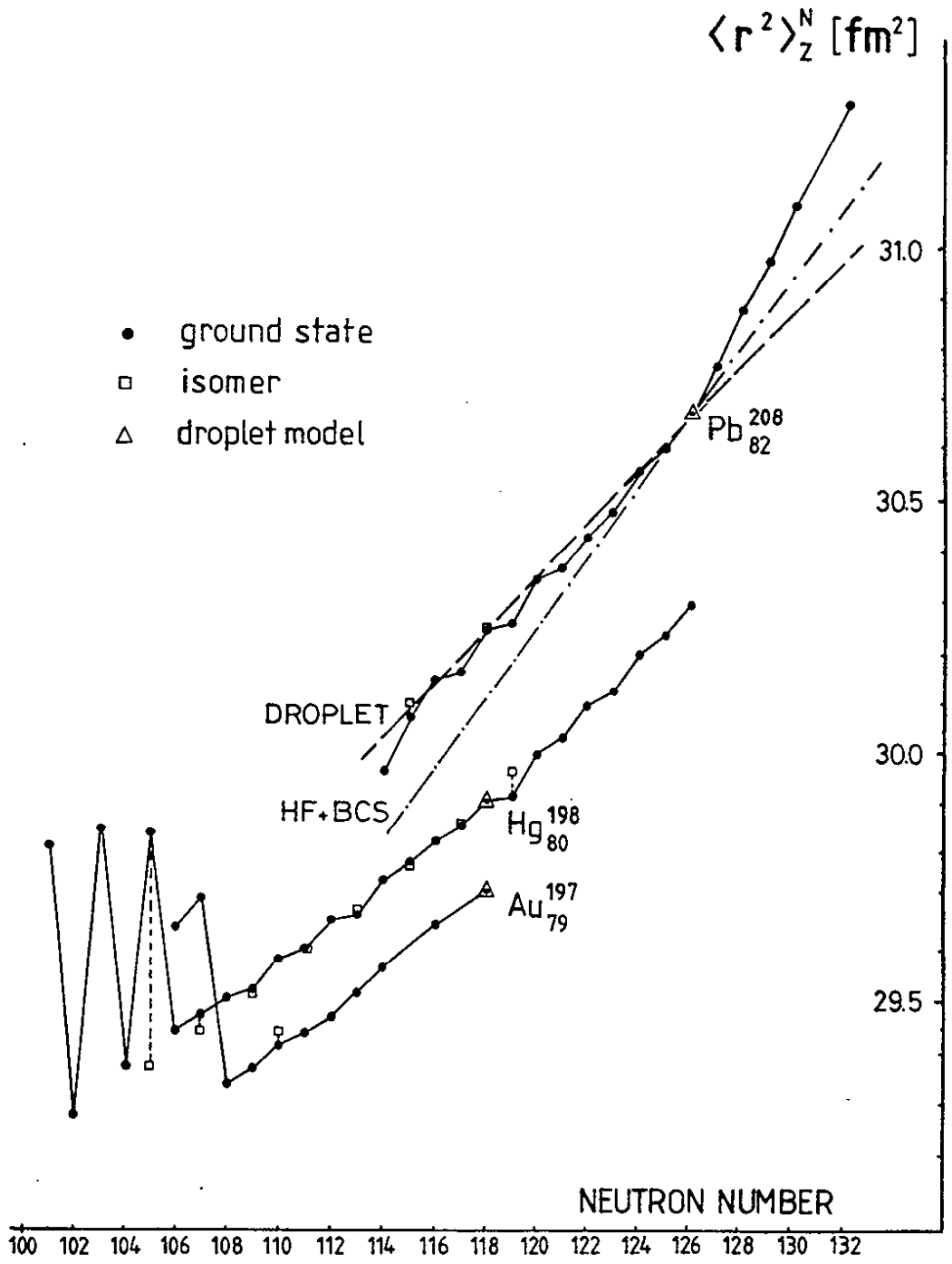

Fig. 4.10: Change of $\langle r^2 \rangle$ in the isotopic sequences of Au, Hg, Pb. The scales have been fixed at ^{208}Pb, ^{198}Hg and ^{197}Au by the droplet model (for simplicity). Isomers are indicated by open squares (data and references given in Table 7.1).

by a huge isomer shift between the deformed ground state and a quasi-spherical $i_{13/2}$ isomer (Da 79). Fig. 4.10 shows the course of $\delta\langle r^2\rangle$ for Hg and the neighbouring elements Au, Pb.

The deformed states in ^{181,183,185}Hg are clearly identified by their spin I = 1/2 and moment $\mu_I \approx 0.5$ n.m. as the [521]1/2 Nilsson orbit. Unfortunately no Q_s value could be measured so far in the deformed region, neither for Hg because of I = 1/2, nor for ^{185,186}Au because of J = 1/2 of the atomic states involved (Wa 87). In a recent up-date of Hg data (Ul 86) reanalyzed rms deformation parameters for the isotopes ^{181,183,185}Hg are given as $\langle\beta_2^2\rangle_{IS}$ = 0.28, 0.27, 0.25, respectively, in accordance with the original numbers, quoted above.

4.7.2. Interpretation of Shape Coexistence

In the first years after the discovery of a shape transition so close to the magic proton number Z = 82 different theoretical explanations were given. Most calculations were performed with the Strutinsky or with the density-dependent Hartree-Fock (DDHF) method. Based on a paper by Wong (Wo 72) and the observation of missing rotational fine structure in α-decay, Hornshøj et al. (Ho 73) speculated about a central depression of charge density in light Hg isotopes, so-called bubble nuclei. The bubble hypothesis was disprooved by Beiner and Lombard (Be 73) and by Nilsson et al.; the latter authors concluded that the increase in $\langle r^2\rangle$ is only by parts due to deformation and predominantly caused by an increase in proton surface density as

a consequence of occupying large (n,l)-orbitals (Ni 74). A similar interpretation was given recently again by Krygin and Metroshin (Kr 85). Faessler et al. (Fa 72), Dickmann and Dietrich (Di 73,74), Cailliau et al. (Ca 73), Kolb and Wong (Ko 75) and Frauendorf and Pashkevich (Fr 75) explained the effect as a transition from small oblate to strong prolate deformation.

Frauendorf and Pashkevich were also the first who gave a satisfactory explanation of the odd-even shape staggering. Fig. 4.11 shows potential energy surfaces for Hg isotopes from their paper. All cases shown exhibit a nearly spherical oblate minimum and a more deformed prolate one which are competing. The former is caused by the almost closed proton shell, the latter by the open neutron shell. ^{184}Hg and odd masses $A \geq 187$ favour the oblate minimum, odd masses $A \leq 185$ the prolate one in agreement with experiment. The physical explanation of the odd-even staggering is found in the difference of neutron pairing energy on both sides. On the oblate side it is strong, because of the high level density in the open spherical shell; on the prolate side it is lower, since the level density at the Fermi surface has relaxed due to the presence of the gap of the deformed neutron shell. Thus pairing is able to stabilize in cooperation with the preferred proton configuration the almost spherical shape of the even nuclei even up to the middle of the neutron at $N \approx 104$. For odd neutron numbers, however, pairing is weakened by the blocking effect; from a certain point on these nuclei swap over to the prolate side, therefore. The balance between the two minima is obviously very delicate. This is also seen

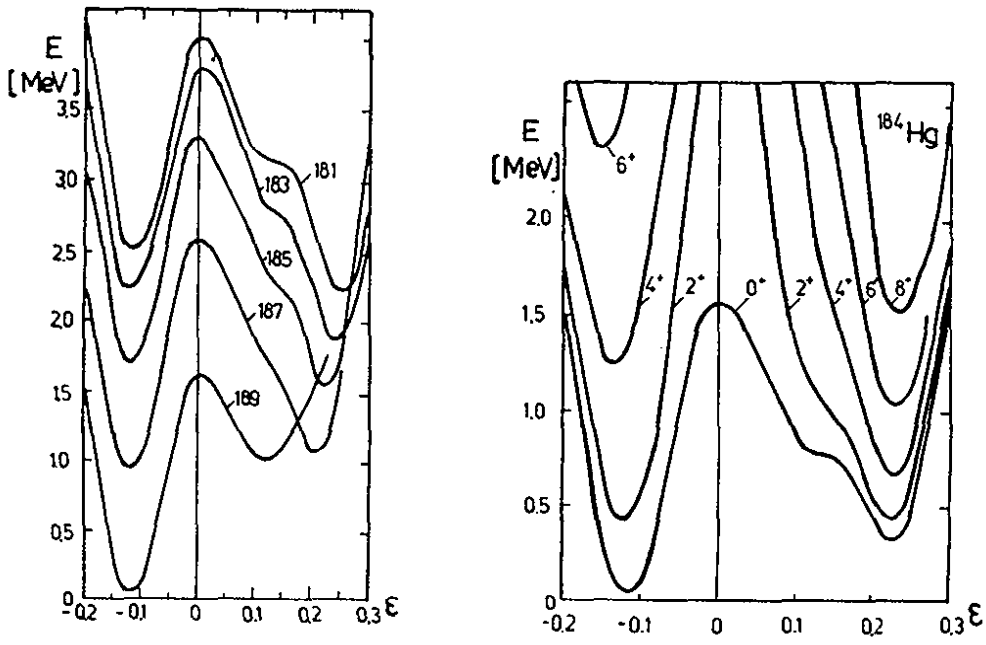

Fig. 4.11: Deformation energy of the odd-mass Hg isotopes (left) and of the rotational states in ^{184}Hg (right). Hexadecapole deformation α_4 is equal to -0.02 (Fr 75).

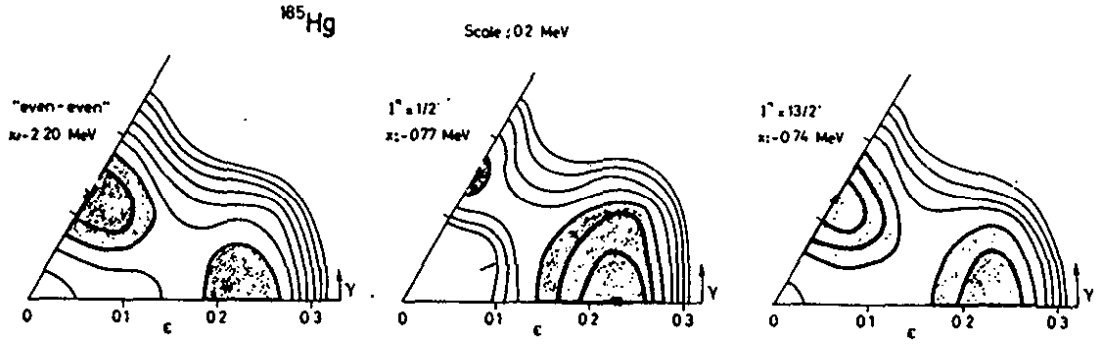

Fig. 4.12: Potential surfaces in the ε,γ-plane for ^{185}Hg. Left: for the ^{184}Hg core, calculated with a Strutinsky-like method. The odd particle added in a $1/2^-$-state (middle) and in a $13/2^+$-state (right), calculated by the particle plus rotor model. Equi-potential lines are plotted with a spacing of 0.2 MeV (Ra 80).

from the low lying 0_2^+-deformed band head in ^{184}Hg at 375 keV (Co 76). Already in the neighbouring ^{185}Au neutron-pairing is not sufficient anymore to stabilize a spherical ground state which underlines again the critical energy balance. But also in Au the deformed region starts with an odd neutron number (107 instead of 105 in Hg) (Wa 87).

Ragnarsson treated the problem of the ^{185}Hg isomer in a triaxial calculation of the potential energy surface in the β,γ plane (see Fig. 4.12). He could locate a minimum for the $i_{13/2}$ state on the oblate and for the [521]1/2 state on the prolate side at almost degenerate positions in agreement with experiment (Ra 80). Fig. 4.12 shows, moreover, that the two minima are separated only by a rather shallow saddle, whereas the path along the γ = 0°, 60° axes through the point of shpericity at the origin has to surmount a substantially higher barrier. This is a characteristic feature of all calculations in this region which include the γ-degree of freedom to allow for triaxiality. It is well known also that the spectra of heavier Hg isotopes correspond well to γ-deformed or γ-unstable nuclei (Ha 85). In the context of shape coexistence it is difficult to understand, however, why the γ-instability, sometimes also called "γ-river", apparently does not bring about any substantial shape mixing. This is seen e.g. from the isotope shift which distinguishes two absolutely separate classes of nuclei. Also the monopole strength between the two 0^+ band heads in ^{184}Hg is weak (Co 76) and implies a mixing amplitude of 8 % only (Kü 77). If the potential energy surfaces have been calculated correctly, then the

problem could lie with the effective masses of the γ-vibration which for some reason might get very high at a certain point. Girod and Reinhard have investigated the problem more recently by an elaborate triaxial Hartree-Bogoljubov calculation using the Gogny force. Collective motion was treated by the Cranking model. They find the potential energy surface of even isotopes as well as the effective masses as functions of γ to be smooth. They expect the ground state of ^{184}Hg and ^{182}Hg on the prolate rather than on the oblate side. But the energy differences are marginal. Furthermore, they find that an odd neutron substantially reinforces the minima on both sides depending on its particular state; thus they can explain shape isomerism in ^{185}Hg (Gi 82).

Nuclear spectroscopy has traced the proton configurations which trigger the shape transition in cooperation with the large number of valence neutrons (reviewed e.g. by Heyde et al. (He 83) and Hamilton et al. (Ha 85)). In Tl and Au spectra it has been observed that the spherical $\pi h_{9/2}$ orbit from across the Z = 82 shell gap steps down systematically in energy with decreasing N and finally forms a $5/2^-$ ground state in ^{185}Au in a complicated coupling to the deformed core (Po 83, Bo 82). The downsloping intruder reveals that it costs little energy only to promote a proton pair from the full $h_{11/2}$ to the empty $h_{9/2}$ shell. In the even Hg core, for instance, this mechanism would produce altogether 6 active valence protons (2 particles and 4 holes) which drive the core to deformation in cooperation with the valence neutrons. Isotope and isomer shift measurements in light Tl isotopes have revealed, in fact, that the $\pi h_{9/2}$ intruder isomer is distinctly more deformed than the corresponding $\pi s_{1/2}$ ground state (Bo 85b). In ^{193}Tl the isomer shift corresponds to $\delta\langle\beta^2\rangle^{9/2,1/2} = 0.015$.

4.7.3. The Isotope Shift around the Double Shell Closure at ^{208}Pb

The course of $\delta\langle r^2\rangle$ of the heavier Au, Hg and Pb isotopes below the shell closure is remarkably straight and, moreover, rather parallel to the droplet line, especially for Pb and for Hg in the range $120 \leq N \leq 126$. Pb shows a kink at the magic number again but positively smaller than observed for lighter elements (compare figures above). Certainly the presence (or neighbourhood) of the proton shell closure plays a role in this question. But still in Ra which lies already 6 protons above shell closure the kink is rather flat (see Fig. 4.24). In general one gets the impression as if the kink decreases from one major shell to the next. That is to say that a small core polarizes easier than a big one.

Another interesting difference to the situation at lighter N-shell closures is the asymmetry of the two $\delta\langle r^2\rangle$ branches of Pb with respect to the droplet line. An interpretation in terms of no core polarization below and a rather strong one above $N = 126$ seems strange. One could argue that higher multipole deformations contribute in addition to the quadrupole mode and that this contribution steadily increases across the shell closure. This would help to restore the symmetry around $N = 126$ with respect to quadrupole polarization, but shifts the problem of asymmetry to the higher-order polarizations. Andl et al. (An 82), and Barranco and Broglia (Ba 85) have discussed ground state correlations due to octupole vibrations and their influence on the variation

of ms charge radii of Ca isotopes. They are found to be very important in ^{40}Ca and decrease for the heavier isotopes. The question of higher multipole contributions in the N ≲ 126 region was also discussed by Ulm et al. (Ul 86) in the analysis of heavy Hg isotopes; but they saw no chance for giving a conclusive answer to that question at the present stage of experimental information. For N > 126, on the other hand, it is known that the octupole strength increases strongly due to the $g_{9/2}$ valence neutrons which have large octupole matrix elements connecting to $\nu j_{15/2}$ states (Bo 75, Kl 82).

Thompson et al. (Th 83) have performed HF and BCS calculations of ms charge radii of Pb isotopes, using Skyrme III forces. They calculate a slope of $\delta\langle r^2\rangle$ being about 15 % steeper than obtained from the droplet model (My 83). The distance of the calculated line from the experimental data is now more symmetric for the even isotopes, but cannot be brigded by the $\langle\beta_2^2\rangle$ contribution as calculated from the (few) measured BE2 values; these are too small as observed in Rb already. Again the microscopic calculation gives practically no evidence for a kink at the magic number as observed already for Rb and Ba.

An increase of the standard droplet slope of $\delta\langle r^2\rangle_{sD}$ by about 10 - 15 % in the lead region was suggested further by Berdichevsky and Tondeur on the basis of another microscopic calculation (Be 85) and also by Möller et al. who advanced the droplet model to include finite range forces (Mö 84).

Ulm et al. (Ul 86) applied the standard droplet model to evaluate $\langle\beta_2^2\rangle_{IS}$ of Hg isotopes and found good agreement with $\langle\beta_2^2\rangle_{BE2}$ below ^{198}Hg. If the higher slope was adapted instead,

the former would be raised over the latter. In view of the same discrepancy observed elsewhere this would not come unexpectedly, in fact. In the next section that problem will be treated in more detail.

4.8. Parabolic Isotope Shifts and the Question of Large Core Polarization in Regions of Closed Proton Shells

4.8.1. Isotope Shift and Core Polarization in Ca Nuclei

Ca is the only element (besides its neighbour K) for which IS measurements cover a full neutron shell, namely the $\nu\ 1f_{7/2}$ shell between ^{40}Ca and ^{48}Ca, a small one, admittedly. The even isotopes in the series which are all stable have been investigated in addition by any method yielding information on charge and mass distribution: Coulomb excitation, muon spectroscopy, electron scattering, hadron scattering, etc. The treasure of data comprises, therefore, not only precise ms radii but also form factors and their isotopic change (for a synopsis see (Re 79)). The isotope shift, shown in Fig. 4.13 (An 82) is characterized first of all by the astonishing fact that the two double magic nuclei ^{40}Ca and ^{48}Ca have the same ms charge radius. Electron scattering experiments have revealed that the charge distributions $\rho(r)$ themselves are not identical, however. Their change has been shown in Fig. 2.4 already in the form $r^2\ \Delta\rho(r)^{48,40}$. Charge has flown from the center and from the outer skin into a region around the half density radius c. Since the total area under this curve is zero it leaves $\langle r^2 \rangle$ unchanged (Em 83).

One has to keep in mind that (elastic) electron scattering measures the monopole charge distribution averaged over all possible multipole deformations. The latter manifest themselves by simulating an increased skin thickness of $\rho(r)$ which cannot be discriminated from a possible change of the intrinsic charge distribution. The same is true for the isotope shift. In this picture the two parameter model (4.10) would be changed, therefore, to

$$\delta\langle r^2\rangle = \delta\langle r^2\rangle_s + 3\delta\sigma^2 \qquad (4.23)$$

The change in skin thickness may be calculated from eq. (4.23) by inserting experimental values on the left and the droplet expectation $\delta\langle r^2\rangle_{sD}$ on the right side. The result is a shrinking of σ^2 by 0.166 fm^2 in between ^{40}Ca and ^{48}Ca; or based on the assumption σ^{40} = 0.99 fm, σ^{48} would have dropped down to 0.90 fm.

Andl et al. (An 82) have pointed out already that at least the major part of this effect can be attributed to collective $\langle\beta_2^2\rangle$ and $\langle\beta_3^2\rangle$ contributions (see also the general theoretical treatment of the problem for nuclei in this region by Reinhard and Drechsel (Re 79b)). The octupole zero point motion as calculated from the transition strength to the first 3^--state is very large in ^{40}Ca and decreases to a small value in ^{48}Ca. This decrease just compensates the increase in $\langle r^2\rangle_{sD}$. The quadrupole strength is small at both shell closures and maximizes in between; it thus explains part of the bump of $\delta\langle r^2\rangle$ in the

middle of the shell. Barranco and Broglia (Ba 85) have taken up the problem again and performed a full theoretical calculation of ms deformations up to $\langle\beta_5^2\rangle$ for the even isotopes. For ^{40}Ca they calculated a total ms deformation $\sum_{i=1}^{5} \langle\beta_i^2\rangle$ as high as 0.30 and for ^{48}Ca still a value of 0.16. Adding these deformation corrections to the droplet value $\delta\langle r^2\rangle_{sD}$ according eq. (4.10) yields curve c in Fig. 4.13. It lies about 0.1 fm^2 below the experimental line but reproduces its structure fairly well, at least in comparison to the pure droplet model. The remaining difference may or may not be interpreted as the residual "non-collective" change of skin thickness. It could be attributed as well to deficiencies of the collective or of the droplet model. After all, one cannot expect gross models to represent the exact nuclear wave function in any detail. It should be noted here that the isotope shift of K (To 82b) shows a similar shape as that of Ca (compare Table 7.1); grosso modo it may be interpreted on the same lines therefore.

4.8.2. The Occurence of Parabolic Shapes of $\delta\langle r^2\rangle$ and the Zamick-Talmi Model

Apart from odd-even staggering the Ca isotope shift has apparently a parabolic shape with a maximum in the middle of the shell. Parabolic shapes of $\delta\langle r^2\rangle$ are met quite frequently in regions where abrupt shape transitions do not occur. Also isotonic shifts can show this behaviour as seen from Fig. 4.14 where differential isotone shifts $\delta R^{Z,Z-2} \approx (1/2)\langle r^2\rangle^{-1/2}\delta\langle r^2\rangle^{Z,Z-2}$ are plotted for stable nuclei in the $\pi 1f_{7/2}$ shell and the fol-

Fig. 4.13: Plots of $\delta\langle r^2\rangle^{A,40}$ in the Ca series (data and references given in Table 7.1): a) experiment, b) droplet model, c) droplet model plus contributions from deformation (Ba 85), d) fit of the data to the Zamick-Talmi model (Ta 84).

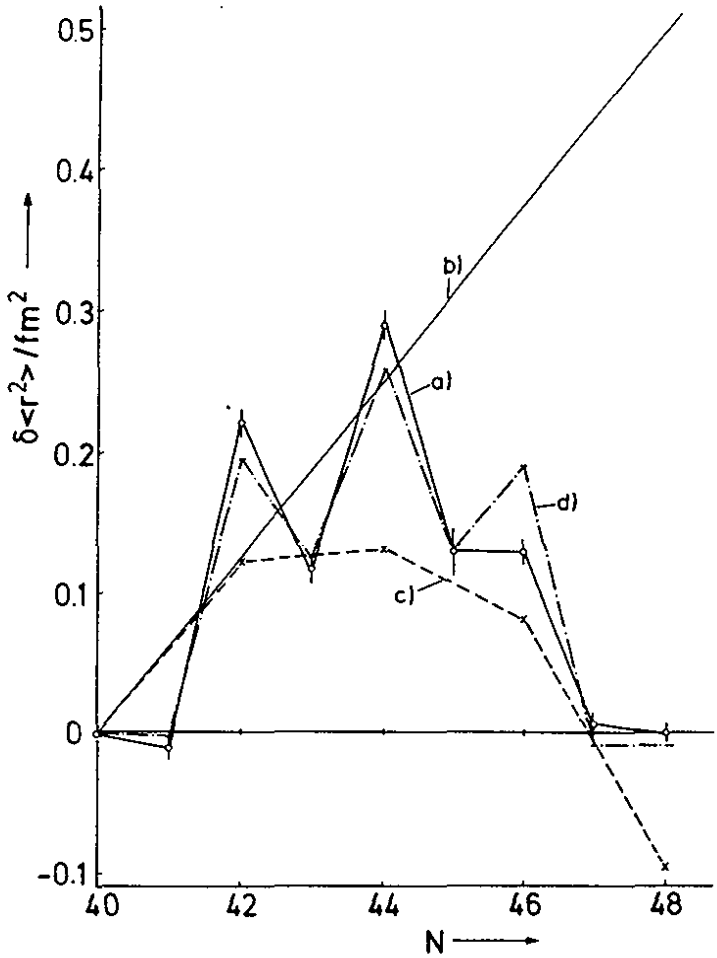

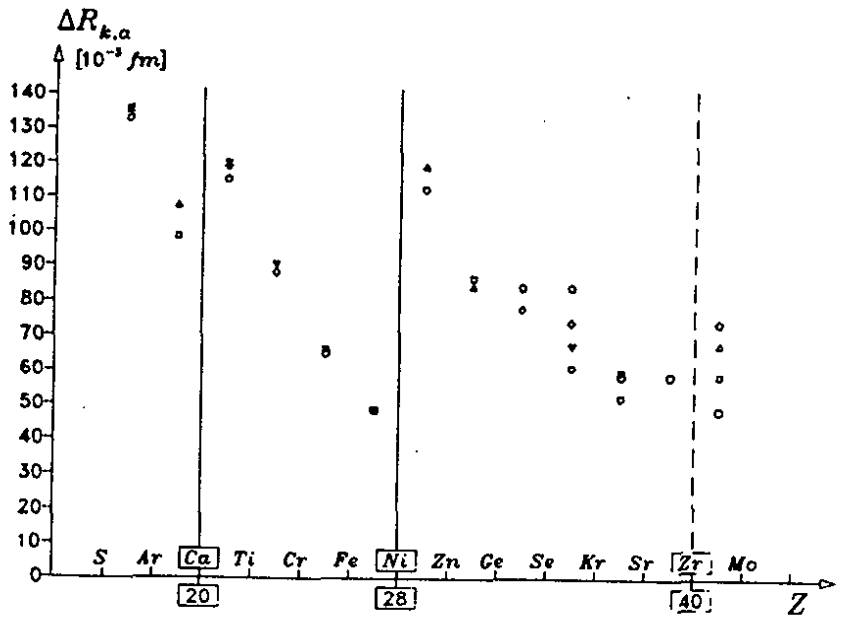

Fig. 4.14: Differential isotone shifts $\delta R^{Z,Z-2}$ for even elements within the shells $20 \leq Z \leq 28$ and $28 \leq Z \leq 40$ (Fr 81, Fr 86).

lowing one up to Z = 40; they were obtained from electron scattering and muonic spectra (Fr 81 , Fr 86). The data are consistent with a downsloping straight line in each shell. This corresponds to an integral shift of parabolic shape with negative curvature as observed in Ca. The step at Z = 28 corresponds to the well known kink of the integral shift, discussed above, with which the parabola of the next shell starts.

A parabolic shape may also be attributed to the course of the ms deformation $\langle\beta_2^2\rangle^{N,82}$ of Yb which lies just outside the shape transition region of rare earths (compare Fig. 4.7). The most conspicious examples of this kind are found for the isotope shifts of Cd (Bu 87), In (Ul 85, Eb 87b) and Sn (An 86, Lo 85, Eb 87) which are shown in Fig. 4.15. They fit perfectly to a polynomial of second order. It may be written in the form

$$\delta\langle r^2\rangle^{N,50} = a(N-50) + b(N-50)(82-N) + (1/2)\, c(1-(-1)^N) + d \qquad (4.24)$$

such that the quadratic term maximizes at midshell. The parameter c describes the odd-even staggering assumed to be a constant over the shell. (The offset d is introduced for optimizing the fit and has no further physical relevance).

A parabolic model which includes odd-even staggering was introduced by Zamick to fit the Ca charge radii (Za 71) in formal analogy to an identical equation derived by Talmi and Thieberger (Ta 56) for the isotopic dependence of the nuclear binding energy. When isotope shifts of odd Ca-isotopes became

available later, Träger showed that they also fitted nicely into the model (except for ^{46}Ca) (Tr 81).

Talmi has taken up the problem recently again and gave an explicit derivation of eq. (4.24) in terms of a core polarization of nuclei with closed proton shells by valence neutrons in a pure νj^n shell model configuration and in states of lowest seniority (Ta 84). For the contribution of an even multipole polarization of order $2\ell > 0$ the dependence of $\langle r^2 \rangle$ on the occupation number n is given by:

$$\delta\langle r^2\rangle^{(n)} = \frac{2|\langle j||T_\nu^{(2\ell)}||\rangle|^2}{(2j+1)(2j-1)} \left[n(2j+1-n)-(1/2)(1-(-1)^n)(j+1/2)\right] \quad (4.25)$$

The factor in front of the right side of eq. (4.25) is the reduced matrix element of the multipole operator acting on a single neutron in a state νj. The first, quadratic term in the bracket is proportional to the number of particles times the number of holes and is symmetric in both like in the ansatz (4.24). The second term describes a constant odd-even staggering with a negative sign.

Monopole polarization gives rise to a n^2-dependence of $\langle r^2 \rangle$ with positive curvature. The data give no evidence for such a term being present. Odd multipoles contribute with a positive, constant term for all odd-n but do not contribute at even-n. They give also rise to an odd-even staggering but with a sign opposite to that of the even multipole case. An expansion of the ms core radius proportional to $A^{2/3}$ is not considered in the model.

Andl et al. (An 82) have fitted eq. (4.25) to $\delta\langle r^2\rangle$ values of Ca and got a qualitatively correct shape and indication of odd-even staggering. Talmi (Ta 84) performed the fit with the more general Zamick formula which has three free parameters ε, α, β (Za 71)

$$\delta\langle r^2\rangle^{40+n,40} = \varepsilon n + \frac{\alpha}{2} n(n-1) + [\frac{n}{2} - (1-(-1)^n)/4]\beta \qquad (4.26)$$

He got a better fit, of course, but on cost of a stringent interpretation; his fit is included in Fig. 4.13.

In a major neutron shell the n-dependence of core polarization of semi-magic nuclei is still given by eq. (4.26), at least for even-n, under certain conditions also for odd ones (Ta 84, Ta 71). The odd-even staggering would again be constant over the shell. Eq. (4.26) preserves the quadratic character of eq. (4.24) and eq. (4.25).

4.8.3. Interpretation of Parabolic Shapes in Terms of the Two Parameter Model in the Cd, In, Sn Region

Since the parameters of eq. (4.26) are not related to each other, it gives no information about the form of the parabola. Physically it is evident that it still should have its vertex in the middle of the shell. Namely, if the polarization amplitude is made up by some coherent, residual interaction of the pairs in the valence shell, then it should be proportional to their number. This explains $\delta\langle r^2\rangle$ to be a quadratic function of that

number. Since, moreover, this interaction is limited tc the valence space of the major shell in question and since it obeys the Pauli principle, it should be symmetric in particles and holes; hence it should maximize in the middle of the shell as well as eq. (4.25) did. With these assumptions made the quadratic term in eq. (4.24) would be identified most naturally with the ms deformation $\langle\beta^2\rangle$. Under the additional assumption $\langle\beta^2\rangle^{N=50} = \langle\beta^2\rangle^{N=82} = 0$, it follows

$$\langle\beta^2\rangle^{N}_{model} = \frac{4\pi}{5} b(N-50)(82-N) \qquad (4.27)$$

where any residual, shell-independent deformation at the shell closures has been neglected (Bu 87). Application of eq. (4.27) implies that the fit can be extrapolated to the shell closures which have not been reached jet experimentally in the Cd-Sn region. But there is no reason to expect any strange bending or discontinuity in the course of $\delta\langle r^2\rangle$ on its final, short path to the shell closures.

Since the explicit formulae for multipole core polarization by a single j shell discussed above did not exhibit any linear n-dependence, the a-parameter in eq. (4.24) might be fully attributed to a quantity outside the core poalrization model, namely to the volume effect $\delta\langle r^2\rangle_s$. Fitting eq. (4.24) to the data yields a(Cd) = 0.047 fm^2, a(In) = 0.060 fm^2, a(Sn) = 0.065 fm^2; the droplet model predicts a $\approx$ 0.055 fm^2 in fair agreement with the average of the data. By fitting the parameter b one obtains from eq. (4.27) the ms deformation at mid-

shell as $\langle\beta^2\rangle^{N=66}_{model} = 0.078, 0.048, 0.032$ for Cd (Bu 87), In (Eb 87b), Sn (Eb 87). Note that the model yields the center deformation only from the curvature of the experimental $\delta\langle r^2\rangle$ curve without explicit reference to any other input data.

Fig. 4.16 shows $\langle\beta^2\rangle_{IS}$ for Cd calculated from $\delta\langle r^2\rangle^{N,66}_{exp}$ by use of the two parameter model (4.10) with $\delta\langle r^2\rangle_s$ taken from the droplet model and using $\langle\beta^2\rangle^{N=66}_{model} = 0.078$ as reference point (Bu 87). Alternatively one could adapt $\langle\beta^2\rangle^{N}_{model}$ from eq. (4.27) as final result of the analysis for all N. Both differ systematically, if the fitted parameter "a" in front of the linear term of eq. (4.24) does not agree with the droplet slope $\delta\langle r^2\rangle^{N,N-1}_{sD}$. The question which one comes closer to thruth can hardly been answered, since both ways are running risks of introducing systematic errors.

Surprisingly enough the rms deformation reaches a maximum as high as 0.28 for Cd at midshell. In fact, $\langle\beta^2\rangle_{IS}$ values are about a factor of two larger than those calculated from BE2 ($0^+ \rightarrow 2^+_1$) values as can be seen from Fig. 4.16. The same proportion is observed in In between $\langle\beta^2\rangle^{1/2}_{IS}$ and $\langle\beta\rangle_{Q_s}$, where the latter is derived from Q_s values in the strong coupling limit $\Omega = I$ by eq. (2.26) (see Fig. 4.17) (Eb 87b).

In both cases shown, but also in Sn, the IS reveals a much stronger collective contribution to $\langle r^2\rangle$ than expected from the simple model of vibrational or static quadrupole deformation. In the latter case one could argue that the contribution of

Fig. 4.15: Plots of $\delta\langle r^2\rangle$ for Cd, In, Sn (data and references given in Table 7.1). The Cd and In curves have been lowered at the reference point N = 66 by 0.4 fm² and 0.2 fm², respectively, for convenience. The broken lines are fitted parabolas with odd-even staggering according to eq. (4.24). Also shown is the droplet line.

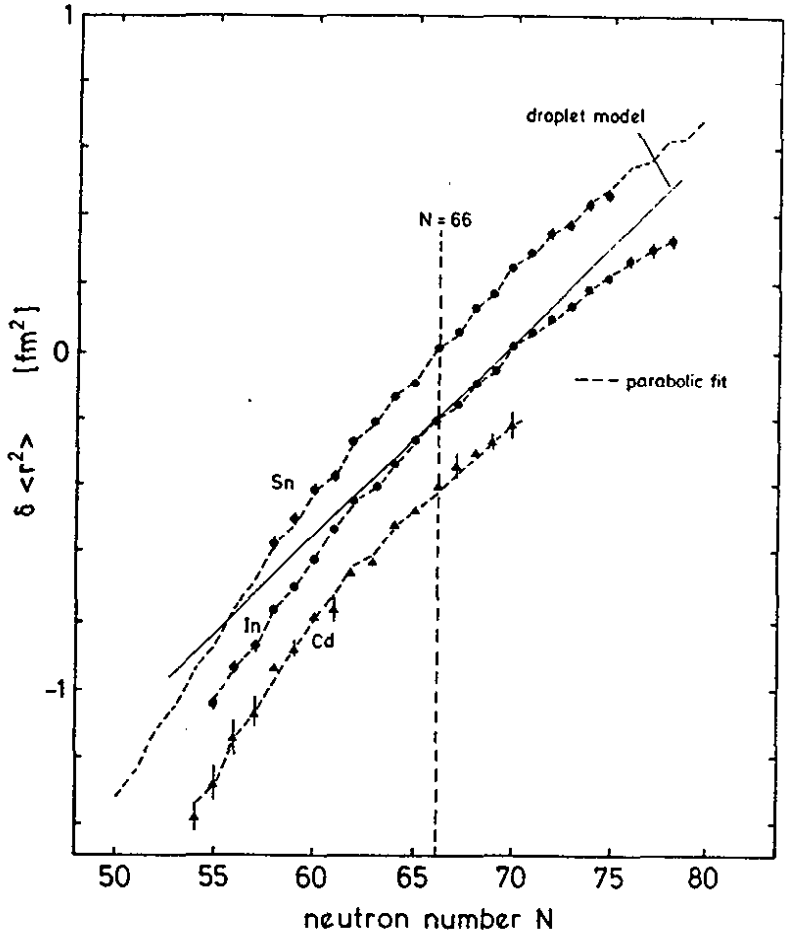

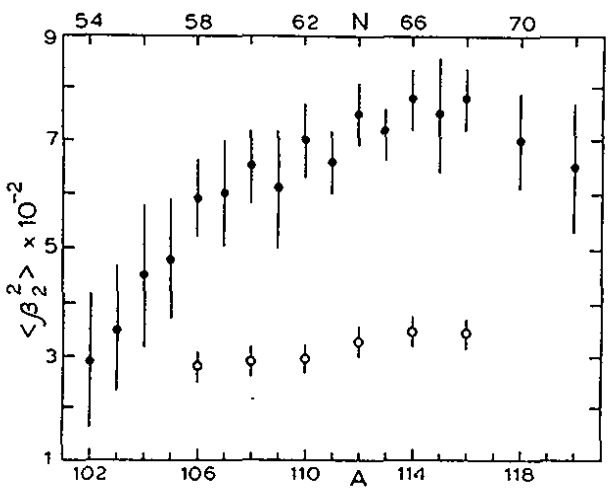

Fig. 4.16: $\langle\beta^2\rangle$ of Cd ground states from $\delta\langle r^2\rangle$ (full dots) compared to those derived from BE2($0^+ \rightarrow 2_1^+$) values (open circles) (Bu 87).

zero point motion to Q_s and hence to $\langle\beta\rangle_{Q_s}$ cancels. Regarding the missing strength in $\langle\beta_2^2\rangle_{BE2}$ one must admit that the truncation of eq. (4.19) is certainly unjustified in case of anharmonic vibration. Strong anharmonicity of a soft mode is postulated e.g. in the Jahn-Teller model of nuclear deformation (Re 84). Moreover, the question is open to what extent multipoles other than quadrupole may contribute to the ground state collectivity of the Cd-In-Sn region. But they are expected to be much weaker than observed in the Ca case. An explanation may be sought furthermore, at least by parts, in a shell dependence of the intrinsic skin thickness as was advocated by Friedrich and Voegler (Fr 81, 82) and in particular for Cd by Wenz et al. (We 81). None of the explanations can be excluded at present.

In summary the analyses in this section have led to the following conclusions: Isotope shifts of proton magic or nearly proton magic elements have a very regular, parabolic shape and bear a much larger contribution from (probably) collective core polarization than offered from BE2 ($0^+ \rightarrow 2_1^+$) values alone. The same phenomenon is observed near closed neutron shells, as was mentioned in foregoing sections already. On the other hand, we repeat that the isotope shift is well described by the droplet model plus the traditional β_2-contribution whenever it connects rigid spherical with rigid deformed nuclei.

4.9. Isotope Shift of Very Light Nuclei

In light elements muonic spectra and electron scattering yield excellent, model-independent rms radii, but only very few

and not very precise measurements of isotope shifts have been reported for elements lighter than Ca (Ja 74, En 74). The situation is not better in optical spectroscopy except for Na. The reasons are obvious: (i) The field shift is becoming so small that experimental errors matter even for the most precise methods. (ii) The mass shift exceeds the field shift by orders of magnitude (about 10^2 for Na). Consequently the field effect can be traced only by tiny deviations of the total IS from the well defined A-dependence of the mass shift (eq.s (2.2, 2.3). This is possible, if a sufficently large number of isotopes has been measured which is the case for Na (Hu 78). Still the quantitative evaluation of the field shift and especially its scale depend strongly on the choice of the specific mass shift constant S. It has to be chosen such that the $\delta\langle r^2\rangle$ scale is compatible with some model prediction. Fig. 4.18 shows $\delta\langle r^2\rangle$ values for Na isotopes resulting from this type of evaluation (Hu 78) in comparison with deformed Hartree-Fock calculations (Ca 75). In the vicinity of A = 25 both curves agree very well. But the experiment does not confirm the sharp edges at A = 23 and 30 exhibited by the theoretical curve.

The example of Na proves that optical spectroscopy of light exotic nuclei can still produce fruitful results on their charge distribution, although the accuracy is limited much more by experimental and systematic errors than in heavier elements.

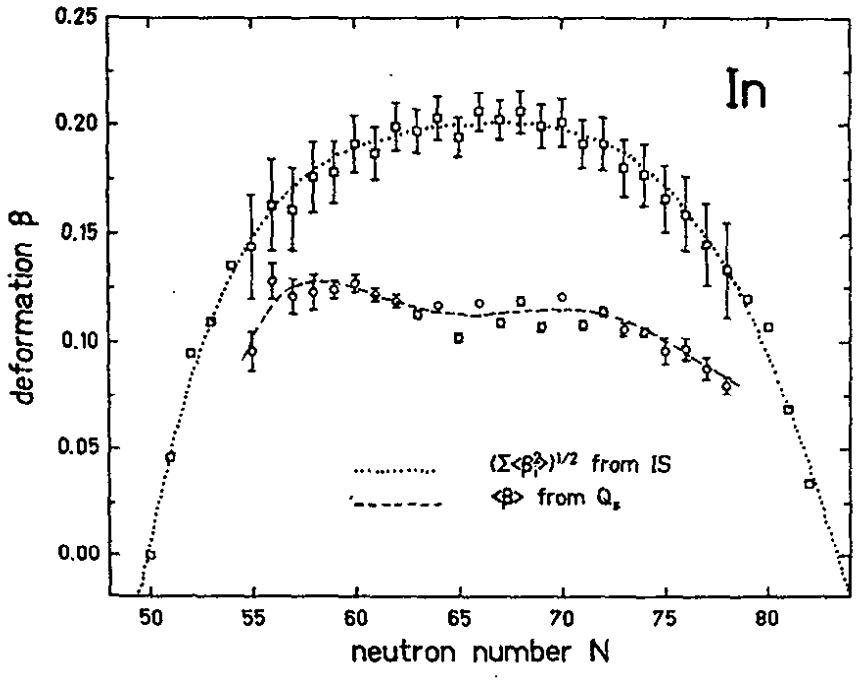

Fig. 4.17: $\langle\beta^2\rangle_{IS}^{1/2}$ of In isotopes in comparison with $\langle\beta\rangle_{Q_s}$ values. The error bars on $\langle\beta^2\rangle_{IS}^{1/2}$ increase towards the wings of the curve due to systematic scaling errors (Eb 87b).

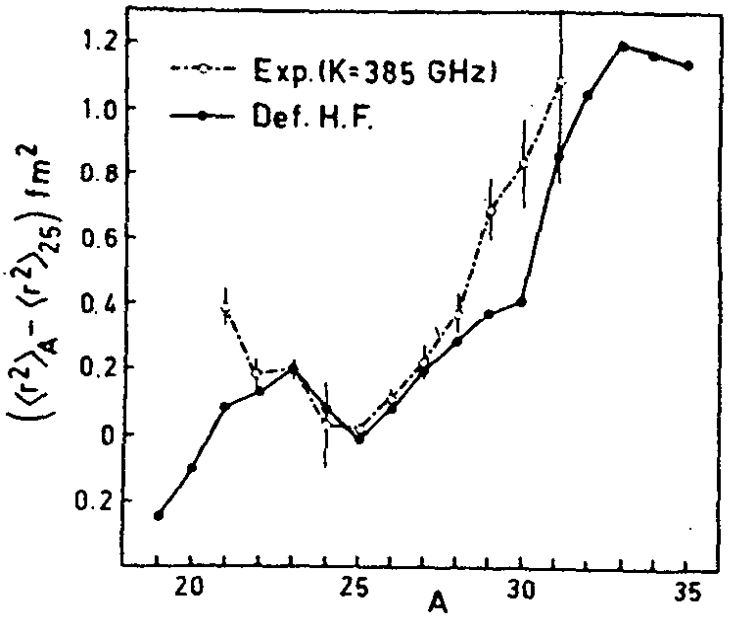

Fig. 4.18: Experimental $\delta\langle r^2\rangle^{A,25}$ values for a series of Na isotopes (Hu 78) in comparison with a deformed Hartree-Fock calculation (Ca 75). The total mass shift constant K = N + S was chosen to be 385 GHz.

4.10. Isotone and Isobar Shifts and the Question of Neutron Skin

The problem of the distribution of neutrons $\rho_n(r)$ in nuclei differing from that of protons $\rho_p(r)$ was already addressed in section 4.2. Only hadronic probes have direct access to the former, but electrons only to the latter. Still the neutron distribution can indirectly be felt by electrons through its retroaction on the proton distribution. That should be reflected, for instance, in differences between isotope and isotone shifts and in isobar shifts of the ms charge radius $\langle r^2 \rangle_p$. Isotone shifts between stable nuclei were shown in Fig. 4.14 already; they are limited to $\Delta Z = 2$ mostly. Since measurements of isotope shifts off stability have extended the knowledge of ms charge radii over large, compact regions of the nuclear chart, it is possible now to extract also long chains of isotone and isobar shifts from the data. So far this matter has not been explored systematically except for the example of the Cd-Sn region which has been connected towards lower Z to Rb and towards higher Z to Cs and Ba (Bu 87).

For evaluating isotone and isobar shifts one needs besides the optical isotope shifts an absolute $\langle r^2 \rangle$ value for at least one isotope in each chain as additional input parameter which serves as a link between the different elements. The latter are taken from muonic spectroscopy or electron scattering of stable nuclei. As an example the isotone shift at N = 66, i.e.

in the middle of the neutron shell, is shown in Fig. 4.19a. As in the case of isotope shift, the shell closure at Z = 50 is rendered by a distinct kink in the $\delta\langle r^2\rangle$ curve, which indicates a minimum of nuclear deformation. After substracting the contribution of deformation in an appropriate way the $\delta\langle r^2\rangle$ line is straightened and coincides with the droplet prediction (Fig. 4.19b).

An example of isobar shift is given for A = 118 in Fig. 4.20; it covers the range from $^{118}_{48}Cd^{70}$ to $^{118}_{55}Cs^{63}$ with 7 nucleons being exchanged. Corrected for contributions from deformation it also agrees with the prediction from the droplet model. Note that in a naive, homogeneously charged liquid drop model of radius

$$R_p = R_n = R_o = r_o A^{1/3} \qquad (4.28)$$

the isobar shift would vanish identically. Hence, it demonstrates in a very simple and clear manner the capacity of the droplet model to describe neutron and proton radii separately and correctly.

The connexion between isobar shift and ms neutron radii may be illustrated further by deriving a relation between $\delta\langle r^2\rangle_p$ and $\delta\langle r^2\rangle_n$ under the assumption that the ms nuclear matter radius

$$\langle r^2\rangle_m = \frac{Z}{A}\langle r^2\rangle_p + \frac{N}{A}\langle r^2\rangle_n \qquad (4.29)$$

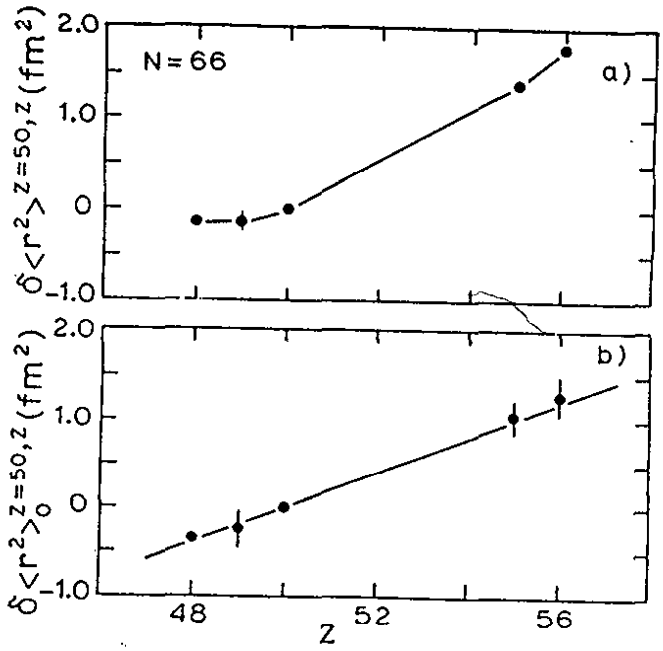

Fig. 4.19: a) $\delta\langle r^2\rangle^{Z,50}$ in the isotonic series N = 66 relative to the closed proton shell isotone $^{116}_{50}Sn$. The line connects the data points for guiding the eye.
b) Same as a), but corrected for the contribution of quadrupole deformation to $\langle r^2\rangle$ (Bu 87). The line indicates the prediction of the spherical droplet model.

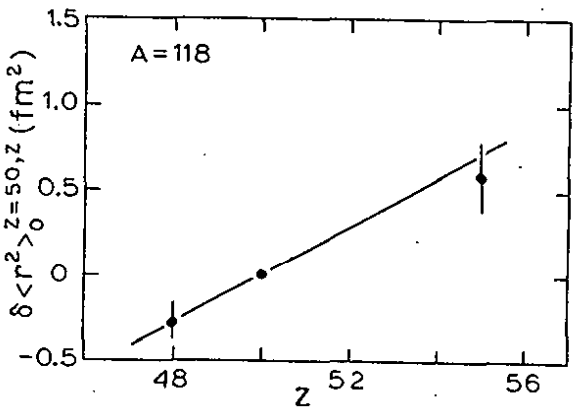

Fig. 4.20: $\delta\langle r^2\rangle$ in the isobaric series A = 118 corrected for quadrupole deformation (Bu 87). The prediction of the spherical droplet model is shown as solid line.

shall be constant in a chain of isobars. (This assumption is more flexible than eq. (4.28) but still implies essentially the incompressibility of nuclear matter.) With this constraint one finds from eq. (4.29) the relation

$$\delta\langle r^2\rangle_n^{N_1,N_o} = -\frac{Z_1}{N_1}\delta\langle r^2\rangle_p^{Z_1,Z_o} - \frac{A}{N_o N_1}(N_1-N_o)(\langle r^2\rangle_m^A - \langle r^2\rangle_p^{Z_o}) \qquad (4.30)$$

and hence to first order

$$\delta\langle r^2\rangle_n = -\frac{Z}{N}\,\delta\langle r^2\rangle_p \qquad (4.31)$$

which was sought for. For the case considered it follows from the data

$$\langle r^2\rangle_N\,(^{118}_{48}Cd^{70}) - \langle r^2\rangle_N\,(^{118}_{55}Cs^{63}) = 0.59\ \text{fm}^2. \qquad (4.32)$$

In terms of rms radii eq. (4.32) corresponds to a swelling of the neutron radius by $\delta\langle r^2\rangle_N^{1/2} = 0.063$ fm on cost of a shrinking of the charge radius by $\delta\langle r^2\rangle_Z^{1/2} = -0.092$ fm (Bu 87). Angeli et al. have performed systematic calculations of proton and neutron radii with a BCS Hartree-Fock code (An 80). Fig. 4.21 from their paper shows differences between neutron and proton rms radii in isotopic sequences from which on reads, e.g. $\delta\langle r^2\rangle_n^{1/2} - \delta\langle r^2\rangle_p^{1/2} = 0.12$ fm for the pair $^{118}_{48}Cd^{70}$, $^{118}_{52}Te^{66}$ with 4 nucleons being exchanged. Extrapolation of this number to the exchange of 7 nucleons rises it to 0.196 fm which is in fair agreement with the value of 0.155 fm estimated from the crude model made above.

4.11. Differential Isotope Shifts, Subshell Effects and Odd-Even Staggering

The experimental accuracy of measuring integral optical isotope shifts exceeds for all but light elements by far the present limits of their interpretation which are set by systematic errors in the evaluation of mass and field shift and by deficiencies of models of nuclear gross structure. It makes sense, therefore, to examine also differential shifts between neighbouring isotopes; by that means systematic errors are scaled down and even small local changes in the course of $\delta\langle r^2\rangle$ are accentuated sufficiently to stand out clearly.

4.11.1. Indications of Subshell Closures

This accentuation is illustrated by the sharply structured $\delta\langle r^2\rangle^{A,A-2}$ plot of Sn isotopes in Fig. 4.22 (An 86) in comparison to the smooth integral isotope shift, plotted in Fig. 4.15. The interpretation of such differential structures is not obvious. The authors have attributed the drop at N = 64, for instance, to a subshell closure, deviding the $d_{5/2}$ and $g_{7/2}$ from the $s_{1/2}$, $d_{3/2}$ and $h_{11/2}$ neutron orbits. The same correlation was observed in the isotones of Cd already before (We 81). Also in other regions of the nuclear chart the appearence of discontinuities in the differential isotope shift could be correlated to subshell closures. But the signature of these effects does not resemble the clear and unique one at major shell closures. So far an explicit explanation of what these structures actually mean is missing. Be that as it may, the Sn structure is repro-

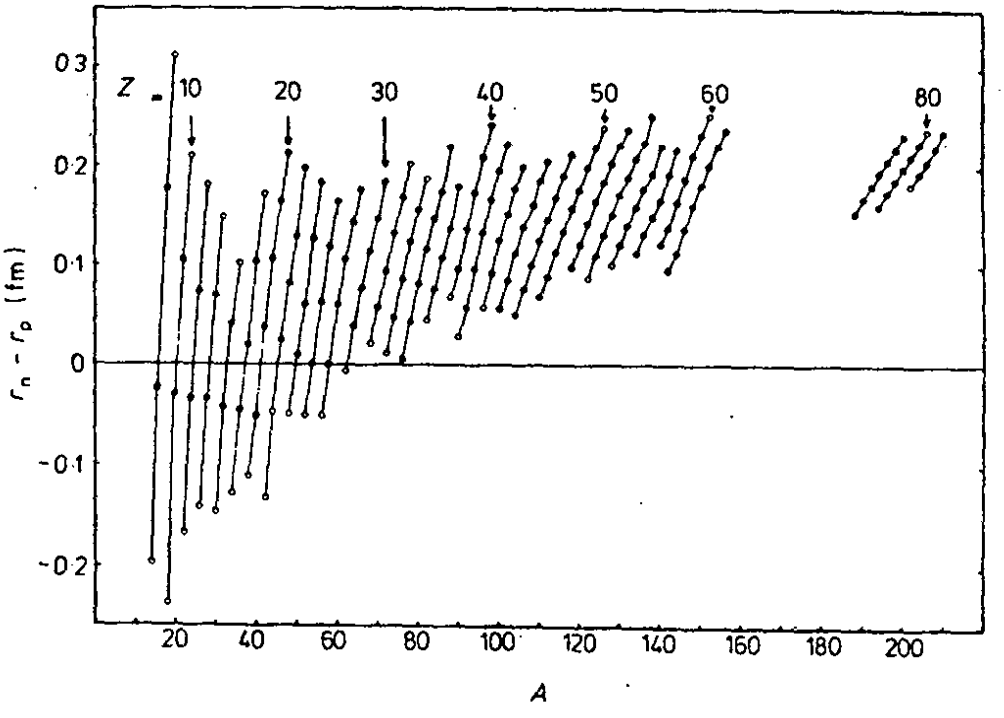

Fig. 4.21: Calculated differences between neutron and proton rms radii. Full circles correspond to stable nuclei, open circles indicate unstable ones (An 80).

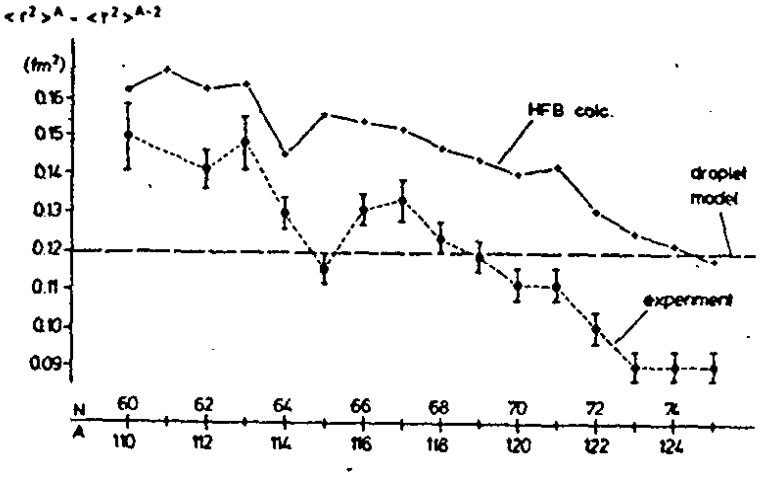

Fig. 4.22: Differential isotope shifts $\delta\langle r^2 \rangle^{A,A-2}$ of Sn (An 86) in comparison with theoretical results (Do 84).

duced qualitatively by a microscopic Hartree-Fock-Bogoljubov calculation, although the dip is shifted against the experimental one by one neutron number (Do 84).

4.11.2. Odd-Even Staggering and its Interpretation as Collective Effect

A famous differential effect is the odd-even staggering of nuclear radii. It is known since the early days of isotope shift measurements and has been observed in all regions of nuclei. With a few exceptions (see the next section) the effect exhibits a very regular signature, namely that $\langle r^2 \rangle$ of an odd-N nucleus is always smaller than the average of its even-N neighbours, which is expressed by the staggering parameter

$$\gamma^{(N)} = 2\, \delta\langle r^2 \rangle^{N,N-1} \,/\, \delta\langle r^2 \rangle^{N+1,N-1}\,, \quad (N = \text{odd}) \qquad (4.33)$$

being smaller one. The neutron-deficient isotopes of Xe, Cs and Ba in Fig. 4.5 exhibit an especially clear example of the regularity and persistence of this effect.

For a regular phenomenon usually a clearcut explanation is found; not so for odd-even staggering! At present, there is no quantitatively successful theory of odd-even staggering available. But qualitatively all explanations agree, that the effect is due to deformation and that $\langle \beta_2^2 \rangle$ should be smaller for an odd-N nucleus than for its even neighbour. One explanation on these lines was already met in section 4.9. within

the frame of the Zamick-Talmi model. The algebra of core polarization matrix elements led to a dependence on particle number in a (j^n) shell which included odd-even staggering. Inspection of eq. (4.25) which holds for even multipoles proves that the sign of the effect is given correctly.

In the frame of a boson picture one could argue naively that in the first place only the number of pairs of particles or holes counts for the deformation. This mechanism would automatically produce odd-even staggering in the right sense.

The standard explanation of odd-even staggering is given in terms of the pairing plus quadrupole model. Reehal and Sørensen formulated the theory and performed extensive calculations of staggering parameters in qualitative agreement with experiment (Re 71). Following their conception, the BCS mechanism scatters pairs in levels above the Fermi surface giving rise to an enlarged collective vibrational $ß_2$-amplitude of the zero point motion which contributes to $\langle r^2 \rangle$ via eq. (4.9). In odd nuclei these vibrations are reduced by blocking. The effect may also be visualized graphically from Fig. 4.23 showing the potential energy surface of an odd and an even nucleus in a schematic fashion. Both nuclei may fill the ground level in a deformed minimum created by shell corrections to the liquid drop energy. As already discussed in section 4.7. the residual pairing interaction is counteracting the shell corrections; thus it reduces the depth of the minimum which causes the collective wave function to spread out wider. Consequently the rms deformation shifts to a larger value due to its quadratic weight. In odd nuclei,

however, this effect is blocked (see also ref. (Ah 87)). It is interesting to note that the same picture is used to explain why spontaneous fission rates are slower in odd than in even nuclei (Bj 80).

The systematics of odd-even staggering which are available now show variations with the occupation number of a particular subshell. In the case of the $\nu i_{13/2}$ isomers in Hg, for instance, the effect is very strong for light isotopes ($\gamma \approx 0$ in ^{185}Hg) and vanishes for heavy ones ($\gamma \approx 1$ in ^{197}Hg) where the shell is full except for a single hole (St 79, Ul 86). A similar behaviour seems to be observed in the $\nu f_{7/2}$ shell of rare earths. The theoretical literature on the extensive new results of odd-even staggering obtained off stability is scarce. Zawischa has taken up the problem recently again; he included a cluster interaction between neutron and proton pairs in order to transfer the pairing effect of the neutrons which is the primary course of odd-even staggering to the charge distribution. He could reproduce experimental data from stable Mo, Cd and Ba isotopes with fair accuracy (Za 85).

4.12. Evidence for Octupole Shapes in the Ra-Region

An interesting new feature of nuclear structure has been the discovery in recent years that intrinsic reflection symmetry is spontaneously broken in the ground states of a group of heavy nuclei around ^{225}Ra. Nuclear spectroscopy has traced several characteristic signatures of this asymmetry, for instance: (i) almost degenerate doublets of same spin and opposite parity

in odd nuclei, (ii) I^p sequences of 0^+, 1^-, 2^+, 3^-, 4^+, ... in bands of even nuclei; (iii) unusually large E1-matrix elements in α and γ decay. Most theories ascribe the broken symmetry to an intrinsic octupole deformation of the matter distribution, some others to α clustering at the nuclear surface. Both explanations would also imply the existence of an intrinsic electric dipole moment, a priori in the latter case and a posteriori in the former case. The field is summarized e.g. in ref.s (Ha 85, Me 86).

4.12.1. Octupole Effects in the Isotope Shift

What can optical spectroscopy contribute to the question? Systematic measurements of spins, moments and isotope shifts have been performed recently along extended isotope chains of Rn, Fr and Ra (data and references given in Table 7.1) which cross the critical region of neutron numbers $130 \lesssim N \lesssim 140$. Fig. 4.24 shows the course of $\delta\langle r^2\rangle$ for Ra spanning the range $206 \leq A \leq 232$. There is a blank between ^{214}Ra and ^{220}Ra, since α decay lifetimes drop to the μs range in this region, too short to be separable with present on-line mass separation techniques. Nevertheless, one recognizes the characteristic kink at the magic neutron number $N = 126$ by extrapolation from heavier masses.

One may ask whether it seems possible to identify an octupole term $\langle\beta_3^2\rangle$ from an analysis of the integral isotope shift $\delta\langle r^2\rangle^{N,126}$ by eq. (4.10) under the assumption $\langle\beta_i^2\rangle^{N=126} \approx 0$. A β_3 value in the range of 0.1 which is calculated by the majo-

Fig. 4.23: Schematic drawing of the potential energy of an odd and an even nucleus as a function of quadrupole deformation. The minima of PE and the rms deformations of the ground level are indicated.

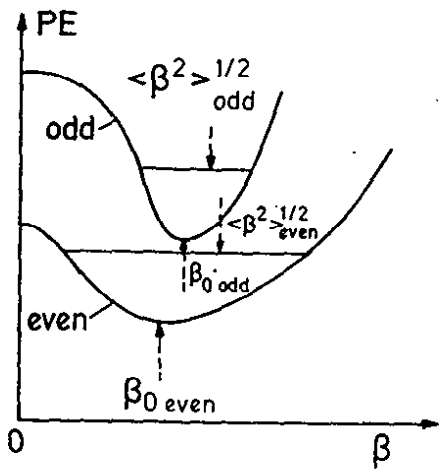

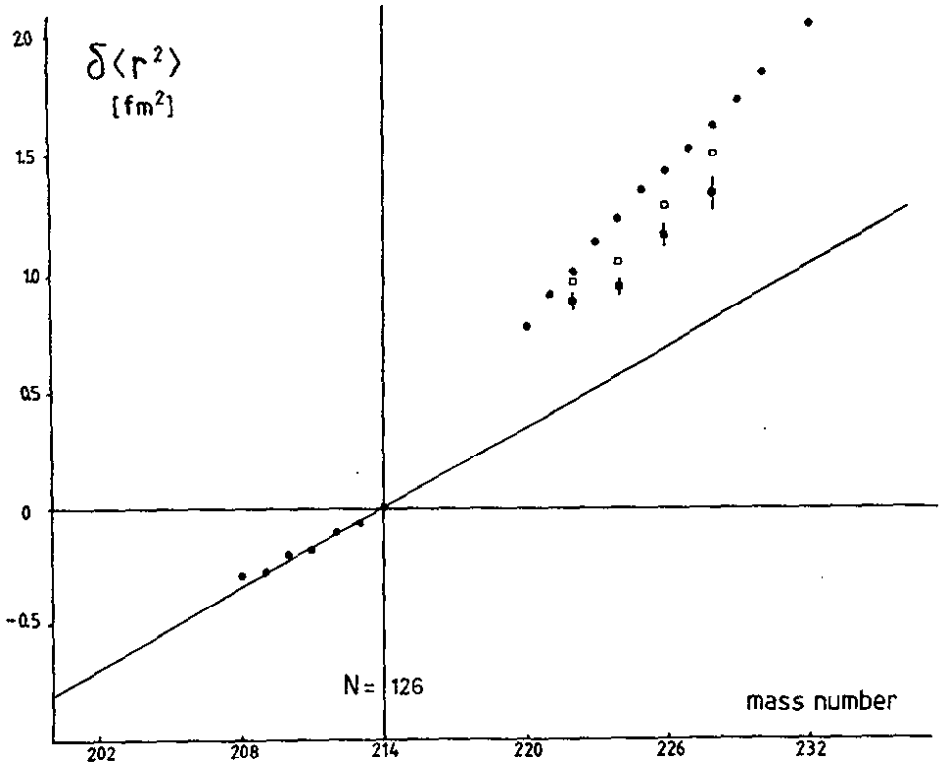

Fig. 4.24: Plot of $\delta\langle r^2\rangle^{A,214}$ (full dots) for Ra (Ah 87) in comparison with the revised steeper droplet line (Mö 84). The shape effect as calculated from experimental BE2 values is added to the latter one for some of the heavier isotopes (full squares). A further correction with theoretical β_4 values (Na 84) leads to the open squares.

rity of theories (see e.g. ref. (Le 84b)) would have an effect of 0.13 fm^2 on the ms radius. Competing with a total shift of about 1.5 fm^2 over that range, the effect is actually too small in view of the systematic errors in the evaluation of the field shift factor F (eq. (2.13)) and of the volume effect $\delta\langle r^2\rangle_s$ (Ah 87). Alternatively one could start from the side of the heavy masses, for instance from ^{229}Ra, where octupole deformation should have vanished already. Q_s and BE2 values are known in this region in order to correct $\delta\langle r^2\rangle$ for quadrupole deformation. This procedure seems to be safe at the heavy end of the chain since deformation is static there as has been proved by comparing Q_s to Q_o by the strong coupling rule (2.26.) (Ah 83, Ah 87). But for smaller N the static character of deformation gets lost which inhibits a safe determination of $\langle\beta_2^2\rangle$ from BE2 or Q_s values, as has been pointed out in preceding sections. Moreover, a β_4-deformation has to be taken into account. In summary isotope shift analysis is overcharged by the task of determining the size of the octupole deformation reliably.

But the isotope shift reveals a very valuable qualitative feature of the presence of octupole deformation. This concerns the irregular, inverted odd-even staggering observed for ^{221,223,225}Ra. Their ms radius is bigger than the average of their even neighbours indicating a larger ms deformation. The inversion of the staggering is seen more clearly in the derivative of the integral isotope shift, which is plotted in Fig. 4.25 as $\delta\langle r^2\rangle^{N,N-1}$. The slope always staggers from one isotope to the

next but its sense is inverted in the above mentioned region. There the odd ones are up and the even ones down in contrast to the regular staggering below N = 126. It is very conspicious, moreover, that the inverted staggering is not confined to Ra but repeated also in the isotones of Rn (Bo 87) and Fr (Co 87) as seen from the figure.

The observation of the inverted staggering came unexpected; but it supports calculations by Chasman (Ch 80), and Leander and Sheline (Le 84b) stating that octupole deformation should be more pronounced in odd than in even nuclei. In this context it is worth reminding also that the core polarization model by Zamick and Talmi (see section 4.9.) predicted the regular odd-even staggering for even multipoles and inverted ones in case of odd multipoles. Although the theories to be compared here do not have very much in common, their agreement in that point is not necessarily accidental.

It was already mentioned that octupole deformation can also bring about an intrinsic electric dipole moment. The order of magnitude observed experimentally is p = 1 e·fm. Its effect on the ms radius may be estimated as follows: The dipole may be created by moving an amount of charge $q = p/R_o$ from its quadratically weighted average position at $\langle r^2 \rangle^{1/2} = \sqrt{(3/5)\ R_o^2}$ to the surface at R_o. Then $\langle r^2 \rangle$ increases by

$$\delta\langle r^2 \rangle_{e.D.} = \frac{q}{Z\ e} (R_o^2 - 3/5\ R_o^2) = \frac{2}{5} \frac{p}{Z\ e} R_o. \qquad (4.34)$$

The effect amounts to 0.033 fm^2 in Ra for p as given above; it is small but not completely negligible.

4.12.2. Single Particle States of Octupole Deformed Nuclei

Crucial information on octupole shapes are also provided by single particle properties like spin and magnetic moment. Before explaining these details it might be advisable to briefly resume a few basic relations between geometry and dynamics in an asymmetric potential. Per definition the nuclear potential energy surface must be symmetric in the collective octupole coordinate β_3, since change of sign is equivalent to a rotation of the nucleus by 180° (see Fig. 4.26). If the central barrier at $\beta_3 = 0$ is high enough, the collective wave function localizes around the two potential minima at $\pm\beta_{3min}$ and forms a symmetric (positive parity) and an antisymmetric (negative parity) state with respect to reflexion. These two states form an (almost) degenerate doublet of opposite parity which is the characteristic spectroscopic feature of asymmetric shapes, as is well known from molecular physics. The famous maser transition in NH_3, for instance, is just this doublet transition. If the doublet splitting is very small as compared to other excitations, then one can speak of a "stable" octupole deformation; because the time for which the collective wave function can be localized at one side of the barrier by superposition of the doublet states is given by the reciprocal of the transition energy. This doublet structure is fairly well established in a number of cases in the Ra region.

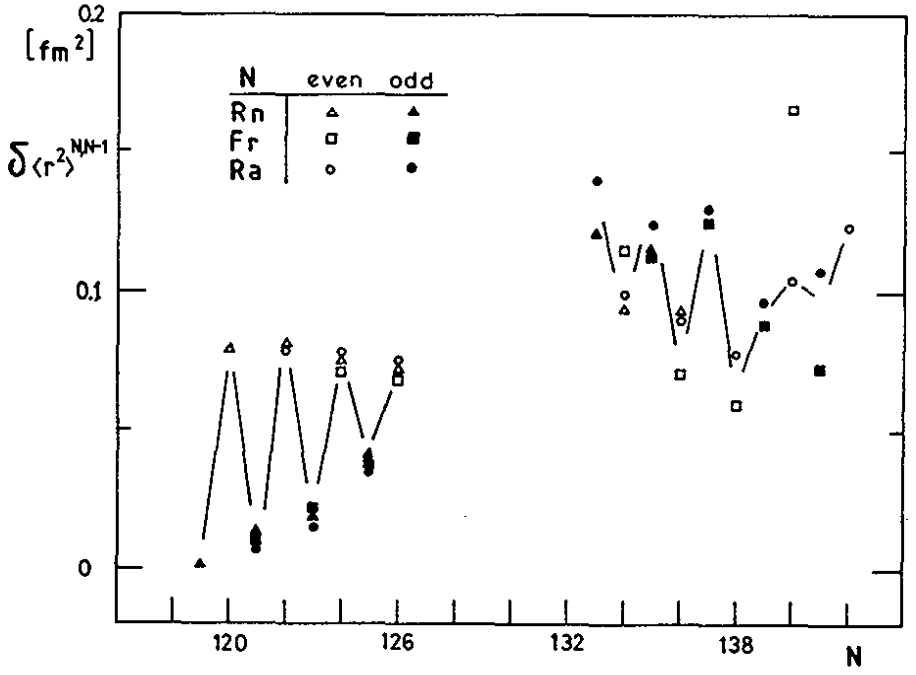

Fig. 4.25: Differential isotope shift $\delta\langle r^2\rangle^{N,N-1}$ for Rn, Fr and Ra isotopes showing regular odd-even staggering below N = 126 and the inverted for neutron numbers N = 133, 135, 137 (Ah 87).

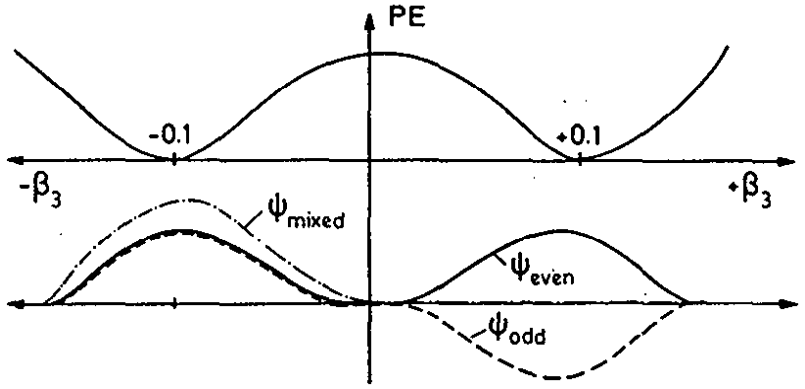

Fig. 4.26: Schematic drawing of an octupole potential energy surface (upper part). The symmetric and the anti-symmetric collective wave function as well as their superposition are shown on the lower part.

In an octupole potential single particle levels of opposite intrinsic parity will get mixed, especially degenerated ones. Fig. 4.27a shows Nilsson levels for Ra as a function of the quadrupole deformation β_2 where the octupole deformation has been kept zero (Le 84b). One sees a number of level crossings of states with same spin but opposite parity. After switching on octupole deformation to $\beta_3 = 0.08$ (Fig. 4.27b), these crossings are removed by forming new single particle states, which now have mixed intrinsic parity. In fact, these level crossings are the ones, which trigger the breakdown from quadrupole to octupole symmetry by residual octupole interaction with the core (reviewed e.g. in ref. (Ra 78)). It has been shown (Re 84) that this mechanism is the same as the one which breaks the symmetry of molecular configurations, namely the Jahn-Teller effect (Ja 37).

For comparison with experiment it is important that the reshuffled level scheme shows another spin sequence as a function of neutron number than for pure quadrupole deformation. For neutron numbers $133 \leq N \leq 141$ spins 1/2, 3/2, 3/2, 5/2, 5/2 appear consecutively at the Fermi surface in the quadrupole case, whereas calculations including octupole reproduce the correct experimental sequence 5/2, 3/2, 1/2, 3/2, 5/2. (β_2 increases in this range from 0.15 to 0.2).

Moreover, the magnetic moment is very sensitive to the degree of intrinsic parity mixing in the hybridized single particle wave function. This is particularly evident, when states with opposite nucleon spin projection like $|n, n_z, \Lambda\downarrow\rangle$ and $|n+1, n_z+1, \Lambda-1\uparrow\rangle$ mix, because the nucleon g-factor cancels in taking

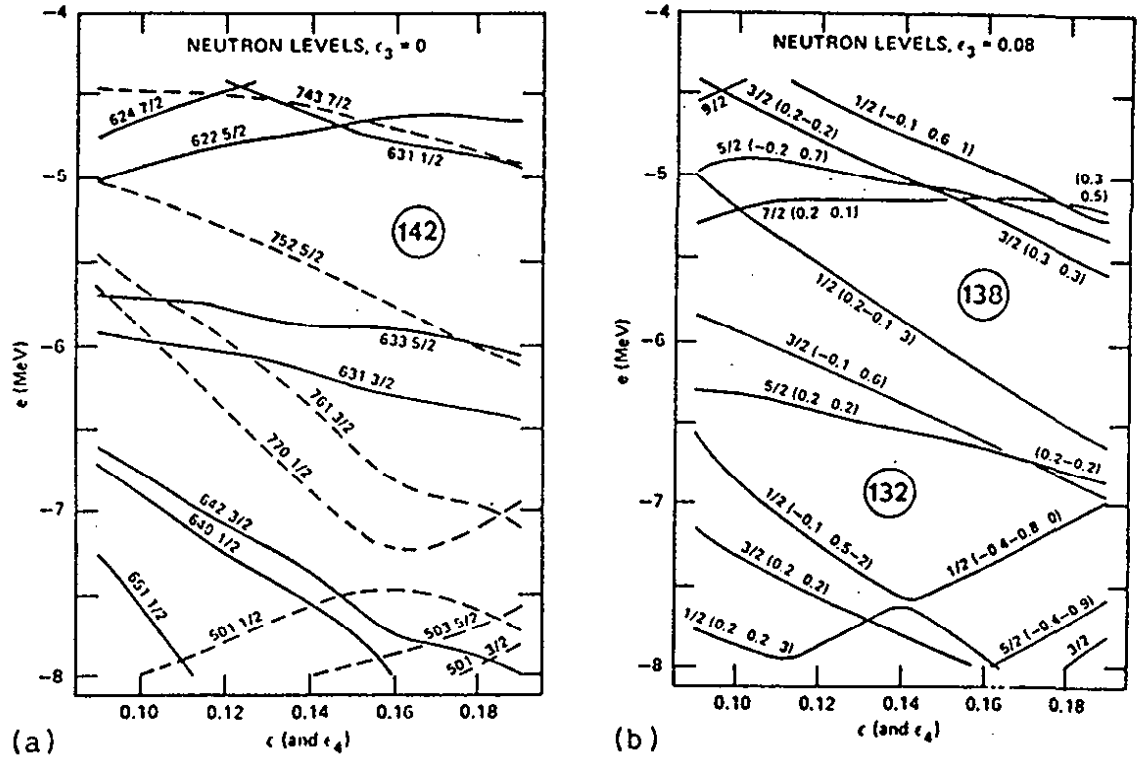

Fig. 4.27: Nilsson diagram of neutron levels in Ra as a function of β_2; a) without octupole degree of freedom ($\beta_3 = 0$), b) β_3 fixed to 0.08 (Le 84b).

the sum. Table 4.1, taken from ref. (Le 84b), shows in comparison with experiment magnetic moments calculated with and without octupole deformation. The table proves that only in the octupole case satisfactory agreement between theory and experiment can be achieved (compare also ref. (Ra 83)).

Table 4.1: Spins and magnetic moments of some Ra-isotopes in comparison with theoretical calculations with and without octupole degree of freedom (Le 84b).

Nucleus	I^p_{exp}	μ_{exp}(n.m.)	I^p_{th}	μ_{th}(n.m.)	β_3	Dominant Configuration
^{221}Ra	5/2	-0.18	$5/2^+$	-0.13	0.1	[642]x[752]5/2
			$5/2^+$	0.39	0	[633]5/2
^{223}Ra	3/2	0.27	$3/2^+$	0.50	0.1	[642]3/2
			$3/2^+$	0.03	0	[631]3/2
			$3/2^-$	-0.06	0	[761]3/2
^{225}Ra	$1/2^+$	-0.73	$1/2^+$	-0.75	0.1	[640]1/2
			-	-	0	-
^{227}Ra	$3/2^+$	-0.40	$3/2^+$	-0.41	0.08	[631]3/2
			$3/2^+$	-0.06	0	[631]3/2
^{229}Ra	5/2	0.50	$5/2^+$	0.38	0.04	[633]5/2
			$5/2^+$	0.61	0	[633]5/2
			$5/2^-$	-0.29	0	[752]5/2

5. CONCLUDING REMARKS

What has been achieved by optical spectroscopy far off stability and what is still to be done? Charge radii, spins and moments have been measured along extended isotopic chains of about 20 elements covering about 400 nuclear ground states and isomers. Seen from a numerical standpoint of view we are not jet midway. Experimental methods are prepared for the rest of it.

But will more numbers give new essential insights in nuclear structure and stimulate theory or will they just fill tables like a collection of precious stones an amateurs shelves? The truth is that the complexity of nuclear structure can not be understood and analyzed adequately without rather detailed and complete experimental information. Critical phenomena like shape transitions are one example, proving the statement. The charge radii of transitional nuclei show suprisingly large contributions from core polarization; but this could be seen only from analyzing the isotope shift along extended chains which cover major parts of a shell. The systematic IS and Q_s measurements over compact regions have also corroborated the traditional nuclear gross models for nuclei with stabilized spherical or deformed shells.

Generally speaking optical spectroscopy and nuclear spectroscopy are playing rather complimentary roles in studying the fundamental questions of nuclear size, shape and symmetry, the former on the side of the geometry, the latter on the side of the dynamics.

On the other side of the medal one finds a number of open questions in atomic physics: how to evaluate precisely the electric field gradient, the specific mass and the field shift in electronic spectra. In many body theory of electronic shells these problems have certainly a right and weight of their own. The present uncertainties of about 10 %, or even more in some cases, are impeding but by no means preventing the interpretation of the results in nuclear physics. Progress in these atomic physics questions may be expected soon from the theoretical side but also from the experimental one through calibration measurements by muonic spectra.

On-line laser spectroscopy in combination with sophisticated isotope production and separation, and signal detection techniques will push the frontiers to higher sensitivity and enable measurements on refractory elements. The new techniques will enrich the scope of experiments at mass separators on line with proton and heavy ion accelerators. But also on line facilities at high current machines could further boost the field.

6. ACKNOWLEDGEMENT

Having finished this treatise on a meeting point of quantum optics, atomic and nuclear physics the author feels very grateful to his collaborators and colleagues J. Bonn, G. Huber, H.-J. Kluge and R. Neugart with whom he had the pleasure to work in this field over the years and whose ideas and results have merged into this article. He acknowledges the most valuable help of Mrs. A. Hermanni and K. Wendt who arranged the figures, references and the table of results. Sincere thanks also to Mrs. E. Stuck for her diligent typing of the manuscript.

7. Appendix

TABLE 7.1: NUCLEAR MOMENTS AND CHARGE RADII OF LONG ISOTOPIC CHAINS

Elements included: Status: 11/86

Abbreviation	Element	Proton Number Z
Li	Lithium	3
Na	Sodium	11
K	Potassium	19
Ca	Calcium	20
Rb	Rubidium	37
Sr	Strontium	38
Cd	Cadmium	48
In	Indium	49
Sn	Tin	50
Cs	Caesium	55
Ba	Barium	56
Eu	Europium	63
Er	Erbium	68
Yb	Ytterbium	70
Au	Gold	79
Hg	Mercury	80
Tl	Thallium	81
Pb	Lead	82
Rn	Radon	86
Fr	Francium	87
Ra	Radium	88

Legend:

The table compiles spins (I), magnetic moments (μ_I), spectroscopic quadrupole moments (Q_s) and changes of ms charge radii $\delta\langle r^2\rangle$ measured in extended chains of isotopes by off stability techniques of optical spectroscopy.

Explicit reference is usually given to these experiments only. Other data are taken from (Le 78). Comments are given with regards to the experimental method used, the optical transitions investigated, and the evaluation of data. In most cases μ_I is calculated from the ratio of A-factors through a known and diamagnetically corrected μ_I of a reference isotope and without correction for hfs anomaly, using the equation

$$\mu_I^x = \mu_I^{ref} \left(A^x I^x / A^{ref} I^{ref} \right).$$

Regarding Q_s it is mentioned whether a Sternheimer correction is applied or not.

$\delta\langle r^2 \rangle$ values: The method used for the evaluation of the field shift factor F and its value are given in each individual case including reference. Also given is the specific mass shift constant S used in the calculation.

In cases of competing data the most precise value published was chosen without averaging or further reanalysis, the corresponding reference is printed without brackets, whereas bracketed references refer to the other competing measurements. In view of the different evaluation methods used, this was felt to be the only viable procedure. Errors are given as published, mostly they do not include systematic uncertainties.

Element: Lithium Z = 3

A	$\tau_{1/2}$	I	μ_I n.m.	Q_m b.	$\delta\langle r^2\rangle^{A,6}$ fm^2	Ref. μ_I , Q_m , $\delta\langle r^2\rangle$
6	stable	1	0.8220467(6)	-0.000644(7)		1 , 2
7	stable	3/2	3.256424(2)	-0.0366(3)		1 , 3
8	0.84s	2	1.65335(35)	0.024(2)		4 , 5
9	178.3ms	3/2	3.4391(6)	0.032(6)		6 , 6
11	8.5ms	3/2	3.73(13)			7

References: 1. (Be 74), 2. (Wh 64), 3. (Gr 71), 4. (Ha 73)
5. (Mi 75), 6. (Co 83), 7. (Ar 86)

Comments:

Exp. Method: 1.-3.: nuclear magnetic resonance
4.-6.: radiation detected nuclear magnetic resonance
7.: β-RADOP

Transitions: 7.: LiI D1 and D2 line (670 nm)

μ_I-eval.: reference isotope ^{6}Li from 1.

Q_m-eval.: direct measurements

$\delta\langle r^2\rangle$-eval.: not given, only possible under extremly restrictive assumptions about the dominating mass-shift

---

Element: Sodium Z = 11

A	$\tau_{1/2}$	I	μ_I n.m.	Q_s b.	$\delta\langle r^2\rangle^{A,23}$ fm²	Ref. μ_I	Ref. Q_s	Ref. $\delta\langle r^2\rangle$
20	446.ms	2	0.3694(2)		-0.13(7)	5		2(1)
21	22.5s	3/2	2.38612(10)	0.050(37)	0.12(5)	1	2	2(1)
22	2.60y	3	1.746(3)		-0.05(4)	1		2(1)
23	stable	3/2	2.217520(2)	0.101(8)	0	3		4
24	15.02h	4	1.6902(5)		-0.12(4)	1		2(1)
25	60.0s	5/2	3.683(4)	-0.095(50)	-0.10(3)	1	2	2(1)
26	1.07s	3	2.851(2)	-0.079(54)	-0.005(18)	1	2	2(1)
27	290ms	5/2	3.895(5)	-0.058(54)	0.12(4)	1	2	2(1)
28	30.5ms	1	2.426(3)	-0.017(37)	0.28(5)	1	2	2(1)
29	43.ms	3/2	2.449(8)	0.025(54)	0.60(8)	1	2	2(1)
30	53.ms	2	2.083(10)		0.76(12)	1		2(1)
31	17.ms	3/2	2.283(38)		1.09(7)	1		2(1)

References: 1. (Hu 78) and references therein, 2. (To 82), 3. (Be 74), 4. (Le 78), 5. (Sc 75)

Comments:

Exp. method: 1.-2.: LIOP and laser rf double resonance
5.: RADOP

Transitions: 1.-2.: NaI D1 and D2 line

μ_I-eval.: reference isotope ^{23}Na

Q_s-eval.: HS-calc. from (Ro 72)

$\delta\langle r^2\rangle$-eval.: semi-emp. calc. F=-47.MHz.fm²
N+S=385.5GHz as disc. in 2.
$\delta\langle r^2\rangle$ values extremely sensitive to S !

Element: Potassium Z = 19

A	$\tau_{1/2}$	I	μ_I n.m.	Q_m b.	$\delta\langle r^2\rangle^{A,39}$ fm²	Ref. μ_I , Q_m , $\delta\langle r^2\rangle$
36	342.ms	2	±0.548(1)			1
37	1.226s	3/2	0.20321(6)			4
38	7.63m	3	1.371(6)		-0.058(41)	3 , 2
39	stable	3/2	0.3914658(4)	0.049(4)	0	3 , 3
40	stable	4	-1.2982(4)		0.0222(20)	3 , , 2
41	stable	3/2	0.2148699(2)	-0.067(8)	0.117(6)	3 , 3 , 2
42	12.36h	2	-1.1425(6)	0.060(5)	0.116(15)	3 , 3 , 2
43	22.3h	3/2	0.1633(8)		0.143(9)	2 , , 2
44	22.1m	2	-0.856(4)		0.148(11)	2 , , 2
45	17.3m	3/2	0.1734(8)		0.176(13)	2 , , 2
46	107.s	2	-1.051(6)		0.143(12)	2 , , 2
47	17.5s	1/2	1.933(9)		0.126(13)	2 , , 2

References: 1. (Sc 75), 2. (To 82b), 3. (Le 78), 4.(Kö 69)

Comments:

Exp. Method: 2.: Atomic beam laser spectroscopy (LIOP)
1.+4.: RADOP

Transitions: 1.-2.: KI D1 and D2 line

μ_I-eval.: reference isotope ^{39}K

Q_m-eval.: see 3. and references therein

$\delta\langle r^2\rangle$-eval.: semi-emp.-calc., F=-128MHz/fm²
S=200(4)GHz from muonic x-rays acc. to 2.

Element: Calcium Z = 20

A	$\tau_{1/2}$	I	μ_I n.m.	Q_s b.	$\delta\langle r^2\rangle^{A,40}$ fm^2	Ref. μ_I	Ref. Q_s	Ref. $\delta\langle r^2\rangle$
39	0.86s	3/2	1.02168(12)			4		
40	stable	0			0			
41	1×10^5y	7/2	-1.59478(1)	-0.062(12)	0.0012(25)	4	2	2-3
42	stable	0			0.2209(60)			1-3
43	stable	7/2	-1.31726(6)	-0.040(8)	0.1221(45)	4	2	1-3
44	stable	0			0.2908(75)			1-3
45	165.d	7/2	-1.316(16)	0.043(9)	0.1272(89)	3	2	2-3
46	stable	0			0.1290(63)			1-3
47	4.536d	7/2	-1.380(24)		0.007(10)	3		2-3
48	stable	0			0.0032(67)			1-3

References: 1. (Br 78), 2. (Be 80), 3. (An 82), 4. (Le 78)

Comments:

Exp. Method: 1.+3. Atomic beam laser fluorescence spectroscopy
2. Classical atomic beam spectroscopy

Transitions: 1.-3.: CaI 4s $^1S_0$-4s4p$^{1,3}P_1$ (422.7nm and 657.3nm)

μ_I-eval.: reference isotope ^{43}Ca

Q_s-eval.: semi-emp. calc. from fs in 2., Sternheimer corrected

$\delta\langle r^2\rangle$-eval.: weighted mean values from 1.-3.,
calibrated by muonic X-ray isotope shift acc. to (He 85b)

Element: Rubidium Z = 37

A	$\tau_{1/2}$	I	μ_I n.m.	Q_s b.	$\delta\langle r^2\rangle^{A,87}$ fm^2	Ref. μ_I , Q_s , $\delta\langle r^2\rangle$
76	39.1s	1	-0.376(9)	0.38(15)	0.220(27)	2 , 2 , 2
77	3.70m	3/2	0.6568(41)	0.695(32)	0.2831(69)	2 , 2 , 2
78	17.66m	0			0.3060(23)	2
78m	5.74m	4	2.5485(21)	0.814(39)	0.1912(26)	2 , 2 , 2
79	22.9m	5/2	3.3579(12)	-0.098(22)	0.2249(23)	2 , 2 , 2
80	30.34s	1	-0.0834(3)	0.348(20)	0.2166(68)	3 , 2 , 2
81	4.58h	3/2	2.0595(14)	0.398(23)	0.1698(22)	2 , 2 , 2
81m	32.m	9/2	5.5980(17)	-0.743(57)	0.1398(22)	2 , 2 , 2
82	1.25m	1	0.5536(54)	0.190(72)	0.1322(65)	2 , 2 , 2
82m	6.2h	5	1.6434(12)	1.01(12)	0.1319(58)	3 , 2 , 2
83	86.2d	5/2	1.4249(8)	0.196(22)	0.0512(15)	2 , 2 , 2
84	32.87d	2	-1.3246(16)	-0.015(35)	0.0078(32)	2 , 2 , 2
84m	20.49m	6	0.220(15)	0.57(27)	0.004(16)	2 , 2 , 2
85	stable	5/2	1.3533505(9)	0.274(2)	0.0355(22)	3 , 3 , 2(1)
86	18.65d	2	-1.6977(16)	0.193(32)	0.0271(31)	2 , 2 , 2
86m	1.018m	6	1.8150(10)	0.369(95)	0.0060(35)	2 , 2 , 2
87	stable	3/2	2.751816(2)	0.127(1)	0	3 , 3
88	17.8m	2	0.5117(26)	-0.012(96)	0.1364(78)	2 , 2 , 2
89	15.2m	3/2	2.3836(7)	0.144(26)	0.3051(31)	2(1),2(1),2(1)
90	153.s	0			0.4289(80)	2(1)
90m	4.26m	3	1.61598(64)	0.204(45)	0.4149(31)	2 , 2 , 2(1)
91	58.4s	3/2	2.1815(15)	0.154(26)	0.5580(35)	2(1),2(1),2(1)
92	4.50s	0			0.6963(80)	2(1)
93	5.85s	5/2	1.4095(16)	0.177(40)	0.8130(32)	2(1),2(1),2
94	2.70s	3	1.4984(18)	0.163(50)	0.9167(35)	2 , 2 , 2
95	0.38s	5/2	1.3336(34)	0.211(65)	1.0781(56)	2 , 2 , 2
96	0.20s	2	1.4658(17)	0.246(56)	1.1637(74)	2 , 2 , 2
97	0.17s	3/2	1.8410(21)	0.581(44)	1.7391(62)	2 , 2 , 2
98	0.11s	(0)			1.821(15)	2 , 2 , 2

References: 1. (Kl 79b), 2. (Th 81), 3. (Le 78)

Comments:

Exp. Method: 1. Standard collinear fast beam laser spectroscopy
2. Atomic beam laser spectroscopy (LIOP)

Transitions: 1.: RbI D2' line (420.3nm)
2.: RbI D2 line (780.0nm)

μ_I-eval.: reference isotopes ^{87}Rb

Q_s-eval.: HS-calc. from (Ro 72)
Sternheimer-correction applied

$\delta\langle r^2\rangle$-eval.: semi-emp. approach, F_{78o}=-650MHz/fm^2,
S_{78o}=0Ghz

Element: Strontium Z = 38

A	$\tau_{1/2}$	I	μ_I n.m.	Q_s b.	$\delta\langle r^2\rangle^{A,88}$ fm^2	Ref. μ_I , Q_s , $\delta\langle r^2\rangle$
78	30.6m	1			0.237(8)	2
79	2.25m	3/2			0.260(6)	2
80	106.3m	0			0.249(4)	2(3)
81	22.2m	1/2			0.238(4)	2(3)
82	25.6d	0			0.182(4)	2(3)
83	32.4h	7/2			0.163(4)	2(3)
84	stable	0			0.110(2)	1(2,3)
85	64.84d	9/2				(3)
86	stable	0			0.047(2)	1(2,3)
87	stable	9/2	-1.093602(1)	0.15(6)	0.006(2)	4 , 4 , 1(2,3,5)
88	stable	0			0.	
89	50.55d	5/2			0.147(8)	1(2,3)
90	28.6y	0			0.318(3)	1(2,3,5)

References: 1. (Bu 85), 2. (Ea 87), 3. (An 86), 4. (Le 78), 5. (He 61)

Comments:

Exp. Method: 1.+3. Atomic beam laser fluorescence spectroscopy
2. Coll. fast beam laser coincidence spectroscopy (FACS)
5. Classical high resolution spectroscopy

Transitions: 1.+2.: $5s^2\ ^1S_0$-$5s5p\ ^1P_1$ (460.7nm)
3.: $5s^2\ ^1S_0$-$5s6p\ ^1P_1$ (293.2nm)

μ_I-eval.: not evaluated as hfs unresolved

Q_s-eval.: not evaluated as hfs unresolved

$\delta\langle r^2\rangle$-eval.: semi-emp. approach from (Be 84d),
F_{460}=-896(130)MHz/fm^2, S_{470}=-0.12(8)N

Element: Cadmium Z = 48

A	$\tau_{1/2}$	I	μ_I n.m.	Q_s b.	$\delta\langle r^2\rangle^{A,114}$ fm^2	Ref. μ_I	Ref. Q_s	Ref. $\delta\langle r^2\rangle$
102	5.5m	0			-0.982(43)			1
103	7.3m	5/2	-0.81(3)	-0.79(66)	-0.876(41)	1	1	1
104	58.m	0			-0.745(47)			1
105	56.0m	5/2	-0.7393(2)	0.43(4)	-0.673(34)	1	1	1
106	stable	0			-0.5345(2)			1
107	6.50h	5/2	-0.615055(1)	0.68(7)	-0.481(29)	2	2	1
108	stable	0			-0.3920(2)			1
109	453d	5/2	-0.827846(2)	0.69(7)	-0.377(40)	2	2	1
110	stable	0			-0.2555(2)			1
111	stable	1/2	-0.5948856(9)		-0.2348(2)	2		1
111m	48.6m	11/2	-1.1051(4)	-0.85(9)	-0.246(100)	2	2	1
112	stable	0			-0.1206(220)			1
113	stable	1/2	0.6223005(9)		-0.0989(2)	2		1
113m	14.y	11/2	1.087783(2)	-.71(7)	-0.100(68)	2	2	1
114	stable	0			0			
115	53.4h	1/2	-0.648425(1)		0.023(45)	2		1
115m	44.8d	11/2	-1.041034(2)	-.54(5)	0.030(12)	2	2	1
116	stable	0			0.0941(2)			1
118	50.3m	0			0.125(22)			1
120	50.8s	0			0.169(42)			1

References: 1. (Bu 87), 2. (Le 78)

Exp. Method: Cell laser spectroscopy

Transitions: 1.: CdI $5s^2\ {}^1S_0$-$5s5p\ {}^3P_1$ (326.1nm)

μ_I-eval.: reference isotope ^{109}Cd

Q_s-eval.: see reference 2.

$\delta\langle r^2\rangle$-eval.: see the extensive discussion in 1.
F_{326}=3.91(46)GHz/fm^2, S=376(230)GHz

Element: Indium Z = 49

A	$\tau_{1/2}$	I	μ_x n.m.	Q_s b.	$\delta\langle r^2\rangle^{A,115}$ fm^2	Ref. μ_x	Ref. Q_s	Ref. $\delta\langle r^2\rangle$
104	1.7m	(5)	4.435(22)	0.659(106)	-0.842(15)	4	4	4
105	4.9m	9/2	5.675(5)	0.829(50)	-0.733(14)	2	2	2
106	6.2m	7	4.916(7)	0.972(61)	-0.678(12)	2	2	2
107	32.4m	9/2	5.585(8)	0.807(52)	-0.575(10)	1	1	1
108	58.m	7	4.561(3)	1.005(7)	-0.509(5)	3	3	3
108	40.m	2	4.935(5)	0.467(14)	-0.501(5)	3	3	3
109	4.2h	9/2	5.538(4)	0.841(27)	-0.410(7)	1	1	1
110	4.9h	7	4.713(8)	1.000(22)	-0.361(8)	1	1	1
111	2.83d	9/2	5.503(7)	0.804(22)	-0.262(5)	1	1	1
112	20.9m	4	5.277(5)	0.714(10)	-0.218(6)	4	4	4
112	14.4m	8	3.080(32)	-0.093(6)		4	4	
113	stable	9/2	5.5289(2)	0.799	-0.1280(3)	5	4	4
113	99.5m	1/2	-0.21074(2)			5		
114	49.51d	5	4.653(5)	0.739(12)	-0.087(2)	5	4	4
115	stable	9/2	5.5408(2)	0.810	0	5		
115m	4.49h	1/2	-0.24398(5)		0.014(3)	5		4
116	54.1m	5	4.235(15)	0.802(12)	0.048(1)	4	4	4
116m	2.18s	8	3.215(11)	0.310(9)	0.043(3)	4	4	4
117	43.8m	9/2	5.519(4)	0.829(10)	0.119(4)	4	4	4
117	1.93h	1/2	-0.25174(3)		0.125(6)	4		4
118	4.45m	5	4.231(9)	0.796(8)	0.157(2)	4	4	4
118	8.5s	8	3.321(11)	0.441(7)	0.153(2)	4	4	4
119	2.4m	9/2	5.515(10)	0.854(7)	0.220(4)	4	4	4
119	18.0m	1/2	-0.319(5)		0.222(3)	4		4
120	44.4s	5	4.295(5)	0.810(17)	0.252(2)	4	4	4
120	47.3s	8	3.692(4)	0.530(10)	0.243(6)	4	4	4
121	23.1s	9/2	5.502(5)	0.814(11)	0.306(3)	4	4	4
121	3.8m	1/2	-0.355(4)		0.305(3)	4		4
122	9.2s	5	4.318(5)	0.806(20)	0.332(4)	4	4	4
122	10.5s	8	3.781(6)	0.592(21)	0.330(5)	4	4	4
123	6.0s	9/2	5.491(7)	0.757(9)	0.385(3)	4	4	4
123	48.s	1/2	-0.400(4)		0.379(4)	4	4	4
124	3.2s	3	4.043(11)	0.614(68)	0.412(6)	4	4	4
124	2.4s	8	3.888(9)	0.664(9)	0.405(8)	4	4	4
125	2.32s	9/2	5.502(9)	0.710(36)	0.452(5)	4	4	4
125	12.2s	1/2	-0.433(4)		0.446(5)	4	4	4
126	1.53s	3	4.034(11)	0.494(49)	0.480(7)	4	4	4
126	1.45s	8	4.061(4)	0.683(12)	0.480(5)	4	4	4
127	1.15s	9/2	5.522(8)	0.589(29)	0.508(7)	4	4	4

References: 1. (Ul 85), 2. (Lo 85), 3. (Eb 86), 4. (Eb 87b) and references therein for some μ_x and Q_s values, 5. (Le 78)

Comments:

Exp. Method: 1.-4.: Standard collinear fast beam laser spectroscopy

Transitions: 1.-4.: InI 5p $^2P_{1/2}$-6s $^2S_{1/2}$ line (410nm) and 5p $^2P_{3/2}$-6s $^2S_{1/2}$ line (451nm)

μ_x-eval.: reference isotope ^{115}In

Q_s-eval.: reference isotope ^{115}In as discussed in ref. 1., Sternheimer corrected

$\delta\langle r^2\rangle$-eval.: RCDF calc. from (Fr 85): F=2.070(10)GHz/fm^2, S from K_{α} x-ray and Kingplot as disc. in ref. 1.-4.

Element: Tin Z = 50

A	$\tau_{1/2}$	I	μ_I n.m.	Q_s b.	$\delta\langle r^2\rangle^{A,116}$ fm^2	Ref. μ_I , Q_s , $\delta\langle r^2\rangle$
108	10.3m	0			-0.578(4)	2
109	18.0m	5/2	-1.079(6)	0.31(10)	-0.506(4)	2 , 2 , 2
110	4.1h	0			-0.417(3)	2(1)
111	35.m	7/2	0.608(4)	0.18(9)	-0.378(3)	2 , 2 , 2(1)
112	stable	0			-0.269(2)	2(1)
113	115.1d	1/2	-0.8791(6)		-0.212(1)	1 , , 2(1)
114	stable	0			-0.136(3)	2(1)
115	stable	1/2	-0.91883(7)		-0.096(1)	3 , , 2(1)
116	stable	0			0	
117	stable	1/2	-1.00104(7)		0.044(1)	3 , , 2(1)
117m	14.0d	11/2	-1.3955(10)	-0.42(5)	0.045(7)	1 , 1 , 2(1)
118	stable	0			0.128(1)	2(1)
119	stable	1/2	-1.04728(7)		0.165(1)	3 , , 2(1)
120	stable	0			0.241(2)	2(1)
121	27.1h	3/2	0.6978(10)	-0.02(2)	0.281(1)	1 , 1 , 2(1)
121m	55.y	11/2	-1.3877(9)	-0.14(3)	0.279(3)	1 , 1 , 1(1)
122	stable	0			0.342(3)	2(1)
123	129.d	11/2	-1.3700(9)	0.03(4)	0.367(1)	1 , 1 , 2(1)
124	stable	0			0.428(4)	2(1)
125	9.62d	11/2	-1.348(2)	0.09(17)	0.455(3)	1 , 1 , 2(1)

References: 1. (An 86b), 2. (Eb 87), 3. (Le 78)

Comments:

Exp. Method: 1. Atomic beam laser fluorescence spectroscopy
2. Standard collinear fast beam laser spectroscopy

Transitions: 1.: SnI $5p^2\ ^3P_0$-$5p6s\ ^3P_1$ (286.3nm)
2.: SnI $5p^2\ ^1S_0$-$5p6s\ ^{1,3}P_1$ (452.5nm and 563.2nm)

μ_I-eval.: reference isotopes ^{115,117,119}Sn

Q_s-eval.: semi-emp. calc. from (De 84)
and semi-emp. calc in 2., no Sternheimer-correction

$\delta\langle r^2\rangle$-eval.: 1. semi-emp. approach from (Ba 83):
F_{286}=3.3(5)GHz/fm^2, S_{286}=-1.2N
2. RDF calc. and K_α X rays acc. to 2.:
F_{452}=2.24(27)GHz/fm^2, S_{452}=-1.02N

Element: Caesium Z = 55

A	$\tau_{1/2}$	I	μ_I n.m.	Q_s b.	$\delta\langle r^2\rangle^{A,133}$ fm²	Ref. μ_I	Ref. Q_s	Ref. $\delta\langle r^2\rangle$
118	16.4s	2	3.876(5)	1.4(2)	-0.197(2)	5	5	5
119	37.7s	9/2	5.46(3)	2.8(1)	-0.136(6)	5	5	5
119m	28.s	3/2	0.838(5)	0.9(1)	-0.334(4)	5	5	5
120	64.s	2	3.87(2)	1.45(2)	-0.1185(14)	5	5	5
121	2.09m	3/2	0.770(4)	0.838(9)	-0.2555(9)	5	5	5
121m	2.9m	9/2	5.41(3)	2.69(5)	-0.0702(8)	5	5	5
122	21.s	1	-0.1333(9	-0.19(1)	-0.2524(15)	4	4	4
122m	4.5m	8	4.77(2)	3.29(8)	-0.0681(18)	4	4	4
123	5.8m	1/2	1.377(7)		-0.2078(6)	4		4
124	31.s	1	0.673(3)	-0.74(3)	-0.2008(12)	4	4	4
125	45m	1/2	1.409(7)		-0.1517(6)	4		4
126	1.64m	1	0.777(4)	-0.68(2)	-0.1586(9)	4	4	4
127	6.25h	1/2	1.459(7)		-0.0985(7)	4		4(7)
128	3.62m	1	0.974(5)	-0.570(8)	-0.1131(4)	4	4	4
129	32.06h	1/2	1.491(8)		-0.0561(11)	4		4(7)
130	29.2m	1	1.460(7)	-0.059(6)	-0.0465(10)	4	4	4
130m	3.7m	5	0.629(4)	1.45(5)	-0.0628(14)	4	4	4
131	9.688d	5/2	3.543(2)	-0.620(6)	-0.0141(7)	6(8),8		4(7)
132	6.47d	2	2.222(7)	0.508(7)	-0.0369(6)	6(8),8		4(7)
133	stable	7/2	2.582023(9)	-0.003(1)	0	6(8),6(8)		
134	2.062y	4	2.9937(9)	0.389(3)	-0.0096(11)	6(8),8		4(7)
134m	2.90h	8	1.0978(2)	0.98(8)	0.0037(16)	4	4	4
135	3×10^6y	7/2	2.7324(2)	0.050(2)	0.0250(9)	4	6	4(7)
135m	53m	19/2	2.18(1)	0.89(7)	0.0169(10)	4	4	4
136	13.10d	5	3.711(15)	0.225(10)	0.0168(14)	4(8),8		4(7)
136m	19s	8	1.319(7)	0.74(10)	0.0743(15)	4	4	4
137	30.17y	7/2	2.8413(4)	0.051(1)	0.0821(11)	3	6	4(1)
138	32.2m	3	0.700(4)	0.125(18)	0.2023(8)	4	3	4(1,3)
138m	2.9m	6	1.713(9)	-0.40(3)	0.2022(7)	4	4	4
139	9.27m	7/2	2.696(4)	-0.075(11)	0.3604(12)	3	3	4(1,3)
140	63.7s	1	0.134(1)	-0.112(7)	0.4869(13)	4	3	4(3)
141	24.94s	7/2	2.438(10)	-0.36(4)	0.6159(14)	3	3	4(3)
142	1.8s	0			0.7454(7)			4(3)
143	1.78s	3/2	0.870(4)	0.47(3)	0.8798(5)	4	4	4
144	1.00s	1	-0.546(3)	0.30(1)	0.9669(7)	5	5	5
145	0.59s	3/2	0.784(4)	0.62(6)	1.0953(10)	5	5	5
146	0.34s	1	-0.515(2)	0.22(3)	1.185(2)	5	5	5

References: 1. (Sc 78b), 2. (Hu 78b), 3. (Bo 79), 4. (Th 81b), 5. (Co 87), 6. (Le 78), 7. (Ul 75), 8. (Ac 75)

Comments:

Exp. Method: 1.+3.: Standard collinear fast beam laser spectroscopy
2.+4.-5.: Atomic beam laser spectroscopy (LIOP)
7.+8.: Optical level crossing technique

Transitions: 1.+3.: CsI D2' line (455.5 nm)
2.+4.+5.+7.+8.: CsI D2 line (852.1 nm)

μ_I-eval.: reference isotope ^{133}Cs

Q_s-eval.: 1.+3.+8.: $\langle r^{-3}\rangle_{6p}$ from semi-emp calc. in 8.
2.+4.+5.: HS-calc. from (Ro 72)
Sternheimer corrected in both cases

$\delta\langle r^2\rangle$-eval.: semi-emp. calc. in 2.,
F_{es2}=-2313 MHz/fm², S=0 GHz

Element: Barium Z = 56

A	$\tau_{1/2}$	I	μ_I n.m.	Q_s b.	$\delta\langle r^2\rangle^{A,138}$ fm^2	Ref. μ_I	Ref. Q_s	Ref. $\delta\langle r^2\rangle$
122	2.0m	0			-0.204(3)			2
123	2.7m	5/2	-0.687(18)	1.52(13)	-0.220(3)	2	2	2
124	11.9m	0			-0.175(2)			3(2)
125	3.5m	1/2	0.177(12)		-0.182(2)	2		2
126	100.m	0			-0.142(2)			1(2)
127	13.m	1/2	0.089(12)		-0.158(2)	2		2
128	2.43d	0			-0.111(1)			1(2)
129	2.23h	1/2	-0.298(16)		-0.118(1)	1		1(2)
129m	2.17h	7/2	0.930(17)	1.60(13)	-0.130(1)	1	1	1(2)
130	stable	0			-0.086(1)			1(2)
131	11.8d	1/2	-0.709(16)		-0.093(1)	1		1(2)
131m	14.6m	9/2	-0.870(18)	1.46(13)	-0.096(1)	2	2	2
132	stable	0			-0.068(1)			1(2)
133	10.74y	1/2	-0.769(3)		-0.084(1)	5		1(2)
133m	38.9m	11/2	-0.910(51)	0.89(7)	-0.072(1)	1	1	1(2)
134	stable	0			-0.053(1)			1(2)
135	stable	3/2	0.837943(17)	0.146(16)	-0.079(1)	5	2	2
135m	28.7h	11/2	-1.001(15)	0.96(8)	-0.053(1)	1	1	1(2)
136	stable	0			-0.041(1)			1(2)
137	stable	3/2	0.937365(20)	0.228(24)	-0.059(1)	5	2	2
137m	2.551m	11/2	-0.992(26)	0.78(9)	0.004(1)	2	2	2
138	stable	0			0			
139	84.63m	7/2	-0.975(17)	-0.50(4)	0.124(1)	2	2	2
140	12.75d	0			0.281(1)			2(1)
141	18.27m	3/2	-0.346(16)	0.43(4)	0.395(1)	2	2	2
142	10.6m	0			0.529(2)			2
143	14.5s	5/2	0.454(20)	-0.81(7)	0.654(2)	2	2	2
144	11.4s	0			0.793(3)			2
145	4.s	5/2	-0.272(36)	1.15(10)	0.893(3)	2	2	2
146	2.2s	0			1.019(4)			2
148	0.64s	0			1.252(5)			4

References: 1. (Be 79), 2. (Mu 83), 3. (Re 80), 4. (We 87b), 5. (Le 78)

Comments:

Exp. Method: 1.+3.: Atomic beam laser fluorescence spectroscopy
2.+4.: Standard collinear fast beam laser spectroscopy

Transitions: 1.-3.: $6s^2\ {}^1S_0$-$6s6p\ {}^1P_1$ (553.6nm)
4.: Ba II D2-line (455.4nm)

μ_I-eval.: reference isotopes ^{135,137}Ba from (Ol 72)

Q_s-eval.: semi-emp. $\langle r^{-3}\rangle_{6p}$ from (Ma 76) with Sternheimer-correction R_{6p}=-0.23(2)

$\delta\langle r^2\rangle$-eval.: semi-emp. approach, F_{554}=-3929 MHz/fm^2, S=0 GHz from Kingplot to BaII D1 (F=-4980 Mhz/fm^2 (Fi 74b)

Element: Europium Z = 63

A	$\tau_{1/2}$	I	μ_I n.m.	Q_s b.	$\delta\langle r^2\rangle^{A,145}$ fm²	Ref. μ_I	, Q_s	, $\delta\langle r^2\rangle$
140	1.3s	1	1.365(13)	0.31(4)	0.033(12)	5	, 5	, 5
141	40.s	5/2	3.494(8)	0.85(4)	0.035(9)	5	, 5	, 5(2)
142	2.4s	1	1.536(19)	0.12(5)	-0.054(10)	5	, 5	, 5(2)
142m	73.s	8	2.978(11)	1.41(6)	0.003(6)	5	, 5	, 5
143	2.6m	5/2	3.673(8)	0.51(3)	-0.026(5)	5	, 5	, 5(2)
144	10.s	1	1.893(13)	0.10(3)	-0.050(6)	5	, 5	, 5(2)
145	5.9d	5/2	3.993(7)	0.29(2)	0	5	, 5	, 5(1,2
146	4.6d	4	1.425(11)	-0.18(6)	0.124(9)	5	, 5	, 5(1,2
147	24.6d	5/2	3.724(8)	0.55(3)	0.271(17)	5	, 5	, 5(1,2,4)
148	54.5d	5	2.340(10)	0.35(6)	0.376(24)	5	, 5	, 5(1,2)
149	93.d	5/2	3.565(6)	0.75(2)	0.532(33)	5	, 5	, 5(1,2,4)
150	35.8y	5	2.708(11)	1.13(5)	0.625(39)	5	, 5	, 5(2)
150m	12.6h	0			0.634(40)			5
151	stable	5/2	3.4717(6)	0.903(10)	0.851(51)	6	, 7	, 5(2,3,4)
152	13.33y	3	-1.9414(13)	2.54(22)	1.396(81)	6	, 5	, 5(2,3,4)
152m	9.30h	0			1.112(53)			4
153	stable	5/2	1.5330(8)	2.412(21)	1.453(83)	6	, 7	, 4(3)
154	8.8y	3	-2.00	3.04	1.540(64)	4	, 4	, 4(3)
155	4.96y	5/2	1.53	2.51	1.528(61)	4	, 4	, 4
156	15.19d	0			1.565(64)			4

References: 1. (Al 83), 2. (Fe 84), 3. (Dö 83), 4. (Dö 84),
5. (Ah 85), 6. (Le 78), 7. (Ta 83)

Comments:

Exp. Method: 1.-2. Resonance ionisation spectroscopy (RIS)
3.-5. Standard collinear fast beam laser spectroscopy

Transitions: 1.-2.: EuI 5765Å line
3.-4.: EuII 6049Å line
5.: EuI 4594Å and 4627Å line

μ_I-eval.: reference isotope ^{151}Eu

Q_s-eval.: reference isotope ^{153}Eu from 7.

$\delta\langle r^2\rangle$-eval.: 4. semi-emp. approach acc. to (He 74)
5. semi-emp. approach, F_{s-sp}=-6.55GHz/fm², S=0GHz

Element: Erbium Z = 68

A	$\tau_{1/2}$	I	μ_I n.m.	Q_s b.	$\delta\langle r^2\rangle^{A,166}$ fm^2	Ref. μ_I , Q_s , $\delta\langle r^2\rangle$
153	37.1s	7/2	-0.939(7)	-0.42(2)		1 , 1
155	5.3m	7/2	-0.671(5)	-0.27(2)		1 , 1
157	25.m	3/2	-0.414(3)	0.92(1)		1 , 1
159	36.m	3/2	-0.305(2)	1.17(1)		1 , 1
161	3.21h	3/2	-0.367(3)	1.35(2)		1 , 1
162	stable	0				
163	75.0m	5/2	0.560(4)	2.56(2)		1 , 1
164	stable	0				
165	10.36h	5/2	0.646(4)	2.71(3)		1 , 1
166	stable	0			0	
167	stable	7/2	-0.5665(24)	3.565(29)		2 , 3
168	stable	0				

References: 1. (Ah 87b), 2. (Le 78), 3. (Ta 83)

Exp. Method: 1.: Standard collinear fast beam laser spectroscopy

Transitions: 1.: ErI 4151Å and 4409Å line

μ_I-eval.: reference isotope ^{167}Er

Q_s-eval.: reference isotope ^{167}Er from 3.,
no Sternheimer-correction

$\delta\langle r^2\rangle$-eval.: not given although IS is measured

---

Element: Ytterbium Z = 70

A	$\tau_{1/2}$	I	μ_I n.m.	Q_s b.	$\delta\langle r^2\rangle^{A,168}$ fm^2	Ref. μ_I , Q_s , $\delta\langle r^2\rangle$
156	24.s	0			-1.00(2)	2
158	1.1m	0			-0.9554(58)	2
159	4.6m	5/2	-0.366(8)	-0.22(2)		3 , 3 ,
160	4.8m	0			-0.7319(38)	2
161	4.2m	3/2	-0.327(8)	1.03(2)	-0.6472(32)	3 , 3 , 2
162	18.9m	0			-0.5157(28)	2
163	11.0m	3/2	-0.374(8)	1.24(2)	-0.4340(23)	3 , 3 , 2
164	76.m	0			-0.3135(27)	2
165	10.m	5/2	0.478(8)	2.48(4)	-0.2409(16)	3 , 3 , 2
166	56.7h	0			-0.1397(10)	2
167	17.5m	5/2	0.623(8)	2.70(4)	-0.0640(5)	3 , 3 , 2
168	stable	0			0	
169	32.0d	7/2	-0.635(8)	3.54(6)	0.0517(14)	3 , 3 , 2
170	stable	0			0.1173(12)	2(1)
171	stable	1/2	0.49367(1)		0.1573(14)	4 , , 2(1)
172	stable	0			0.2279(19)	2(1)
173	stable	5/2	-0.67989(3)	2.80(4)	0.2664(23)	4 , 4 , 2(1)
174	stable	0			0.3144(27)	2(1)
176	stable	0			0.3968(34)	2(1)

References: 1. (Cl 79), 2. (Bu 82), 3. (Ne 83), 4. (Le 78)

Comments:

Exp. Method: 1.: Atomic beam laser fluorescence spectroscopy
2.-3.: Standard collinear fast beam laser spectroscopy

Transitions: 1.: YbI $6s^2\ {}^1S_0$-$6s6p\ {}^3P_1$ (555.6nm)
2.-3.: YbI $6s^2\ {}^1S_0$-$6s6p\ {}^3P_1$ (555.6nm)
YbI $6s6p\ {}^3P_2$-$6s7,8s\ {}^3S1$ (769.9nm, 456.4 nm)

μ_I-eval.: reference isotopes ^{173}Yb

Q_s-eval.: reference isotope ^{173}Yb

$\delta\langle r^2\rangle$-eval.: semi-emp. approach from (He 85b)
F^{555}=35.5GHz/fm^2, N+S=296(148)GHz

Element: Gold Z = 79

A	$\tau_{1/2}$	I	μ_I n.m.	Q_s b.	$\delta\langle r^2\rangle^{A,197}$ fm^2	Ref. μ_I , Q_s , $\delta\langle r^2\rangle$
185	4.3m	5/2	2.170(17)		-0.075(9)	3 , , 4
186	10.7m	3	-1.263(29)		-0.014(8)	3 , , 4
187	8.0m	1/2	0.535(15)		-0.385(9)	3 , , 4
188	8.8m	1	-0.067(28)		-0.347(9)	3 , , 4
189	28.7m	1/2	0.494(14)		-0.309(7)	3 , , 4
189m	4.6m	11/2	6.186(20)		-0.283(9)	3 , , 4
190	42.8m	1	-0.068(26)		-0.285(6)	3(2), , 4(2)
191	3.18h	3/2	0.140(7)		-0.242(5)	2 , , 4(2)
192	5.0h	1	±0.0081(11)		-0.208(5)	2 , , 4(2)
193	17.65h	3/2	0.142(7)		-0.157(4)	2 , , 4(2)
194	39.5h	1	0.076(4)			4
195	186.d	3/2	0.151(7)		-0.076(6)	2 , , 2(1)
196	6.18d	2	0.5914(14)			5
197	stable	3/2	0.148158(8)	0.594(10)	0	5 , 5

References: 1. (Kl 83), 2. (St 85c), 3. (Wa 87), 4. (Wa 87b)
5. (Le 78)

Comments:

Exp. Method: 1.-2.: Fluorescence laser spectroscopy in cells
3.-4.: Resonance ionization spectroscopy

Transitions: 1.-4.: AuI D1 line (267.6nm)

μ_I-eval.: reference isotope ^{197}Au

Q_s-eval.: not given

$\delta\langle r^2\rangle$-eval.: MCDF calc. from (Ro 84b):
F_{268}=-43.07GHz/fm^2, S=0 GHz

Element: Mercury Z = 80

A	$\tau_{1/2}$	I	μ_I n.m.	Q_s b.	$\delta\langle r^2\rangle^{A,198}$ fm²	Ref. μ_I , Q_s , $\delta\langle r^2\rangle$
181	3.6s	1/2	0.5071(7)		-0.0953(33)	1 , , 3(1)
182	11.s	0			-0.6384(20)	3
183	8.8s	1/2	0.524(5)		-0.0527(16)	1 , , 3(1)
184	31.s	0			-0.5337(13)	3(6)
185	50.s	1/2	0.509(4)		-0.0622(6)	3(1), , 3(1)
185m	27.m	13/2	-1.017(9)	0.20(33)	-0.5357(22)	3(2),3(2),3(2)
186	1.4m	0			-0.4643(10)	3(6)
187	2.4m	3/2	-0.594(4)	-0.75(25)	-0.4324(40)	3(1),3(1),3(1)
187m	1.6m	13/2	-1.044(11)	0.45(33)	-0.4630(24)	2(2),3(2),3(2)
188	3.3m	0			-0.3944(10)	3(6)
189	7.7m	3/2	-0.6086(8)	-0.76(35)	-0.3793(24)	3(1),3(1),3(1)
189m	8.7m	13/2	-1.058(6)	0.66(26)	-0.3877(13)	2 , 3(2),3(2)
190	20.m	0			-0.3188(8)	3(1)
191	50.m	3/2	-0.618(11)	-0.80(25)	-0.3041(15)	3(1),3(1),3(1)
191m	50.8m	13/2	-1.068(5)	0.64(25)	-0.3037(13)	2 , 3(2),3(2)
192	4.9h	0			-0.2405(14)	3(1,5)
193	6.h	3/2	-0.62757(2)	-0.72(38)	-0.2340(80)	3(5),3(5),3(5)
193m	11.1h	13/2	-1.058429(3)	0.916(97)	-0.2160(24)	1 , 3(2),3(2,5)
194	260.y	0			-0.1607(7)	3(5)
195	9.5h	1/2	0.541475(1)		-0.1234(22)	4 , , 3(5)
195m	40.h	13/2	-1.044647(3)	1.08(11)	-0.1315(22)	1 , 3(2),3(2,5)
196	stable	0			-0.0809(3)	3
197	64.1h	1/2	0.5273741(9)		-0.0532(30)	4 , , 3
197m	23.8h	13/2	-1.027684(3)	1.24(14)	-0.0427(16)	1 , 3(2),3(2)
198	stable	0			0	
199	stable	1/2	0.5058851(9)		0.0119(2)	4 , , 3
199m	42.6m	13/2	-1.014703(3)	1.18(45)	0.0623(30)	1 , 3(1),3
200	stable	0			0.0935(2)	3
201	stable	3/2	-0.560225(1)	0.385(40)	0.1245(2)	4 , 3(1),3
202	stable	0			0.1970(2)	3
203	46.6d	5/2	0.84895(13)	0.343(36)	0.2288(36)	4 , 3(1),3
204	stable	0			0.2988(3)	3
205	5.2m	1/2	0.6009(1)		0.3333(20)	1 , , 3(1)
206	8.2m	0			0.3987(17)	3(2)

References: 1. (Bo 76) and references therein, 2. (Da 79), 3. (Ul 86) and references therein (updates also earlier measurements), 4. (Le 78), 5. (To 64), 6. (Kü 77)

Comments:

Exp. Method: 1. RADOP and nuclear magnetic resonance
2.+6. Fluorescence laser spectroscopy in cells
3. Standard collinear fast beam laser spectroscopy (applied only to even isotopes)
5. Classical high resolution spectroscopy

Transitions: 1.-2.+5.-6.: HgI $6s^2\ ^1S_0$- $6s6p\ ^3P_1$ (253.7nm)
3.: $6s6p\ ^3P_2$-$6s7s\ ^3S_1$ (546.1nm)

μ_I-eval.: reference isotope ^{199}Hg

Q_s-eval.: semi-emp. calc of $\langle r^{-3}\rangle_{6p}$, see 3., Sternheimer corrected

$\delta\langle r^2\rangle$-eval.: MCDF calc. from (To 85):
F_{254}=-55.36GHz/fm², S_{254}=0GHz

Element: Thallium Z = 81

A	$\tau_{1/2}$	I	μ_I n.m.	Q_m b.	$\delta\langle r^2\rangle$ fm^2	Ref. μ_I , Q_m , $\delta\langle r^2\rangle$
189m	1.4m	9/2		-2.29(4)		2
190	3.7m	7				
191	5.22m	9/2		-2.27(3)		2
192	10.8m	7				
193	21.6m	1/2				
193m	2.11m	9/2		-2.20(2)		2
194	33.0m	2	±0.14(1)			3
194m	32.8m	7				
195	1.16h	1/2	1.58(4)			3
196	1.84h	2	±0.07(12)			3
196m	1.41h	7				
197	2.84h	1/2	1.58(2)			3
198	5.3h	2	±0.00(1)			3
198m	1.87h	7	±0.640(74)			3
199	7.42h	1/2	1.60(2)			3
200	26.1h	2	±0.04(1)			3
201	73.1h	1/2	1.61(2)			3
202	12.23h	2	±0.06(1)			3
203	stable	1/2	1.622257(1)			3
204	3.78y	2	±0.0908			3
205	stable	1/2	1.6382134(7)			3
207	4.77m	1/2	1.876(5)			1

References: 1. (Ne 85b), 2. (Bo 85b), 3. (Le 78)

Comments:

Exp. Method: 1.-2.: Standard collinear fast beam laser spectroscopy

Transitions: 1.-2.: TlI 6p $^2P_{3/2}$-7s $^2S_{1/2}$ line (535.0nm)

μ_I-eval.: reference isotope ^{205}Tl

Q_m-eval.: ab initio calc. from (Li 74),
no Sternheimer-correction applied

$\delta\langle r^2\rangle$-eval.: not given, although IS is measured

Element: Lead Z = 82

A	$\tau_{1/2}$	I	μ_I n.m.	Q_s b.	$\delta\langle r^2\rangle^{A,208}$ fm^2	Ref. μ_I , Q_s , $\delta\langle r^2\rangle$
196	37.m	0			-0.6957(52)	2
197	8.m	3/2	-1.0753(22)	-0.078(174)	-0.6038(50)	2 , 2 , 2
197m	42.m	13/2	-1.1045(27)	0.469(339)	-0.5739(47)	2 , 2 , 2
198	2.4h	0			-0.5214(49)	2(1)
199	1.5h	5/2	-1.0742(12)	0.078(86)	-0.5163(42)	2(1),2(1),2(1)
200	21.5h	0			-0.4286(35)	2(1)
201	9.4h	5/2	0.6753(5)	-0.009(43)	-0.4093(34)	2(1),2(1),2(1)
202	5.3×10^4y	0			-0.3280(27)	2(1)
202m	3.62h	9	-0.2276(7)	0.581(86)	-0.3299(27)	2(1),2(1),2(1)
203	52.0h	5/2	0.6864(5)	0.095(52)	-0.3045(25)	2(1),2(1),2(1)
204	stable	0			-0.2231(18)	2(1)
205	1.5×10^7y	5/2	0.7117(4)	0.226(37)	-0.1967(16)	2(1),2(1),2(1)
206	stable	0			-0.1179(10)	2(1)
207	stable	1/2	0.592582(9)		-0.0737(6)	3 , , 2(1)
208	stable	0			0	
209	3.25h	9/2	-1.435(16)	-0.269(165)	0.0937(9)	2(1),2(1),2(1)
210	22.3y	0			0.2107(18)	2(1)
211	36.1m	9/2	-1.4037(8)	0.087(62)	0.2995(25)	2 , 2 , 2
212	10.64h	0			0.4144(38)	2(1)
214	26.8m	0			0.6099(52)	2

References: 1. (Th 83), 2. (An 86c), 3. (Le 78)

Comments:

Exp. Method: 1.-2.: Atomic beam laser spectroscopy

Transitions: 1.-2.: PbI $6p^2\ ^3P_0$-$6p7s\ ^3P_1$ (283.3nm)

μ_I-eval.: reference isotope ^{207}Pb

Q_s-eval.: semi-emp. calc. from (De 84), Sternheimer-corrected

$\delta\langle r^2\rangle$-eval.: combined analysis of muonic x-ray and electron scattering (Fr 81d):
F_{283}=20.26(18)GHz/fm^2, S=-0.81(25)N from (Ki 85)

Element: Radon Z = 86

A	$\tau_{1/2}$	I	μ_I n.m.	Q_s b.	$\delta\langle r^2\rangle^{A,212}$ fm^2	Ref. μ_I , Q_s , $\delta\langle r^2\rangle$
202	9.9s	0			-0.4382(4)	1
203m	28.s	13/2	-0.942(47)	1.28(13)	-0.4099(3)	1 , 1 , 1
204	1.24m	0			-0.3860(3)	1
205	2.83m	5/2	0.787(39)	0.062(6)	-0.3849(3)	1 , 1 , 1
206	5.7m	0			-0.3058(3)	1
207	9.3m	5/2	0.800(40)	0.220(22)	-0.2926(2)	1 , 1 , 1
208	24.m	0			-0.2125(2)	1
209	29.m	5/2	0.823(41)	0.311(31)	-0.1917(1)	1 , 1 , 1
210	2.4h	0			-0.1143(1)	1
211	14.6h	1/2	0.590(30)		-0.0735(1)	1 , , 1
212	24.m	0			0	
218	35.ms	0			0.7000(3)	1
219	3.96s	5/2	-0.434(22)	1.15(12)	0.8212(3)	1 , 1 , 1
220	55.6s	0			0.9151(3)	1
221	25.m	7/2	-0.020(1)	-0.474(48)	1.0320(4)	1 , 1 , 1
222	3.8235d	0			1.1236(4)	1

References: 1. (Bo 87)

Comments:

Exp. Method: Standard collinear fast beam laser spectroscopy

Transitions: 1.: RnI 7s-7p (745nm)

μ_I-eval.: semi-emp. calc. in 1.

Q_s-eval.: semi-emp. calc. in 1.,
no Sternheimer-correction

$\delta\langle r^2\rangle$-eval.: semi-emp. approach in 1.,
F_{745}=-22.1GHz/fm^2, S_{745}=0GHz

Element: Francium Z = 87

A	$\tau_{1/2}$	I	μ_I n.m.	Q_s b.	$\delta\langle r^2\rangle^{A,213}$ fm^2	Ref. μ_I , Q_s , $\delta\langle r^2\rangle$
207	14.8s	9/2	3.89(8)	-0.16(5)	-0.21794(16)	2 , 2 , 3(2)
208	58.6s	7	4.75(10)	0.004(38)	-0.20804(12)	1 , 2 , 3(1,2)
209	50.s	9/2	3.95(8)	-0.24(2)	-0.13043(8)	1 , 2 , 3(1,2)
210	3.2m	6	4.40(9)	0.19(2)	-0.10831(4)	1 , 2 , 3(1,2)
211	3.1m	9/2	4.00(8)	-0.19(3)	-0.03757(4)	5 , 2 , 3(1,2)
212	19.3m	5	4.62(9)	-0.10(1)	0	1 , 2
213	34.7s	9/2	4.02(1)	-0.14(2)	0.06829(8)	1(4),2(4),3(1,2,4)
220	27.4s	1	-0.67(1)	0.482(2)	0.86725(45)	2(4),2(4),3(1,2,4)
221	4.8m	5/2	1.58(3)	-1.00(1)	0.98269(33)	2(4),2(4),3(1,2,4)
222	14.4m	2	0.63(1)	0.51(4)	1.09543(12)	2 , 2 , 3(2)
223	21.8m	3/2	1.17(2)	1.17(1)	1.16507(8)	2 , 2 , 3(2)
224	2.7m	1	0.40(1)	0.517(4)	1.28937(4)	2 , 2 , 3(2)
225	3.9m	3/2	1.07(2)	1.32(1)	1.34862(22)	2 , 2 , 3(2)
226	48.s	1	0.071(2)	-1.35(2)	1.43700(4)	2 , 2 , 3(2)
227	2.4m	1/2	1.50(3)		1.60249(8)	2 , 2 , 3(2)
228	39.s	2	-0.76(2)	2.38(5)	1.67522(20)	2 , 2 , 3(2)

References: 1. (Li 80), 2. (Co 85), 3. (Co 87), 4. (Du 87), 5. (Ro 84)

Comments:

Exp. Method: 1.-3.: Atomic beam laser spectroscopy and laser rf double resonance
4.: Standard collinear fast beam laser spectroscopy

Transitions: 1.-3.: FrI D1 and D2 line
4.: FrI D1' and D2` line

μ_I-eval.: reference isotope ^{211}Fr

Q_s-eval.: RMBPT calc. of $\langle r^{-3}\rangle_{7p}$ from (He 83b)
Sternheimer-correction R_{6p}=-0.23(2)

$\delta\langle r^2\rangle$-eval.: semi-emp. approach in 3.

Element: Radium Proton Number Z: 88

A	$\tau_{1/2}$	I	μ_I n.m.	Q_s b.	$\delta\langle r^2\rangle^{A,214}$ fm^2	Ref. μ_I , Q_s , $\delta\langle r^2\rangle$
208	1.3s	0			-0.292(15)	3
209	4.7s	5/2	0.860(16)	0.38(4)	-0.284(14)	4(1),2(1),3
210	3.7s	0			-0.207(11)	3
211	13.s	5/2	0.879(9)	0.46(5)	-0.190(10)	4(1),2(1),3
212	13.0s	0			-0.112(6)	3
213	2.7m	1/2	0.6133(18)		-0.075(4)	4(1), , 3
214	2.46s	0			0	
220	23.ms	0			0.766(39)	3
221	30.s	5/2	-0.179(2)	1.90(20)	0.907(46)	4(1),2(1),3
222	38.s	0			1.007(50)	3
223	11.435d	3/2	0.271(3)	1.19(12)	1.132(58)	4(1),2(1),3
224	3.66d	0			1.225(63)	3
225	14.8d	1/2	-0.7338(15)		1.355(70)	4(1), , 3
226	1.6×10^3y	0			1.433(74)	3
227	42.2m	3/2	-0.404(4)	1.50(15)	1.530(78)	4(1),2(), 3
228	5.76y	0			1.635(84)	3
229	4.0m	5/2	0.503(5)	2.96(30)	1.743(90)	4(1),2(1),3
230	93.m	0			1.867(96)	3
232	?	0			2.073(107)	3

References: 1. (Ah 83), 2. (We 87), 3. (Ah 87), 4. (Ar 87)

Comments:

Exp. Method: 1.-3.: Standard collinear fast beam laser spectroscopy
4.: Collinear laser spectroscopy with spin rotation

Transitions: RaII D1 line (468.3nm)
RaI $7s^2\ {}^1S_0$-$7s7p\ {}^{1,3}P_1$ (482,7nm, 714.1nm)
RaI $7s7p\ P_2$-$7s7d\ {}^3D_3$ (468.3nm)

μ_I-eval.: direct determination in 4. by comparison to ^{137}Ba

Q_s-eval.: semi-emp. calc. in 2.,
Sternheimer-correction R_{7p}=-0.24(5)

$\delta\langle r^2\rangle$-eval.: average value of semi-emp. calc. and MCDF result from (To 85), see disc. in 2.

8. References

Ab 61 A. Abragam, The Principle of Nuclear Magnetism, Oxford Univ. Press, London (1961)

Ac 75 F. Ackermann, E.W. Otten, G. zu Putlitz, A. Schenck and S. Ullrich, Nucl. Phys. A248: 157 (1975)

Ah 83 S.A. Ahmad, W. Klempt, R. Neugart, E.W. Otten, K. Wendt and C. Ekström, Phys. Lett. 133B: 47 (1983)

Ah 85 S.A. Ahmad,W. Klempt, C. Ekström, R. Neugart, K. Wendt, Z. Phys. A321: 35 (1985)

Ah 87 S.A. Ahmad, W. Klempt, R. Neugart, E.W. Otten, K. Wendt, C. Ekström, to be published

Ah 87b S.A. Ahmad, W. Klempt, R. Neugart, K. Wendt and C. Ekström, to be published

Al 83 J.D. Alkhazov, A.E. Barzakh, E.I. Berlovich, V.P. Denisov, A.J. Dernyatin, V.S. Ivanov, A.N. Zherikhin, O.N. Kompanets, V.S. Letokhov, V.I. Mishin, V.N. Fedoseyev, JETP Lett. 37: 274 (1983)

Al 85 C.F. Alonso, J.M. Arias and F. Iachello, Phys. Lett. 164B: 241 (1985)

An 78 K.R. Anton, S.L. Kaufman, W. Klempt, G. Moruzzi, R. Neugart, E.W. Otten and B. Schinzler, Phys. Rev. Lett. 40: 642 (1978)

An 80 I. Angeli, M. Beiner, R.J. Lombard and D. Mas, J. Phys. G6: 303 (1980)

An 82 A. Andl, K. Bekk, S. Göring, A. Hanser, G.

Nowicki, H. Rebel, G. Schatz, R.C. Thompson, Phys. Rev. C26: 2194 (1982)

An 86 M. Anselment, S. Chongkum, K. Bekk, S. Göring, A. Hanser, G. Meisel, H. Rebel, Z. Phys. D3: 421 (1986)

An 86b M. Anselment, K. Bekk, A. Hanser, H. Hoeffgen, G. Meisel, S. Göring, H. Rebel, G. Schatz, Phys. Rev. C34: 1052 (1986)

An 86c M. Anselment, W. Faubel, S. Göring, A. Hanser, G. Meisel, H. Rebel, G. Schatz, Nucl. Phys. A451: 471 (1986)

An 86d S.V. Andreev, V.I. Mishin and V.S. Letokhov, Opt. Comm. 57: 317 (1986)

Ar 71 L. Armstrong, Theory of the Hyperfine Structure of Free Atoms, J. Wiley and Sons Inc., New York (1971)

Ar 86 E. Arnold, thesis, Mainz (1986) and
E. Arnold, J. Bonn, R. Gegenwart, W. Neu, R. Neugart, E.W. Otten, G. Ulm and K. Wendt, to be published

Ar 87 E. Arnold, W. Borchers, M. Carre, H.T. Duong, P. Juncar, J. Lerme, S. Liberman, W. Neu, R. Neugart, E.W. Otten, M. Pellarin, J. Pinard, G. Ulm, J.L. Vialle, K. Wendt, subm. to Phys. Rev. Lett.

Au 85 P. Aufmuth and E. Wöbker, Z. Phys. A321: 65 (1985)

Au 86 P. Aufmuth and E. Wöbker, Z. Phys. D2: 131 (1986)

Ba 73 R. Bauer, J. Speth, V. KLemt, P. Ring, E. Werner and T. Yamazaki, Nucl. Phys. A209: 535 (1973)

Ba 74 R.C. Barret, Rep. Prog. Phys. 37: 1 (1974)

Ba 83 P.E.G. Baird, S.A. Blundell, G. Burrows, C.J. Foot, G. Meisel, D.N. Stacey, G.K. Woodgate, J. Phys. B16: 2485 (1983)

Ba 85 F. Barranco and R.A. Broglin, Phys. Lett. 151B: 90 (1985)

Ba 86 H. Backe, Mainz, private communication

Be 73 M. Beiner and R.J. Lombard, Phys. Lett 47B: 399 (1973)

Be 74 A. Beckmann, K.D. Böklen and D. Elke, Z. Phys. 270: 173 (1974)

Be 79 K. Bekk, A. Andl, S. Göring, A. Hanser, G. Nowicki H. Rebel, G. Schatz, Z. Phys. A291: 219 (1979)

Be 79b C.E. Bemis, jr., J.R. Beene, J.P. Young, S.D. Kramer, Phys. Rev. Lett. 43: 1854 (1979)

Be 80 E. Bergmann, P. Bopp, C. Dorsch, J. Kowalski, F. Träger, G. zu Putlitz, Z. Phys. A294: 319 (1980)

Be 82 C.E. Bemis, jr. and H.K. Carter (eds.), Lasers in Nucl. Physics, Harwood Academic Publishers, New York (1982)

Be 84 C. Bengtsson, C. Ekström, L. Robertsson, J. Heinemeier, Phys. Scr. 30: 164 (1984)

Be 84b N. Bendali, H.T. Duong, P. Juncar, S. Liberman, J. Pinard, J.M. Saint-Jalm, J.L. Vialle, S. Büttgenbach, C. Thibault, F. Touchard, A. Pesnelle A.C. Mueller, C.R.Acad. Sc. 299: 1157 (1984)

Be 84c N. Bendali, H.T. Duong, J.M. Saint-Jalm, J.L.

Vialle, J. Phys. 45: 421 (1984)

Be 84d D. Bender, H. Brand and V. Pfeufer, Z. Phys. A318: 291 (1984)

Be 85 D. Berdichevsky, F. Tondeur, Z. Phys. A322: 141 (1985)

Bj 80 S. Bjornholm, J.E. Lynn, Rev. Mod. Phys 52: 725 (1980)

Bl 85 S.A. Blundell, P.E.G. Baird, C.W.P. Palmer, D.N. Stacey, G.K. Woodgate, D. Zimmermann, Z. Phys. A321: 31 (1985)

Bo 59 R.A. Bodmer, Nucl. Phys. 9: 371 (1959)

Bo 69 A. Bohr and B.R. Mottelson, Nuclear Structure, Vol. 1, Benjamin, New York (1969)

Bo 71 J. Bonn, G. Huber, H.J. Kluge, U. Köpf, L. Kugler, E.W. Otten, Phys. Lett. 36B: 41 (1971)

Bo 72 J. Bonn, G. Huber, H.J. Kluge, L. Kugler, E.W. Otten, Phys. Lett. 38B: 308 (1972)

Bo 74 F. Boehm and P.L. Lee, At. Data and Nucl. Data Tables 14: 605 (1974)

Bo 75 A. Bohr and B.R. Mottelson, Nuclear Structure, Vol. 2, Benjamin, New York (1975), p. 556 ff.

Bo 76 J.Bonn, G. Huber, H.J. Kluge and E.W. Otten, Z. Phys. A276: 203 (1976)

Bo 79 J. Bonn, W. Klempt, R. Neugart, E.W. Otten and B. Schinzler, Z. Phys. A289: 227 (1979)

Bo 82 C. Bourgeois, P. Kilcher, B. Roussiere, J. Sauvage-Letessier and M.G. Porquet, Nucl. Phys. A386: 308 (1982)

Bo 83 G.L. Borchert, O.W.B. Schult, J. Speth, P.G. Hansen, B. Jonson, H.L. Ravn and J.B. Mc. Grory, Nuovo Cimento 73A: 273 (1983)

Bo 85 J. Bonn, Hyp. Int. 22: 57 (1985)

Bo 85b J.A. Bounds, C.R. Bingham, P. Juncar, H.K. Carter, G.A. Leander, R.L. Mlekodaj, E.H. Spejewski and W.M. Fairbank, jr., Phys. Rev. Lett. 55: 2269 (1985)

Bo 87 W. Borchers, R. Neugart, E.W. Otten, H.T. Duong, G. Ulm and K. Wendt, Hyp. Int. in print and to be published

Br 52 P. Brix, Z. Phys. 132: 579 (1952)

Br 77 P. Brix, Naturwissenschaften 64: 293 (1977)

Br 78 H.W. Brandt, K. Heilig, H. Knöckel and A. Steudel, Z. Phys. A288: 241 (1978)

Br 85 P. Brix, Z. Naturforschung 41a: 3 (1986)

Bu 81 F. Buchinger, P. Dabkiewicz, H.J. Kluge, A.C. Müller, E.W. Otten, Hyp. Int. 9: 165 (1981) and in print at Nucl. Phys.

Bu 82 F. Buchinger, A.C. Mueller, B. Schinzler, K. Wendt, C. Ekström, W. Klempt and R. Neugart, Nucl. Instr. Meth. 202: 159 (1982)

Bu 85 F. Buchinger, R. Corriveau, E.B. Ramsay, D. Berdichevsky, D.W.L. Sprung, Phys. Rev. C32: 2058 (1985)

Bu 87 F. Buchinger, P. Dabkiewicz, H.J. Kluge, A.C. Mueller, E.W. Otten, subm. to Nucl. Phys. A

Bü 82 S. Büttgenbach, Hyperfine Structure in 4d and 5d shell atoms, Springer-Verlag, Berlin (1982)

Ca 35 H. Casimir, Physica 2: 719 (1935)

Ca 73 U. Cappeler, W. Mazurkewitz, Journal of Magnetic Resonance 10: 15 (1973)

Ca 73b M. Cailliau, J. Letessier, H. Flocard, P. Quentin, Phys. Lett. 46B: 11 (1973)

Ca 75 X. Campi, H. Flocard, A. Kerman and S. Koonin, Nucl. Phys. A251: 193 (1975)

Ca 80 X. Campi and M. Epherre, Phys. Rev. C22: 2605 (1980)

Ca 81 R.F. Casten, D.D. Warner, D.S. Brenner and R.L. Gill, Phys. Rev. Lett. 47, 1433 (1981)

Ca 85 R.F. Casten, Phys. Rev. Lett. 54: 1991 (1985)

Ca 85b F. Calaprice, Hyp. Int. 22: 83 (1985)

Ca 85c F. Calaprice, W. Happer, D.F. Schreiber, M.M. Lowry, E. Miron and X. Zeng, Phys. Rev. Lett. 54: 174 (1985)

Ca 86 F. Calaprice, Princeton, private communication and to be published

Ca 86b M. Carre, J. Lerme and J.L. Vialle, J. Phys. B19: 2853 (1986)

Ch 80 R.R. Chasman, Phys. Lett. 96B: 7 (1980)

Cl 79 D.L. Clark, M.E. Cage, D.A. Lewis and G.W. Greenlees, Phys. Rev. A20: 239 (1979)

Co 76 J.D. Cole, J.H. Hamilton, A.V. Ramayya, W.G. Nettles, H. Kawakami, E.H. Spejewski, M.A. Ijaz, K.S. Toth, E.L. Robinson, K.S.R. Sastry, J. Lin,

F.T. Avignone, W.H. Brantley and P.V.G. Rao, Phys. Rev. Lett. 37: 1185 (1976)

Co 83 F.D. Correll, L. Mandansky, R.A. Hardekopf and J.W. Sunier, Phys. Rev. C28: 862 (1983)

Co 85 A. Coc, C. Thibault, F. Touchard, H.T. Duong, P. Juncar, S. Liberman, J. Pinard, J. Lerme, J.L. Vialle, S. Büttgenbach, A.C. Mueller, A. Pesnelle, Phys. Lett. 163B: 66 (1985)

Co 87 A. Coc, C. Thibault, F. Touchard, H.T. Duong, P. Juncar, S. Liberman, J. Pinard, M. Carre, J. Lerme, J.L. Vialle, S. Büttgenbach, A.C. Mueller, A. Pesnelle, subm. to Nucl. Phys. A

Da 78 P. Dabkiewicz, C. Duke, H. Fischer, T. Kühl, H.J. Kluge, H. Kremmling, E.W. Otten and H. Schüssler, J. Phys. Soc. Japan 44, Suppl.: 503 (1978)

Da 79 P. Dabkiewicz, F. Buchinger, H. Fischer, H.J. Kluge, H. Kremmling, T. Kühl, A.C. Müller, H.A. Schuessler, Phys. Lett. 82B: 199 (1979)

Da 86 T.P. Das, New York, private communication

De 84 J. Dembczynski, H. Rebel, KFK-Rep. 3815: 64 (1984)

De 84b J. Dembczynski and H. Rebel, Z. Phys. A315: 137 (1984)

Di 73 F. Dickmann, K. Dietrich, Z. Phys. 263: 211 (1973)

Di 74 F. Dickmann, K. Dietrich, Z. Phys. 271: 417 (1974)

Do 84 J. Dobaczewski, M. Flocard and J. Treiner, Nucl. Phys. A422: 103 (1984)

Dö 83 K. Dörschel, W. Hedderich, H. Hühnermann, E.W.

Peau, H. Wagner, G.D. Alkhazov, E.Y. Berlovich, V.P. Denisov, V.N. Panteleev, A.G. Polyakov, Z. Phys. A 312: 269 (1983)

Dö 84 K. Dörschel, W. Hedderich, H. Hühnermann, E.W. Peau, H. Wagner, G.D. Alkhazov, E.Y. Berlovich, V.P. Denisov, V.N. Panteleev, A.G. Polyakov, Z. Phys. A317: 233 (1984)

Du 86 H.T. Duong, S. Liberman, J. Pinard, C. Thibault, F. Touchard, M. Carre, J. Lerme, J.L. Vialle, P. Juncar, S. Büttgenbach, A. Pesnelle, J. de Phys. 47: 1903 (1986)

Du 87 H.T. Duong, P. Juncar, S. Liberman, A.C. Mueller, R. Neugart, E.W. Otten, B. Peuse, J. Pinard, H.H. Stroke, C. Thibault, F. Touchard, J.L. Vialle, K. Wendt, Europhys. Lett. 3: 175 (1987)

Dz 83 V.A. Dzuba, V.V. Flambaum, O.P. Sushkov, Phys. Lett. 95A: 230 (1983)

Dz 85 V.A. Dzuba, V.V. Flambaum and O.P. Sushkov, Phys. Scr. 32: 507 (1985)

Ea 86 D.A. Eastham, P.M. Walker, J.R.H. Smith, J.A.R. Griffith, D.E. Evans, S.A. Wells, M.J. Fawcett, I.S. Grant, J. Phys. G12: 205 (1986)

Ea 87 D.A. Eastham, P.M. Walker, J.R.H. Smith, D.D. Warner, J.A.R. Griffith, D.E. Evans, S.A. Wells, M.J. Fawcett,I.S. Grant, subm. to Phys. Rev. Lett.

Eb 86 J. Eberz, U. Dinger, T. Horiguchi, G. Huber, H. Lochmann, R. Menges, R. Kirchner, O. Klepper, T. Kühl, D. Marx, E. Roeckl, D. Schardt and G. Ulm,

Z. Phys. A323: 119 (1986)

Eb 87 J. Eberz, U. Dinger, G. Huber, H. Lochmann, R. Menges, G. Ulm, R. Kirchner, O. Klepper, T. Kühl, D. Marx, subm. to Z. Phys. A

Eb 87b J. Eberz, U. Dinger, G. Huber, H. Lochmann, R. Menges, R. Neugart, R. Kirchner, O. Klepper, T. Kühl, D. Marx, G. Ulm and K. Wendt, Nucl. Phys. A 464: 9 (1987)

Eg 78 T.v. Egidy, W. Kaiser, W. Mampe, C. Hillebrand, W. Stöffl, R.G. Lanier, K. Mühlbauer, O.W.B. Schult, H.R. Koch, H.A. Baader, R.L. Mlekodaj, R.K. Sheline, E.B. Shera, J. Ungrin, P.T. Prokofjev, L.I. Simonova, M.K. Balodis, H. Seyfarth, B. Kardon, W. Delang, P. Göttel, D. Breitig, W.R. Kane, R.F. Casten, H.J. Scheerer, P. Glässl, E. Huenges, M. Löffler, H. Rösler and H.K. Vonach, Z. Phys. A286: 341 (1978)

Ei 70 J.M. Eisenberg and W. Greiner, Nucl. Models, Vol. 1, North Holland Publ. Corp., Amsterdam (1970)

Ek 77 C. Ekström, S. Ingelman, G. Wannberg, M.Skarestad, Nucl. Phys. A292: 144 (1977)

Ek 78 C. Ekström, S. Ingelman, G. Wannberg and M. Skarestad, Nucl. Phys. A311: 269 (1978)

Ek 79 C. Ekström, L. Robertsson, G. Wannberg, J. Heinemeier, Phys. Scr. 19: 516 (1979)

Ek 80 C. Ekström, L. Robertsson, S. Ingelman, G. Wannberg and I. Ragnarsson, Nucl. Phys. A348: 25

(1980)

Ek 81 C. Ekström, Proc. 4th Int Conf. on Nucl. far from Stab., Helsingör 1981, CERN Rep. 81-09, Geneva (1981), p. 12

Ek 84 C. Ekström, L. Robertsson, J. Heinemeier, Phys. Scr. 30: 164 (1984)

Em 83 H.J. Emrich, G. Fricke, G. Mallot, H. Miska H.G. Sieberling, J.M. Cavedon, B. Frois and D. Goutte, Nucl. Phys. A396: 401c (1983)

En 74 H. Engfer, H. Schneuwly, J.L. Vuilleumier, H.K. Walter and A. Zehnder, At. Data Nucl. Data Tables 14: 509 (1974)

Ep 81 M. Epherre, G. Audi and X. Campi, Proc. 4th Int. Conf. on Nuclei far from Stability, Helsingör 1981 CERN Rep. 81-09: 62 (1981)

Fa 81 A. Faessler, Hyp. Int. 9: 3 (1981)

Fa 72 A. Faessler, U. Götz, B. Slavov, T. Ledergerber, Phys. Lett. 39B: 579 (1972)

Fe 77 P. Federmann and S. Pittel, Phys. Lett 69B: 385 (1977)

Fe 78 P. Federmann and S. Pittel, Phys. Lett. 77B: 29 (1978)

Fe 84 V.N. Fedoseyev, V.S. Lethokov, V.I. Mishin, G.D. Alkhazov, A.E.Barzakh, V.P. Denisov, A.G. Dernyatin, V.S. Ivanov, Opt. Comm. 52: 24 (1984)

Fi 74 W. Fischer, H. Hühnermann, G. Krömer and H.J. Schäfer, Z. Phys. 270: 113 (1974)

Fi 74b W. Fischer, M. Hartmann, H. Hühnermann and H.

Vogg, Z. Phys. 267: 209 (1974)

Fr 75 S. Frauendorf, V.V. Pashkevich, Phys. Lett. 55B: 365 (1975)

Fr 81 G. Fricke in Proc. 4th Int. Conf. on Nuclei far from Stability, Helsingör 1981, CERN Rep. 81-09, Geneva (1981)

Fr 81b J. Friedrich and N. Voegler, Phys. Rev. Lett. 47: 1385 (1981)

Fr 82 J. Friedrich and N. Voegler, Nucl. Phys. A373: 192 (1982)

Fr 83 G. Fricke, Mainz, private communication, referred to in ref. (Bo 83)

Fr 85 B. Fricke, Kassel, private communication

Fr 86 G. Fricke, Mainz, private communication

Ge 79 H. Gerhardt, E. Matthias, H. Rinneberg, F. Schneider, A. Timmermann, R. Wenz and P.J. West, Z. Phys. A292: 7 (1979)

Ge 81 H. Gerhardt, F. Jeschonnek, W. Makat, E. Matthias, H. Rinneberg, F. Schneider, A. Timmermann, R. Wenz and P.J. West, Hyp. Int. 9: 175 (1981)

Ge 86 R. Gegenwart, doctoral thesis, Mainz (1986) and R. Gegenwart, E. Arnold, D. Bauer, J. Bonn, E.W. Otten and K.P.C. Spath, to be published

Gi 82 M. Girod and P.G. Reinhard, Phys. Lett. 117B: 1 (1982)

Gr 60 D.P. Grechukhin, Sov. Phys. JETP 11: 1359 (1960)

Gr 71 S. Green, Phys. Rev. A4: 251 (1971)

Ha 73 R.C. Haskell , L. Mandansky, Phys. Rev. C7, 1277 (1973)

Ha 85 J.H. Hamilton, P.G. Hansen and E.F. Zganjar, Rep. Prog. Phys. 48: 631 (1985)

He 56 R.H. Helm, Phys. Rev. 104: 1466 (1956)

He 61 K. Heilig, Z. Phys. 161: 252 (1961)

He 71 P. Heinecke, Z. Phys. 245: 411 (1971)

He 74 K. Heilig and A. Steudel, At. Data. Nucl. Data Tables 14: 613 (1974)

He 83 K. Heyde, P. van Isacker, M. Waroquier, J.L. Wood, R.A. Meyer, Phys. Rep. 102: 291 (1983)

He 83b J.L. Heully and A.M. Martensson-Pendrill, Phys. Rev. A27: 3332(1983)

He 85 J.L. Heully and A.M. Martensson-Pendrill, Phys. Scr. 31: 169 (1985)

He 85b K. Heilig, Hyp. Int. 24-26: 349 (1985)

Ho 73 P. Hornshoj, P.G. Hansen, B. Jonson, A. Lindahl, O.B. Nielsen, Phys. Lett. 43B: 377 (1973)

Ho 84 B. Hoffmann, G. Baur and J. Speth, Z. Phys. 315: 57 (1984)

Hu 75 G. Huber, C. Thibault, R. Klapisch, H.T. Duong, J.L. Vialle, J. Pinard, P. Juncar, P. Jaquinot, Phys. Rev. Lett. 34: 1209 (1975)

Hu 76 G. Huber, J. Bonn, H.J. Kluge, E.W. Otten, Z. Phys. A276: 187 (1976)

Hu 78 G. Huber, F. Touchard, S. Büttgenbach, C. Thibault, R. Klapisch, H.T. Duong, S. Liberman, J. Pinard, J.L. Vialle, P. Juncar, P. Jaquinot, Phys.

Rev. C18: 2342 (1978)

Hu 78b G. Huber, F. Touchard, S. BÜttgenbach, C. Thibault, R. Klapisch, S. Libermann, J. Pinard, H.T. Duong, P. Juncar, J.L. Vialle, P. Jacquinot and A. Pesnelle, Phys. Rev. Lett. 41: 459 (1978)

Hu 79 G.S. Hurst, M. G. Payne, S.D. Kramer, J.P Young, Rev. Mod. Phys. 51: 767 (1979)

Hy 80 H. Hyuga, A. Arima and K. Shimizu, Nucl. Phys. A336: 363 (1980)

Ia 81 F. Iachello, Nucl. Phys. A358: 89c (1981)

Ia 83 F. Iachello, Hyp. Int. 15/16: 11 (1983) and references therein

Ja 37 H.A. Jahn and E. Teller, Proc. Roy. Soc. A161: 220 (1937)

Ja 74 C.W. de Jager, H. de Vries and C. de Vries, At. Data Nucl. Data Tables, 14: 479 (1974)

Ja 76 P. Jaquinot, in High Resolution Laser Spectroscopy (ed. K. Shimoda), Topics in Applied Phys. 13: 51, Springer Verlag, Heidelberg (1976)

Ja 79 P. Jaquinot and R. Klapisch, Rep. Progr. Phys. 42: 773 (1979)

Ka 76 S.L. Kaufmann, Opt. Comm. 17: 309 (1976)

Ka 81 G. Kaindl and H. Haas, eds., Proc. 5th Int. Conf. on Hyperfine Interactions, Berlin, 1980, Hyp. Int. 9/10 (1981)

Ki 84 W.H. King, Isotope Shifts in Atomic Spectra, Plenum Press, New York (1984)

Ki 85 W.H. King and H. Wilson, J. Phys. G11: L43 (1985)

Ki 86 W.H. King and C.W. Palmer, Comm. in At. and Mol. Phys. 18: 11 (1986)

Kl 79 H.-J. Kluge, in Progress in Atomic Spectroscopy, Part B (W. Hanle and H. Kleinpoppen, ed.) Plenum Publishing Corporation, New York (1979), p. 727

Kl 79b W. Klempt, J. Bonn and R. Neugart, Phys. Lett. 82B: 47 (1979)

Kl 82 P. Kleinheinz, J. Styczen, M. Piiparinen, J. Blomquist and M. Kortelahti, Phys. Rev. Lett. 48: 1457 (1982)

Kl 83 H.J. Kluge, H. Kremmling, H.A. Schuessler, J. Streib and K. Wallmeroth, Z. Phys. A309: 187 (1983)

Kl 85 H.-J. Kluge, Hyp. Int. 24-26: 69 (1985)

Ko 58 H. Kopfermann, Nuclear Moments, Academic Press, New York, 1958

Ko 75 D. Kolb, C.Y. Wong, Nucl. Phys. A245: 205 (1975)

Kö 69 U. Köpf, H.J. Besch, E.W. Otten, C. von Platen, Z. Phys. 226: 297 (1969)

Kr 79 H. Kremmling, P. Dabkiewicz, H. Fischer, H.J. Kluge, T. Kühl, H.A. Schüssler, Phys. Rev. Lett. 43: 1376 (1979)

Kr 85 G.B. Krygin, V.E. Mitroshin, Sov. J. Nucl. Phys. 41, 193 (1985)

Ku 69 H.G. Kuhn, Atomic Spectra, Longmans Group limited, London (1969)

Ku 72 K. Kumar, Phys. Rev. Let. 28: 249 (1972)

Ku 83 W. Kunold, M. Schneider, L.M. Simons, J. Wüst, R. Abela, Z. Phys. A313: 11 (1983)

Kü 77 T. Kühl, P. Dabkiewicz, C. Duke, H. Fischer, H.J. Kluge, H. Kremmling, E.W. Otten, Phys. Rev. Lett. 39: 180 (1977)

La 78 S.E. Larsson, G.A. Leander and I. Ragnarsson, Nucl. Phys. A 307: 189 (1978)

Le 78 C.M. Lederer and V.S. Shirley, Table of Isotopes, 7.ed., Wiley, New York (1978)

Le 84 V.S. Letokhov, Nonlinear Laser Chemistry, Springer Series Chem. Phys. 22, Springer Verlag, Heidelberg Berlin (1984)

Le 84b G.A. Leander and R.K. Sheline, Nucl. Phys. A413: 375 (1984)

Le 86 V.S. Letokhov, Moscow, private communication

Li 74 I. Lindgren and A. Rosen, Case Stud. in At. Phys. 4: 93 (1974)

Li 78 S. Liberman, J. Pinard, H.T. Duong, P. Juncar, J.L Vialle, P. Jaquinot, G. Huber, F. Touchard, S. Büttgenbach, A. Pesnelle, C. Thibault, R. Klapisch, C.R. Acad. Sci. B286: 253 (1978)

Li 80 S. Liberman, J. Pinard, H.T. Duong, P. Juncar, P. Pillet, J.L Vialle, P. Jaquinot, F. Touchard, S. Büttgenbach, C. Thibault, M. de Saint Simon, R. Klapisch, A. Pesnelle, G. Huber, Phys. Rev. A22: 2732 (1980)

Lo 85 H. Lochmann, U. Dinger, J. Eberz, G. Huber, R.

Menges, G. Ulm, R. Kirchner, O. Klepper, T. Kühl, D. Marx and D. Schardt, Z. Phys. A322: 703 (1985)

Lö 70 K.E.G. Löbner, M. Vetter, and W. Hönig, Nucl. Data Tables A7: 495 (1970)

Ma 71 E. Matthias, B. Olsen, D.A. Shirley, J.E. Templeton, R.M. Steffen, Phys.Rev. A4: 1626 (1971)

Ma 76 I.J. Ma and G. zu Putlitz, Z. Phys. A277: 107 (1976)

Me 77 T. Meier, H. Hühnermann and H. Wagner, Opt. Comm. 20: 397 (1977)

Me 86 R.A. Meyer et al, eds., Proc. Tnt. Conf. on Nucl. Structure, Reactions and Symmetries, Dubrovnik (1986), in print at World Scientific Publishers, Signapore

Mi 75 T. Minamisono, J.W. Hugg, D.G. Mavis, T.K. Saylor, S.M. Lazarus, H.F. Glavish and S.S. Hanna, Phys. Rev. Lett. 34: 1465 (1975)

Mö 84 P. Möller, W.D. Myers, W.J. Swiatecki, J. Treiner, Proc. 7th Int. Conf. on At. Masses and Fund. Const., AMCO-7 (O. Klepper, ed.), p. 457, Darmstadt-Seeheim (1984)

Mu 83 A.C. Mueller, F. Buchinger, W. Klempt, E.W. Otten, R. Neugart, C. Ekström, J. Heinemeier, Nucl. Phys. A403: 234 (1983)

My 69 W.D. Myers and W.J. Swiatecki, Ann. Phys. (N.Y.) 55: 395 (1969)

My 77 W.D. Myers, Droplet Model of At. Nuclei, IFI/Plenum Data Co., New York (1977)

My 83 W.D. Myers and K.H. Schmidt, Nucl. Phys. A410: 61 (1983)

Na 84 W. Nazarewicz, P. Olanders, I. Ragnarsson, J. Dudek, G.A. Leander, P. Möller and E. Ruchowska, Nucl. Phys. A429: 269 (1984)

Ne 78 W. Neuhauser, M. Hohenstatt, P.E. Toschek, H.G. Dehmelt, Phys. Rev. Lett. 41: 233 (1978)

Ne 82 R. Neugart, in Lasers in Nucl. Physics, (C.E. Bemis, jr. and H.K. Carter, ed.) Harwood Academic Publishers, New York (1982), p.

Ne 83 R. Neugart, K. Wendt, S.A. Ahmad, W. Klempt and C. Ekström, Hyp. Int. 15/16: 181 (1983)

Ne 85 R. Neugart, Hyp. Int. 24-26: 159 (1985)

Ne 85b R. Neugart, H.H. Stroke, S.A. Ahmad, H.T. Duong, H.L. Ravn and K. Wendt, Phys. Rev. Lett. 55: 1559 (1985)

Ne 86 R. Neugart, W. Klempt and K. Wendt, Nucl. Instr. Meth. B17: 354 (1986)

Ni 57 W.A. Nierenberg, Ann. Rev. Nucl. Sci. 7: 349 (1957)

Ni 74 S.G. Nilsson, J.R. Nix, P. Möller and I. Ragnarsson, Nucl. Phys. A222: 221 (1974)

Ni 83 L. Niesen, F. PLeiter, H. de Waard, eds., Proc. 6th Int. Conf. on Hyperfine Interactions, Groningen, 1983, Hyp. Int. 15/16 (1983)

No 78 G. Nowicki, K. Bekk, S. Göring, A. Hanser, H. Rebel, G. Schatz, Phys. Rev. C18: 2369 (1978)

Ol 72 L. Olschewski, Z. Phys. 249: 205 (1972)

Ot 81 E.W. Otten, Nucl. Phys. A354: 471c (1981)

Ot 85 E.W. Otten, Proc. of Symp. Alfred Kastler, Paris 1985, Ann. Phys. Fr. 10: 659 (1985)

Ot 85b E.W. Otten, Hyp. Int. 21: 43 (1985)

Ot 85c E.W. Otten, J. Phys. Soc. Japan 54, suppl I: 59 (1985)

Po 83 M.G. Porquet, C. Bourgeois, P. Kilcher and J. Sauvage-Letessier, Nucl. Phys. A411: 65 (1983)

Pr 73 D. Proetel, R.M. Diamond, P. Kienle, J.R. Leigh, K.H. Maier and F.S. Stephens, Phys. Rev. Lett. 31: 896 (1973)

Ra 78 R.S. Raghavan, D.E. Murnick, eds., Proc. 4th Int. Conf. on Hyp. Int., Madison, New Jersey, 1977, Hyp. Int. 4 (1978)

Ra 78b I. Ragnarsson, S.G. Nilsson and R.K. Sheline, Phys. Rep. 45: 1 (1978)

Ra 79 H.L. Ravn, Phys. Rep. 54: 201 (1979)

Ra 80 I. Ragnarsson, in Future Directions in Studies of Nuclei far from Stability, (J.H. Hamilton, E.H. Spejewski, C.R. Bingham and E.F. Zganjar, ed.) North Holland Publ. Comp., Amsterdam, 1980, p. 367

Ra 83 I. Ragnarsson, Phys. Lett. 130B, 353 (1983)

Ra 85 G.N. Rao, ed., Proc. Int. Workshop on Hyperfine Interactions, Kanpur, India, 1984, Hyp.Int. 24-26: (1985)

Re 62 A.S. Reiner and L. Wilets, Nucl. Phys. 36: 457 (1962)

Re 71 B.S. Reehal and R.A. Sorensen, Nucl. Phys. A161: 385 (1971)

Re 79 H. Rebel, H.J. Gils and G. Schatz, eds., Proc. Int. Disc.-Meeting on "What do we know about the radial shape of nuclei in the Ca region", KFK-Rep. 2830, Karlsruhe (1979)

Re 79b P.G. Reinhard and D. Drechsel, Z. Phys. A290: 85 (1979)

Re 80 H. Rebel, K. Bekk, G. Nowicki, G. Schatz, Nukleonika 25: 145 (1980)

Re 84 P.G. Reinhard and E.W. Otten, Nucl. Phys. A420: 173 (1984)

Ro 72 A. Rosen and I. Lindgren, Phys. Scr. 6: 109 (1972)

Ro 84 L. Robertsson and C. Ekström, Göteborg Institute of Physics Report GIPR-256 and to be published

Ro 84b A. Rosen, B. Fricke and G. Torbohm, Z. Phys. A316: 157 (1984)

Ru 73 N. Rud, D. Ward, H.R. Andrews, R.L. Graham and J.S. Geiger, Phys. Rev. Lett. 31: 1421 (1973)

Sa 65 P.G.H. Sandars and J. Beck, Proc. Roy. Soc. A289: 97 (1965)

Sc 35 H. Schüler and T. Schmidt, Z. Phys. 94: 457 (1935)

Sc 55 C. Schwartz, Phys. Rev. 97: 380 (1955)

Sc 57 C. Schwartz, Phys. Rev. 105: 173 (1957)

Sc 75 H. Schweickert, J. Dietrich, R. Neugart and E.W. Otten, Nucl. Phys. A246: 187 (1975)

Sc 78 F. Scheck, Phys. Rep. 44: 187 (1978)

Sc 78b B. Schinzler, W. Klempt, S.L. Kaufman,H. Lochmann, G. Moruzzi, R. Neugart, E.W. Otten, J. Bonn, L. von Reisky, K.P.C. Spath, J. Steinacher and D. Weskott, Phys. Lett. 79B, 209 (1978)

Se 69 E.C. Seltzer, Phys. Rev. 188: 1916 (1969)

Sh 76 K. Shimoda, ed., High Resolution Laser Spectroscopy, Topics in Applied Phys. 13: 51, Springer Verlag, Heidelberg (1976)

Sh 82 E.B. Shera, H.D. Wohlfahrt, M.V. Hoehn and Y. Tanaka, Phys. Lett. 112B: 124 (1982)

Si 80 R.F. Silverans, G. Borghs, G. Dumont and J.M. van den Cruyce, Z. Phys. A295: 311 (1980)

Si 85 R.F. Silverans, G. Borghs, P. de Bishop and M. van Hove, Hyp. Int. 24: 181 (1985)

Si 86 R.F. Silverans, private communication and R.F. Silverans, P. Lievens, F. Buchinger, E.B. Ramsay, E. Arnold, W. Neu, R. Neugart, G. Ulm and K. Wendt, to be published

Sp 85 K.P.C. Spath, doctoral thesis, Mainz (1985)

St 50 R.M. Sternheimer, Phys. Rev. 80: 102 (1950)

St 79 H.H. Stroke, D. Proetel and H.J. Kluge, Phys. Lett. 82B: 204 (1979)

St 85 R.M. Steffen, Hyp. Int. 24: 223 (1985)

St 85b N. Stone, Hyp. Int. 22: 3 (1985)

St 85c J. Streib, H.J. KLuge, H. Kremmling, R.B. Moore, H.W. Schaaf, K. Wallmeroth, Z. Phys. A321, 537 (1985)

Ta 56 I. Talmi and R. Thieberger, Phys. Rev. 103: 718 (1956)

Ta 71 I. Talmi, Nucl. Phys. A172: 1 (1971)

Ta 83 Y. Tanaka, R.M. Steffen, E.B. Shera, W. Reuter, M.V. Hoehn, J.D. Zumbro, Phys. Rev. Lett. 51: 1633 (1983)

Ta 84 I.Talmi, Nucl. Phys. A423: 189 (1984)

Th 81 C. Thibault, F. Touchard, S. Büttgenbach, R. Klapisch, M. de Saint Simon, H.T. Duong, P. Jaquinot, P. Juncar, S. Liberman, P. Pillet, J. Pinard, J.L. Vialle, A. Pesnelle, G. Huber, Phys. Rev. C23: 2720 (1981)

Th 81b C. Thibault, F. Touchard, S. Büttgenbach, R. Klapisch, M. de Saint Simon, H.T. Duong, P. Jaquinot, P. Juncar, S. Liberman, P. Pillet, J. Pinard, J.L. Vialle, A. Pesnelle, G. Huber, Nucl. Phys. A367: 1 (1981)

Th 83 R.C. Thompson, M. Anselment, K. Bekk, S. Göring, A. Hanser, G. Meisel, H. Rebel, G. Schatz, B.A. Brown, J. Phys. G9: 443 (1983)

To 64 W.J. Tomlinson, H.H. Stroke, Nucl. Phys. 60: 614 (1964)

To 82 F. Touchard, J.M. Serre, S. Büttgenbach, P. Guimbal, R. Klapisch, M. de Saint Simon, C. Thibault, H.T. Duong, P. Juncar, S. Liberman, J. Pinard, J.L. Vialle, Phys. Rev. C25: 2756 (1982)

To 82b F. Touchard, P. Guimbal, S. Büttgenbach, R. Klapisch, M. de Saint Simon, J. M. Serre, C. Thibault, H.T. Duong, P. Juncar, S. Liberman, J.

Pinard, J.L Vialle, Phys. Lett. 108B: 169 (1982)

To 85 G. Torbohm, B. Fricke and A. Rosen, Phys. Rev. A31: 2038 (1985)

Tr 81 F. Träger, Z. Phys. A299: 33 (1981)

Ul 75 S. Ullrich and E.W. Otten, Nucl. Phys. A248: 173 (1975)

Ul 85 G. Ulm, J. Eberz, G. Huber, H. Lochmann, R. Menges, R. Kirchner, O. Klepper, T. Kühl, P.O. Larsson, D. Marx, D. Murnick and D. Schardt, Z. Phys. A321: 395 (1985)

Ul 86 G. Ulm, S.K. Bhattacherjee, P. Dabkiewicz, G. Huber, H.J. Kluge, T. Kühl, H. Lochmann, E.W. Otten, K. Wendt, S.A. Ahmad, W. Klempt, R. Neugart Z. Phys. A325: 247 (1986)

Va 85 D. Vandeplassche, E. van Walle, J. Wouters, N. Severijns and L. Vanneste, Hyp.Int. 22: 483 (1985)

Vo 77 E.I. Volmyanskii and V.G. Dubro, Bull. Acad. Sci. USSR, Phys. Ser. (USA) Vol.41, no. 6, p. 124, transl. of Izv. Acad. Nauk., SSSR, Ser. Fiz. vol. 41, no. 6, p. 1252 (1977)

Wa 85 E. van Walle, J. Wouters, D. Vandeplassche, N. Severijns and L. Vanneste, Hyp. Int. 22: 83 (1985)

Wa 87 K. Wallmeroth, G. Bollen, M.J.G. Borge, J. Campos, A. Dohn, P. Egelhof, J. Grüner, H.J. Kluge, U. Krönert, F. Lindenlauf, R.B. Moore, A. Rodriguez, A. Venugopalan, J. Wood, Hyp. Int. in print

Wa 87b K. Wallmeroth, G. Bollen, A. Dohn, P. Egelhof, J. Grüner, J. Campos, A. Rodriguez, M.J.G. Borge, A.

Venugopalan, J.L. Wood, R.B. Moore and H.J. Kluge, subm. to Phys. Rev. Lett.

We 81 R. Wenz, A. Timmermann and E. Matthias, Z. Phys. A303: 87 (1981)

We 84 K. Wendt, S.A. Ahmad, F. Buchinger, A.C. Mueller R. Neugart, E.W. Otten, Z. Phys. A318: 125 (1984)

We 85 K. Wendt, doctoral thesis, Mainz (1985)

We 87 K. Wendt, S.A. Ahmad, W. Klempt, R. Neugart, E.W. Otten, H.H. Stroke, Z. Phys. D4: 227 (1987)

We 87b K. Wendt, S.A. Ahmad, W. Klempt, R. Neugart, E.W. Otten, to be published

Wh 64 L. Wharton, L.P. Gold and W. Klemperer, Phys. Rev. 133, B270 (1964)

Wi 76 W.H. Wing, G.A. Ruff, W.E. Lamb, jr. and J.J. Spezewski, Phys. Rev. Lett. 36: 1488 (1976)

Wo 72 C.Y. Wong, Phys. Lett. 41B: 446 (1972)

Wo 77 H. Wollnik, F.K. Wohn, K.D. Wünsch and G. Jung, Nucl. Phys. A291: 355 (1977)

Za 71 L. Zamick, Ann. of Phys. 66: 784 (1971)

Za 85 D. Zawischa, Phys. Lett. 155B: 309 (1985)